THESIS FOR THE DEGREE OF DOCTOR OF PHILOSOPHY

Deactivation of Catalysts and Reaction Kinetics for Upgrading of Renewable Oils

Prakhar Arora

CHALMERS

Chemical Engineering Division
Department of Chemistry and Chemical Engineering

CHALMERS UNIVERSITY OF TECHNOLOGY

Gothenburg, Sweden
2019

Deactivation of Catalysts and Reaction Kinetics for Upgrading of Renewable Oils

Prakhar Arora
ISBN: 978-91-7905-214-0

Doktorsavhandlingar vid Chalmers Tekniska Högskola.
Ny serie nr 4681
ISSN 0346-718X

Department of Chemistry and Chemical Engineering
Chalmers University of Technology
SE-412 96 Gothenburg
Sweden
Telephone + 46 (0)31-772 1000

Cover:
Graphical illustration of conversion of different waste oils containing impurities to green diesel (HVO) during catalytic hydrodeoxygenation process.

Printed by Chalmers Reproservice
Gothenburg, Sweden 2019

Deactivation of Catalysts and Reaction Kinetics for Upgrading of Renewable Oils

Prakhar Arora
Department of Chemistry and Chemical Engineering
Chalmers University of Technology, Gothenburg 2019

Abstract

The transport sector is one of the main contributors of greenhouse gas emissions in the world. Advanced biofuels from renewable oils can play a decisive role in reducing carbon emissions from the transport sector. Advanced biofuels from waste streams like tall oil, used cooking oil etc. can lower the CO_2 emissions in a range of up to 90% making our future and society more sustainable. Catalytic hydrodeoxygenation (HDO) is a process in which oxygen is selectively removed from renewable oils to produce advanced biofuels. These biofuels are drop-in hydrocarbons which can substitute fossil-based fuels without infrastructure or vehicle changes. This thesis focuses on aspects of catalyst deactivation and reaction kinetics during the production of such biofuels via HDO reactions.

Renewable oils can be sourced from varied streams like tall oil (paper industry residue), animal fats, used cooking oil etc. due to which their composition and innate contaminants can vary significantly. Phosphorus, alkali metals like potassium or sodium, iron, silicon, chlorides etc. are some of the common poisons present in renewable feedstocks which can cause catalyst deactivation during the upgrading process. In the first section of this thesis, the influence of iron (Fe), phosphorus (from phospholipid) and potassium (K) as poisons during HDO of fatty acids over molybdenum based sulfided catalysts was investigated. A range of concentration of poisons was evaluated to show that these poisons severely impacted the activity of catalysts. A change in selectivity was also seen, which is an important parameter to consider during the industrial production of biofuels. Different characterization techniques were employed to study the poison distribution on catalyst samples from lab experiments as well as from a refinery. It was suggested that Fe deposits preferentially near Ni-rich sites which deteriorated the ability of these catalysts to create active sites i.e. via sulfur vacancies. However, phosphorus resulted in irreversible phase transformation of the support to aluminum phosphate ($AlPO_4$) which resulted in catalyst deactivation via pore blockage. In the comparative experiments, with spherical catalyst particles (1.8 mm), the Fe caused the strongest deactivation among P and K, based on the quantity added to feed oil. Although, considering the decrease in surface area per unit of deposited element after the experiment, then P caused the most deactivation. It was concluded that Fe deposited mostly near to the outer surface irrespective of concentration while P and K penetrated deeper in catalyst particles such that the distribution profile was dependent on the concentration.

Reaction kinetics of HDO of fatty acids provides critical knowledge which could be applied at the refining scale in process design and optimization. The activity and selectivity of NiMo catalyst during HDO of stearic acid was studied by varying reaction conditions like temperature, pressure, feed concentration and batch-reactor stirring rate and using intermediates like octadecanal and octadecanol. A deeper understanding of the reaction scheme and selectivities was developed based on the experimental results. A Langmuir–Hinshelwood-type mechanism was used to develop a kinetic model which well-predicted the changes in selectivities at varying reaction conditions.

Keywords: Advanced biofuels, HVO, Hydrodeoxygenation, NiMo, Catalyst deactivation, Kinetic modeling

लहरों से डरकर नौका पार नहीं होती

कोशिश करने वालों की हार नहीं होती

The ones who toil are never vanquished..

The ships that dread the waves.. never reach the end of the sea.

Sohan Lal Dwivedi

Acknowledgements

Looking back, it has been a great learning experience with a sense of growing as a person and achieving milestones along the journey. I am geared up for new challenges but before that I would like to thank people who have helped me to develop at both personal and professional level.

Firstly, I would like to deeply thank my supervisor Prof Derek Creaser during this voyage. He has been a guiding star during the challenging times. Thanks for being patient and supportive during the discussions, thesis writing and more.

Many thanks to my examiner, Prof. Louise Olsson who has been so kind and helpful at many occasions. Your supervision, expert knowledge and support throughout these years is greatly acknowledged.

Prof. Magnus Skoglundh, the director of KCK and all senior members are gratefully acknowledged for being conducive and engaging.

I also want to thank Preem AB as the industrial partner in this project. Special thanks to Eva Lind Grennfelt, Henrik Rådberg and Stefan Nyström for all the insightful discussions and giving a shape to this project.

Salam and Wayne, thanks a lot for your frequent help in the lab (even outside the working hours). You have given me valuable scientific inputs during experiments, analysis and writing. Thank you Wayne for proofreading the thesis. Thanks to all friends and colleagues for the memories to cherish – Poonam, Joonsoo, Houman, Ida, Xavier, Jungwon, Tobias, Pouya, Aiyong, Rasmus, Patric, Sreetama, Masood, Joby, Rojin, Jesus and Diana. A special mention to previous colleagues – Stefanie, Nadya, Oana, Kurnia, Kunpeng and Lidija. I would also like to acknowledge all my colleagues at KCK and KART.

Malin, Ximena, Bengisu and Anna, thanks for your support.

Marco, Katarina and Hoda for your excellent contributions during your master thesis projects. I benefited a lot as a co-supervisor of your master's project and I am glad to see you doing well in your careers.

Badminton buddies and coach at times at Olofshöjd and Fjäderborgen.

Some people transform you at different stages of life - Dr. S.R. Sharma, Dr. Neelesh Dahanukar, Dr. V.G. Anand, Dr. Dharmesh Kumar, Dr. Martin Linck, Anders Hultgren and Peter Olofsson. I am continually inspired by their passion and commitment. Thanks for being there as my mentors and encouraging me to push my limits.

My old friends and confidants to whom I look for advice and bouncing my random ideas – Subhajit, Ashutosh, Saurabh, Nishtha and Parivesh.

Michelle, you are amazing and I am deeply grateful for your support in difficult times, excitement in adventures and all the wonderful shared memories. I look forward to you acing the medicine programme and becoming a doctor!

π for being the cat(alyst) of my life.

My parents, Pratibha and Sunil, who have always supported me and blessed me with unconditional love. My brother and his wife, Dr. Shashank and Dr. Rashi, who have always

encouraged me to pursue my dreams. My adorable niece, Aadita whose innocence gives me new perspective on life now and then.

This work is performed at the Competence Centre for Catalysis in collaboration with Preem. We would like to acknowledge Formas (Contract: 239-2014-164) and Preem for the financial support. The Competence Centre for Catalysis is financially supported by Chalmers University of Technology, the Swedish Energy Agency and the member companies: AB Volvo, ECAPS AB, Johnson Matthey AB, Preem AB, Scania CV AB, Umicore Denmark ApS and Volvo Car Corporation AB.

List of publications and contribution

I. Investigating the effect of Fe as a poison for catalytic HDO over sulfided NiMo alumina catalysts
Prakhar Arora, Houman Ojagh, Jungwon Woo, Eva Lind Grennfelt, Louise Olsson, Derek Creaser

Applied Catalysis B: Environmental, Volume 227, 2018, Pages 240-251 (https://doi.org/10.1016/j.apcatb.2018.01.027)

Contribution: I planned and defined the scope with co-authors. I performed the experiments in this study. I interpreted the results with co-authors and wrote the first draft of manuscript.

II. Influence of Bio-Oil Phospholipid on the Hydrodeoxygenation Activity of NiMoS/Al2O3 Catalyst
Muhammad Abdus Salam, Derek Creaser, Prakhar Arora, Stefanie Tamm, Eva Lind Grennfelt, Louise Olsson

Catalysts 2018, 8(10), 418
(https://doi.org/10.3390/catal8100418)

Contribution: I planned and defined the scope with co-authors. I performed some experiments in this study with Muhammad Abdus Salam. I interpreted the results with co-authors and reviewed the manuscript.

III. The role of catalyst poisons during hydrodeoxygenation of renewable oils
Prakhar Arora, Hoda Abdolahi, You Wayne Cheah, Muhammad Abdus Salam, Eva Lind Grennfelt, Henrik Rådberg, Derek Creaser, Louise Olsson

Submitted for publication

Contribution: I planned and defined the scope with co-authors. I performed the experiments with some assistance from Hoda Abdolahi in this study. I interpreted the results with co-authors and wrote the first draft of manuscript.

IV. Kinetic study of hydrodeoxygenation of stearic acid as model compound for renewable oils
Prakhar Arora, Eva Lind Grennfelt, Louise Olsson, Derek Creaser

Chemical Engineering Journal, Volume 364, 15 May 2019, Pages 376-389
(https://doi.org/10.1016/j.cej.2019.01.134)

Contribution: I planned and defined the scope with co-authors. I performed the experiments in this study. I was assisted by Derek Creaser with simulations. I interpreted the results with co-authors and wrote the first draft of manuscript.

Publications not included in this thesis

1. Effect of Dimethyl Disulfide on Activity of NiMo Based Catalysts Used in Hydrodeoxygenation of Oleic Acid
   Houman Ojagh, Derek Creaser, Stefanie Tamm, Prakhar Arora, Stefan Nyström, Eva Lind Grennfelt, and Louise Olsson

   Industrial & Engineering Chemistry Research 2017 56 (19), 5547-5557 (http://dx.doi.org/10.1021/acs.iecr.6b04703)

2. Investigation of the robust hydrothermal stability of Cu/LTA for NH3-SCR reaction
   Aiyong Wang, Prakhar Arora, Diana Bernin, Ashok Kumar, Krishna Kamasamudram, Louise Olsson

   Applied Catalysis B: Environmental, Volume 246, 2019, Pages 242-253 (https://doi.org/10.1016/j.apcatb.2019.01.039)

3. NiMoS on alumina-USY zeolite for hydrotreating lignin dimers: Effect of support acidity and cleavage of CC bond
   Muhammad Abdus Salam, Prakhar Arora, Houman Ojagh, You Wayne Cheah, Louise Olsson, Derek Creaser

   Sustainable Energy Fuels, October 2019 (https://doi.org/10.1039/C9SE00507B)

List of abbreviations

BET	Brunauer Emmett Teller
BJH	Barret Joyner Halenda
BSTFA	N,O-Bis(trimethylsilyl)trifluoroacetamide
C17+	Saturated and unsaturated isomers of C17 hydrocarbons
C18+	Saturated and unsaturated isomers of C18 hydrocarbons
C18=O	Octadecanal
C18-OH	Octadecanol
CUS	Coordinately unsaturated sites
DCO	Decarbonylation
DCO_2	Decarboxylation
DCOx	Decarbonation
DMDS	Dimethyl disulfide
DSC	Differential scanning calorimeter
EDX	Energy dispersive x-ray
EOS	Equation of state
FAs	Fatty acids
FFA	Free fatty acid
FID	Flame ionization detector
GC	Gas chromatography
GDP	Gross domestic product
GHG	Greenhouse gas
HAADF	High angle annular dark field
HDO	Hydrodeoxygenation
HDM	Hydrodemetallization
HDN	Hydrodenitrogenation
HDS	Hydrodesulphurisation
HEFA	Hydroprocessed Esters and Fatty Acids
HR-TEM	High resolution transmission electron microscopy
HVO	Hydrotreated Vegetable Oil

ICP-SFMS	Inductively coupled plasma sector field mass spectrometry
LGO	Light gas oil
MS	Mass spectrometer
MTOE	Million tonnes of oil equivalent
OA	Oleic acid
OPEC	Organization of the petroleum exporting countries
PAHs	Polynuclear aromatic hydrocarbons
PSRK	Predictive Soave-Redlich-Kwong
RPM	Revolutions per minute
SA	Stearic acid
SEM	Scanning electron microscopy
SSR	Squares of the residuals
STEM	Scanning transmission electron microscopy
TAN	Total acid number
TCD	Thermal conductivity detector
TEM	Transmission electron microscopy
TGs	Triglycerides
TMS	Transition metal sulfides
TOFA	Tall oil fatty acid
TPR	Temperature programmed reduction
VGO	Vacuum gas oil
VLE	Vapor liquid equilibrium
XPS	X-ray photoelectron spectroscopy

Contents

1 Introduction

1.1 World's Outlook and Climate Crisis

The world is facing a dual energy challenge; to meet the rising energy demand while reducing carbon emissions at the same time. The demand for energy will increase as the world's population grows and people aspire to a higher quality of life. It is forecasted that due to the combination of growth in population and GDP per capita, the global GDP will more than double from 114 Trillion USD in 2017 to 236 Trillion USD by 2040 [1]. To reduce energy related emissions poses risks as well as opportunities. Technological innovation driven by our commitment and hard-work will enable the worlds transition towards a low-carbon or even carbon-neutral energy system. The UN's Sustainable Development Goals (SDGs) provide a roadmap and targets to prevent the climate change looming over us. The Intergovernmental Panel on Climate Change (IPCC) report explains the far-ranging impacts and threats of 1.5 °C global warming above the pre-industrial era. This report tells that human activities like burning of fossil fuels are estimated to have resulted in approximately a 1 °C of global warming above pre-industrial levels. Further on, if it continues to increase at the current rate, the global warming is likely to reach 1.5 °C between 2030 and 2052. Fig 1.1 shows the current trajectory and projection of global temperature change relative to 1850-1900.

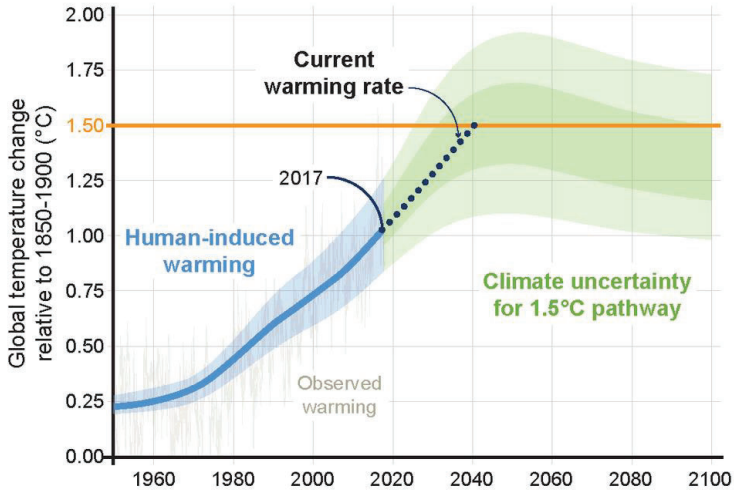

Fig 1.1 How close are we to 1.5 °C? [2]

Global warming will cause irreversible long-term changes in the climate system, such as the submerging of islands and coastal flooding with a rise in sea level, decrease in agricultural output, heat waves etc. Some of these impacts on natural and human systems like European countries walloped by heat waves, loss of warm-water coral reefs at an alarming rate etc. can already be seen today. As per the latest UN report on biodiversity, around one million animal and plant species are at imminent risk of extinction due to the devastating impact of climate change [2].

The major cause of global warming is due to the release of greenhouse gases (GHGs) by human activities. The greenhouse gases in the atmosphere traps heat radiating from Earth, resulting in a heating up of our planet. There are different GHGs - like carbon dioxide (CO_2), methane (CH_4), nitrous oxide (N_2O) etc. However, carbon dioxide is the most important force causing the climate crisis. Human activities are changing the balance of these gases in the atmosphere. For example different anthropogenic activities like the burning of coal and oil, cement production and land-use change cause carbon dioxide emissions. In 2018, fossil-fuel-related global CO_2 emissions are expected to approach a striking total of 37.1 billion metric tons [3]. In the US, the energy related carbon dioxide emissions account for about 98% of US CO_2 emissions [4].

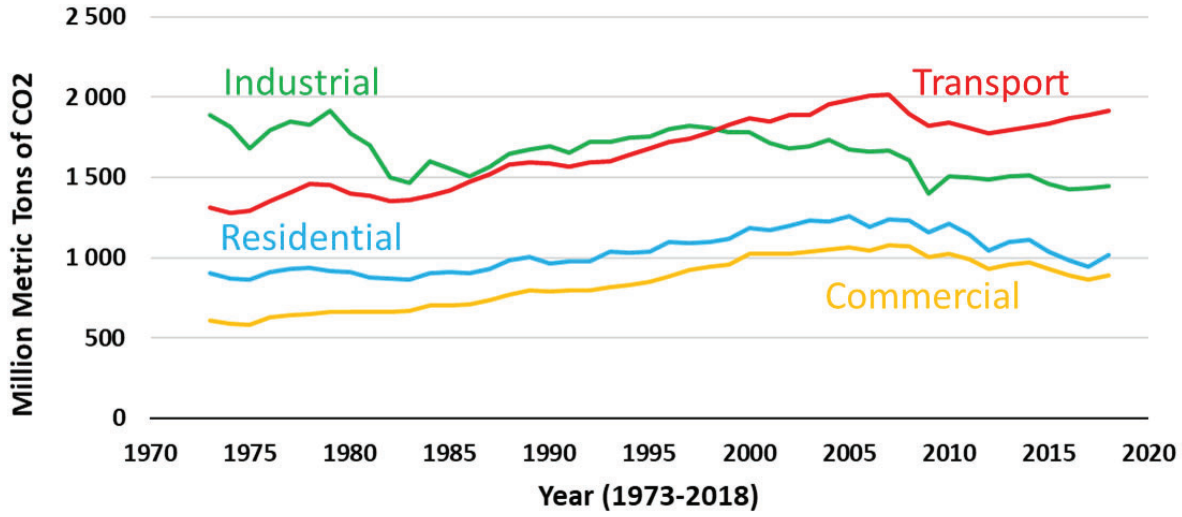

Fig 1.2 Carbon dioxide emissions by end-use sector in US, 1973-2018 [5].

Carbon emissions can be attributed to four primary economic sectors - Transport, Industry, Residential and Commercial. Here, the transportation sector consists of all vehicles whose purpose is to move people and/or goods from one point to another. Vehicles employed for other purposes than transportation like construction cranes, farming vehicles and vehicles in mining are classified in their respective sector and not in the transport segment. The industrial sector is composed of different sectors like manufacturing, agriculture, forestry, mining including oil and gas extraction, construction etc. All facilities and equipment used in production, processing or assembling in these sectors correspond to the industrial segment. The residential sector includes energy consumed in living quarters for private households. The commercial sector includes service providing facilities and equipment of businesses; federal, state, and local governments; and other private and public organizations. Fig 1.2 shows the carbon dioxide emissions in million metric tons by end-use sector from 1973-2018 in the US. The share of carbon emissions for these economic sectors were – Transport - 36%; Industrial - 27%; Residential - 19% and Commercial - 17%.

It is interesting to examine in the present and immediate future how some of the green technologies are being adapted and obsolete processes replaced to lower carbon emissions in different economic sectors. In the industrial sector, heat accounts for around two-thirds of the total energy demand which is mainly produced by fossil-fuel combustion. There are a few incremental steps being implemented while some of the transformative solutions are still in the pilot stage to decarbonize this sector. Fuel switching (coal to gas), electrification of low-medium heat processes (below 400 °C) etc. are some of the measures being implemented. Electrification of high temperature industrial processes like steel production may not be viable. In Sweden, steel producers are pursuing a fundamental change to shift away from coking coal to hydrogen, which will be generated from surplus renewable electricity via electrolysis [6].

The costs of electricity from solar and wind is dropping at a fast rate around the world. It is expected that by 2025, in a majority of countries the cost of power generation from renewables will be cheaper than electricity from coal or gas combustion thermal plants [7]. The electricity grids across the continents will become greener with the looming shutdowns of coal plants and each new installation of solar photovoltaic (PV) and wind turbines. This will propel the decarbonization of both commercial and residential sectors due to their large consumption of electricity. Also, the increased energy efficiency and reduction in heat-loss due to improved materials will further lower the carbon footprints of these two sectors. However, the reduction of carbon emissions from the transport sector is relatively a tough nut to crack in the dawning challenge of climate change. It can be seen in Fig 1.2 that the average trend for carbon dioxide emissions from all sectors are on the decline, except from the transport sector.

1.2 Challenges in the Transport sector

We are at the brink of an upheaval of the transportation system with the advancement in technologies like shared mobility, autonomous driving and electric vehicles. However, the existing fleet of over a billion vehicles in the world still depends on fossil-based liquid hydrocarbons like petrol, kerosene, diesel etc. Worldwide, petroleum and other liquid fuels are the dominant sources of transportation energy, although their share of total transportation energy is expected to marginally decline from 94% as of today to 85% in 2040 as per the current trajectory [1]. This indicates the mammoth scale of the problem and the urgency to find alternate green solutions and enforce seismic transformation of the transport sector. In Fig 1.3, the energy consumption by different modes of transport for passenger and freight traffic is shown. Continuing urbanization and a significant expansion of the middle class in many parts of the world will increase the cars on the roads and total miles travelled per year. Light duty vehicles account for 70% of fossil fuel demand in the passenger category, and the demand will grow by 33% by 2050 [8]. As the population and GDP per capita grows, we will see a large increase in freight transport demand. Heavy duty trucks have a share of 60% of the petroleum demand in the freight segment and the demand will grow by 22% by 2050 [8]. Also, it can be seen from Fig 1.3 that the demand for liquid fuels will continue to grow. This suggests that the status quo with continued strong dependence on combustion of fossil fuels for transportation needs, could result in an unchecked growth of emissions of carbon dioxide. This is concurrent to the current situation discussed in the previous section where the transportation sector was the largest source of carbon emissions in the US (see Fig 1.2).

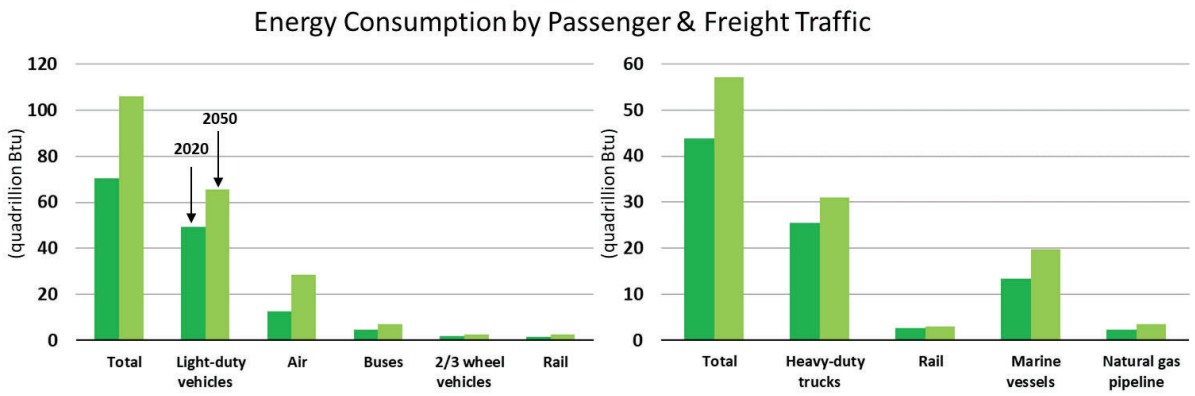

Fig 1.3 Global energy consumption of transport sector by mode comparing 2020 to 2050 [9].

It is envisioned that there will be no silver bullet to mitigate the carbon emissions from the transport sector. Instead, myriad solutions will be needed, such as improved engine efficiency, electrification, shared mobility and switching to advanced biofuels etc. Also, the intangible actions like policy shift, increased awareness, consumer driven demand for renewables etc. will help to curb emissions from the transport sector. These changes sound extensive but are not impossible, and they are most likely inevitable. We should not underestimate the effort required and the scale of changes that will be necessary to a achieve fossil free future.

1.3 Roadmap for Decarbonization of Transport sector

Improved engine efficiency and shared mobility offer incremental steps on our journey to reduce the carbon footprint from the transport sector. Even the small gains achieved by these steps are significant to combat climate change, but not decisive in the long run. Thus, there is a greater need to adapt and implement Kaikaku (radical changes) in transport sector – Electrification and switching to advanced biofuels are the radical solutions to fall in this category. The electrification of light vehicles seems imminent with the improvement in technology and economies of scale driving the costs of batteries down. This will drastically reduce the passenger vehicle related CO_2 emissions. However, the long-range commercial road transportation will continue to require liquid hydrocarbons for several more years. Also, the electrification of marine vessels like cargo ships etc. and passenger aircraft seems far-fetched. This is where advanced biofuels should come in the picture. Advanced biofuels which can lower the carbon emissions in a range of 70 -90% provide an excellent bridge during this transition period for the existing fleet of traditional combustion engine-based vehicles and for aviation and shipping, where electrification would be unfeasible.

Biofuels can be classified in three categories based on feedstock employed in their production or their impact on resources–

a. Bad biofuels - When the feedstock competes with food for the use of arable land, requires large amounts of fresh water or causes loss of biodiversity. The tropical rainforests are a carbon sink and it is unjustifiable to clear huge swaths of biodiversity-rich tropical rainforest for palm plantations in order to use palm oil to produce fuels. Similarly, producing fuels from edible crops like maize or canola oil is controversial. It is not reasonable to prioritize energy demand over food requirements of humans.

b. Good biofuels (Current generation) - When the feedstock is from a waste stream and in liquid state so that it can be processed/co-processed employing existing infrastructure of pipelines and refineries etc. Feedstocks like animal fats from food industry waste, fish fat from fish processing waste, residues from vegetable oil processing, used cooking oil from homes and restaurants, technical corn oil (a residue from ethanol production) and forest industry residues like tall oil. These feedstocks can be processed stand alone or co-fed with fossil feedstocks to produce renewable fuels. Hydrogenated vegetable oils (HVO) and hydroprocessed esters and fatty acids (HEFA) are commercially available example of biofuels which are produced from the above mentioned feedstocks. These raw materials do not compete with food and are from the waste streams of existing industrial processes. These renewable feedstocks from wastes and residues offer a reduction of 85-90% in greenhouse gas emissions compared to traditional diesel.

c. Good biofuels (Next generation) - When the feedstocks are sustainable or are a residue and in solid state to begin with. Feedstocks like agricultural waste, municipal solid waste (MSW), forestry residue, lignin, plastic wastes etc. There are several different technologies to upgrade such solid biomass based feedstocks to produce crude renewable oils which can be further upgraded to drop-in liquid fuels which can be used as engine fuels. Rapid thermal degradation i.e. pyrolysis to produce volatile compounds which can be cooled back to room temperature to generate a brownish liquid crude fuel called “bio-oil”. There are some advanced technologies which integrate hydropyrolysis and hydrotreating to convert solid biomass into liquid transportation fuels like IH2® [10].

It is important to consider the impact of biofuels over their life cycle so that the unintended negative impacts on land, water and biodiversity can be avoided. The overall positive impact of “Good biofuels” on the environment depends a lot on the feedstock from which it is produced. Thus it becomes critical that companies producing biofuels are transparent and provide traceability of raw feedstock supply chains to ensure that the biofuels are good for the environment. This would benefit supportive government policies and public confidence in the contribution of biofuels to realize decarbonization of the transport sector.

One of the “Good Biofuels” from the current generation are - HEFA (Hydroprocessed Esters and Fatty Acids), also known as HVO (Hydrotreated Vegetable Oil), is a renewable diesel fuel that can be produced from a gamut of feedstocks like animal fats and grease, waste vegetable oils, and forestry residues like tall oil. These biofuels are categorized “good” if produced from waste materials or renewable streams but if produced from food crops like raps oil or palm oil then they are not so “good” anymore. These various renewable feedstocks could be hydroprocessed stand alone or co-fed with petroleum feedstock as well [11].

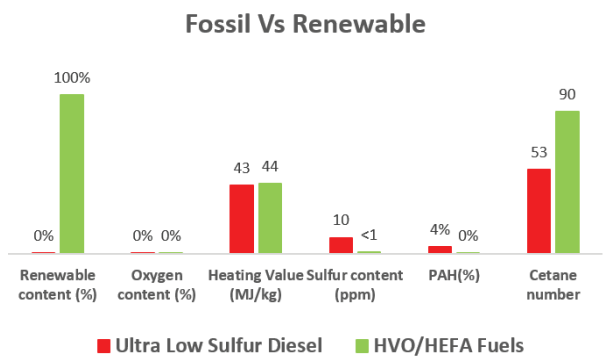

	Ultra Low Sulfur Diesel	HVO/HEFA Fuels
Renewable content (%)	0	100
Oxygen content (%)	0	0
Heating Value (MJ/kg)	43	44
Sulfur content (ppm)	10	1
Polyaromatics (%)	4	0
Cetane number	53	90
GHG emissions	Baseline	-90%
PM emissions	Baseline	-46%
Nox Emissions	Baseline	-14%
Storage stability	Baseline	Good

Fig 1.4 Comparison of HVO/HEFA and a conventional low-sulfur diesel fuel [12].

When such renewable fuels are used then atmospheric carbon is recycled, while in the case of fossil fuels prehistoric carbon stored in the earth's crust is introduced into the atmosphere when they are burnt. HVO/HEFA fuels are chemically identical to the fossil based hydrocarbons. They could be blended with the "bottoms" of diesel pools as they have much higher cetane numbers. They are advantageous as they employ the existing infrastructure for refining, transportation via pipelines, storage tanks and the existing automotive fleet with no need for engine modification. In fact, HVO/HEFA fuels are premium fuels because of their higher heating value, lower SO_x and NO_x emissions, and reduced levels of polyaromatic hydrocarbons (PAH) and fine particulates [12]. Fig 1.4 illustrates some of the advantages of HVO/HEFA fuels over tradition diesel fuel. Additionally, these HVO/HEFA fuels have lower greenhouse gas (GHG, gCO_2 eq/MJ) emissions by up to 90% over the lifecycle of the fuel compared to fossil based diesel [13]. Currently, annual capacity for HVO/HEFA fuels is over 2.6 billion liters, and growing at a steady rate [14]. There are several refineries from Neste, ENI, Total, Preem and Repsol producing these renewable HVO/HEFA fuels. NEXBTL™, Ecofining™, Vegan™ & Hydroflex are some of the commercial technologies employed in these refineries [15]. Several more refineries in France, Italy and Singapore are in the pipeline which would further boost the production of these advanced biofuels. It should be highlighted that the core of these refineries is the catalytic hydrodeoxygenation (HDO) process, which is the removal of oxygen from renewable feeds of bio-origin over a catalyst in the presence of hydrogen to produce predominantly water as a side product. Catalytic HDO will be discussed in detail in Section 2.1 of this thesis. The main objective of this thesis is to develop an understanding regarding different challenges related to catalyst deactivation during production of such HVO/HEFA biofuels, as explained in Section 1.6 in detail. With all these benefits, HVO/HEFA fuels have a great potential to substantially decarbonize the world's economy. The demand for transport distillate – jet fuel, road and marine diesel – is growing. This rising demand could be supplemented by HVO/HEFA renewable fuels. Also, the refining processes for these fuels could be tuned to produce hydrocarbons in gasoline, jet kerosene and the diesel range. This could inherently reduce our dependence on fossil fuels in the near future.

1.4 Biofuels and Swedish perspective

Sweden is leading not only in Europe but the whole world on several fronts in renewable energy and with the ambition to reach net-zero atmospheric greenhouse gas emissions. The European Commission has proposed a strategic long-term climate vision for the EU which aims to attain net-zero greenhouse gas emissions by 2050 [16]. Sweden has committed to achieve the goal of net-

zero greenhouse gas emissions in 5 years less, by 2045, and should thereafter achieve negative emissions [17]. Even in the transport sector where the goal to reduce carbon emissions is huge and far-more complex, Sweden is pioneering the implementation of solutions to achieve these exemplary targets. The government has an ambitious goal to reduce the emissions from the transport sector, excluding domestic aviation, by 70% by 2030 [18]. This would enable Sweden to progress toward their final goal to have no net emissions of greenhouse gases into the atmosphere by 2045 [19].

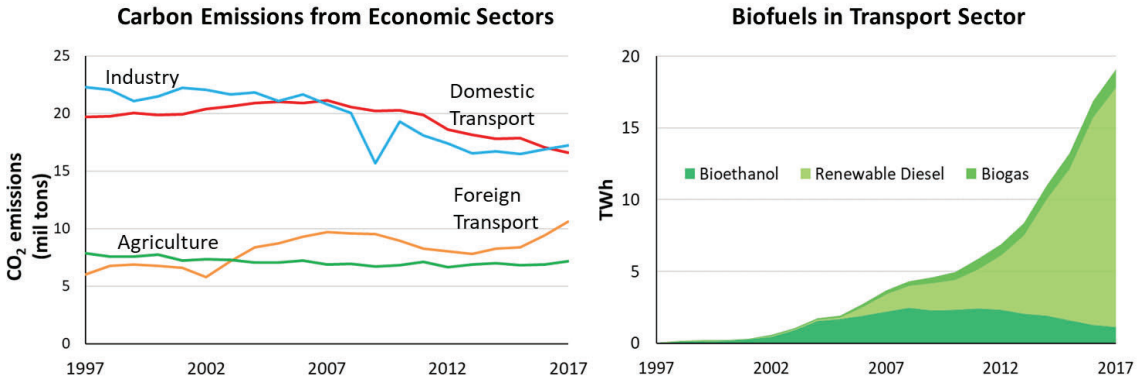

Fig 1.5 Carbon dioxide emissions from main economic activities in Sweden[20] (left) and different biofuels used in the transport sector in Sweden[21] (right), from 1997 -2017).

It may seem like a daunting task but it is achievable as Sweden has existing capabilities for biofuel production and a vast potential for biomass resources. Fig 1.5 presents the carbon emissions from the four largest economic sectors in terms of emissions in Sweden (on left) and the use of different biofuels in the transport sector in Sweden (on right). This figure indicates the current situation and the challenges related to carbon emissions. In 2017, domestic and foreign (aviation and shipping) transport accounted for a total of 44% of carbon dioxide emissions in Sweden. Increasing adoption of biofuels (mainly HVO/HEFA) has helped the country to control the emissions from the transport sector. Sweden has the highest share of energy from renewable sources used for transport in the European Union (EU) at 38.6% in 2017 [22]. However, as of now, the renewable diesel is mostly used in domestic transport so a decline in carbon dioxide emissions can be seen in Fig 1.5 (right). However, with the growing population and GDP of Sweden, the share of emissions from foreign transport is on the rise. The Fig 1.5 (left) also offers a solution to a part of this problem. It presents the increase in consumption of different biofuels by the transport sector in Sweden. In 2017, the share of Bioethanol, Renewable diesel (eg. HVO/HEFA) and Biogas were 6, 87 and 7% respectively. There is a clear acceptance of HVO/HEFA fuels by the market as it is molecularly the same as fossil diesel and cuts the carbon dioxide emissions by up to 90%. Also, the Swedish industry has an important role to play in this by taking up this challenge to set up biofuel production units and leading the development of innovative processes. The transport sector accounted for a total energy consumption of 88.2 TWh including fossil fuels, biofuels and electricity. However, the fossil fuels like petrol, diesel, aviation fuel etc. accounted for the biggest share at 75%, while biofuels and electricity were at 22 and 3% respectively. The roadmap for achieving a fossil fuel independent transport sector should include all green solutions like biofuels for the existing fleet, passenger aircraft, freight shipping and electrification of other modes of transport. Sweden has a vast area covered in forest, at around 57% of the total land area. More importantly, these forests are

sustainably managed. Also, there are many paper and pulp mills in the country. The waste streams from forestry like branches and tops (GROT) etc. and from the paper and pulp industry like tall oil (from black liquor) and lignin etc. can provide ample quantities of feedstocks for biorefineries. These biomass based feedstocks can be utilized in production of advanced biofuels to bring down the carbon emissions from the transport sector substantially. So, there is a high potential as such biomass based feedstocks are available in huge quantities with existing expertise and efficient raw material logistics which give Sweden a large advantage.

1.5 Scope and objective

The main theme of this thesis is to investigate and develop knowledge on catalyst deactivation during production of advanced biofuels (like HVO/HEFA etc.) in refineries. This is achieved using simulating HDO experiments in a batch-reactor setup with a model refining NiMo catalyst and fatty acids as feedstocks, which are the major component of raw bio-based feedstocks used in HVO/HEFA biofuel production at refinery scale. The influence of different contaminants, commonly present in renewable oils, like iron, phospholipids and alkalis (e.g. Na and K) were studied at varying concentrations. Also, a kinetic study was done as a part of this thesis to fully understand the fundamental chemistry and the reaction scheme during HDO of fatty acids.

Catalyst deactivation is a complex phenomenon with ever-continuing research interest due to the huge costs involved in the operation of industrial catalytic processes. Catalyst deactivation occurring during upgrading of renewable oils is an increasing challenge in refineries producing advanced biofuels. Catalyst deactivation is inevitable. However, with better understanding, it can be either slowed or its consequences can be minimized. Catalyst deactivation is mainly caused due to the following routes; a. Poisoning, b. Coking, c. Sintering, d. Solid-state transformations, e. Masking or pore blockage [23]. We will limit the scope of this thesis to deactivation caused by poisoning due to the contaminants present in the feedstock. However, we will digress to understand the aftereffects, like coking or solid-state transformations caused by these poisons. The traditional knowledge is not directly applicable as the contaminants present in renewable feedstocks are different. In this thesis work, the major poisons were identified as iron, phospholipids and alkalis (e.g. Na and K) based on the academic and patent literature, which was later confirmed from the analysis of a spent catalyst recovered from refinery as well.

In **Paper I**, the effect of iron on change in activity and selectivity of MoS_2/Al_2O_3 (unpromoted) and $NiMoS/Al_2O_3$ (promoted) catalysts was studied. The renewable feedstocks have a high oxygen content and are corrosive in nature with a high total acid number (TAN). Corrosion is a common phenomenon when such renewable oils come in contact with iron vessels during transportation or storage to form iron complexes. The objective of this work is to evaluate the iron poisoning over a Ni/Mo containing catalyst during hydrodeoxygenation. Also, the spent catalysts were investigated using different characterization techniques to explain the changed selectivity and peculiar deposition of iron. Phospholipids - another prominent poison present in renewable feeds was investigated in **Paper II.** The catalyst deactivation due to phosphorus (from phospholipid) was studied during HDO of oleic acid. Biomass based feedstocks like used vegetable oil, algal oil etc., contain varying amounts of phosphorus which comes from phospholipids or other cell forming constituents. Phosphatidycholine was used as a model compound from the class of phospholipids.

The interaction of phosphorus affecting the textural properties and chemical composition of the alumina support was further evaluated. In **Paper III**, the first objective was to understand the deactivation of model catalyst samples (spheres of diameter 4 mm) recovered from a refinery and develop methods to revive the activity. The second objective was to simulate the experiments with the identified poisons based on refinery sample. A lab synthesized model $NiMo/Al_2O_3$ catalyst was placed in a refinery unit for biofuel production and thoroughly characterized to evaluate the distribution of different poisons through the catalyst particles. Then a comparative study of the poisons - Fe, K and phospholipid containing P and Na on catalyst deactivation during hydrodeoxygenation of stearic acid was tested in a batch reactor. Different characterization techniques were employed to study the impact of the poisons and how they deposited on the catalyst spheres (1.8 mm). Larger catalyst particles were employed to study how the poisons distribute through the particles which with better represents the refinery situation. The kinetics during HDO of stearic acid over $NiMo/Al_2O_3$ catalyst was explored in **Paper IV**. A set of experiments with varying reaction parameters, such as temperature, pressure, feed concentration and batch-reactor stirring rate were carried out. Also, HDO of the intermediates like octadecanal and octadecanol was tested. The objective was to develop an improved understanding of the reaction scheme and selectivities for the three major reaction routes (decarboxylation, decarbonylation and direct-HDO). A Langmuir–Hinshelwood-type mechanism was used to develop kinetic rate expressions with the aim to predict product selectivity under varying conditions like temperature and hydrogen pressure.

2 Background

2.1 Catalytic hydrodeoxygenation

Hydrotreating is a process employed in refineries around the world to remove the hetero-atoms from fossil based feedstocks like Naphtha, vacuum gas oil (VGO) etc. Catalytic hydrotreating ranks as one of the most important petroleum refining processes along with cracking and reforming. Hydrotreating includes hydrodesulphurization (HDS), hydrodenitrogenation (HDN), hydrodeoxygenation (HDO) and hydrodemetallization (HDM) reactions to remove different impurities. Typically, in fossil feedstocks the oxygen content is not high, so not much attention has been paid to HDO. But renewable feedstocks like lignocellulosic biomass, pyrolysis oil, waste cooking oil, tall oil etc. can contain oxygen in a range of 10-40 wt%. Thus, HDO has been gaining a lot of attention lately as the challenges are different than the traditional HDS and HDN processes. HDO is a hydrotreating process in which oxygen is removed from the feeds in the presence of hydrogen at high temperature and pressure over catalysts [24]. Hydrogen is removed to produce side products like H_2O, CO and CO_2. There are several scientific and engineering problems associated with HDO processes which requires research efforts. To list a few:

a. A lot of water is produced as a side product which can be detrimental to the catalyst support and may contribute to excessive coking.
b. At the introduction of feed in a commercial scale reactor, since HDO is an exothermic process, the sudden rise in temperature could have devastating results which poses technological challenge for the design of the reactors.
c. Contaminants in renewable feeds are very different. It varies from metals like Na, Mg and Fe, to non-metals (Chlorides) and organic compounds (phospholipids) [15, 25, 26]. There is a sincere need to investigate their effect on the catalyst activity under different reaction conditions.

In this thesis, the focus would be on the hydrodeoxygenation of FAs and similar compounds like triglycerides (TGs) and methyl esters. TGs are the esters of glycerol with FAs while methyl esters are formed from the esterification of methanol with FAs. FAs have a carboxyl group (–COOH), with a long carbon chain of 14-24 carbons with 18-carbon FAs are most common [27]. Lauric, capric, palmitic, myristic, oleic, and stearic acids are some common FAs. Fig 2.1 shows a few model compounds from fatty acids, triglycerides and methyl ester classes of compounds. TGs and FAs form the major components of renewable feedstocks like oil from Jatropha, microalgal oil and tall oil [28-30]. Also waste cooking oil contains a high amount of free fatty acids (FFAs) which is

available in large amounts and can be used as a renewable feedstock. Hydrodeoxygenation of such feeds rich in FAs and TGs yields hydrocarbons which are known as renewable or green diesel.

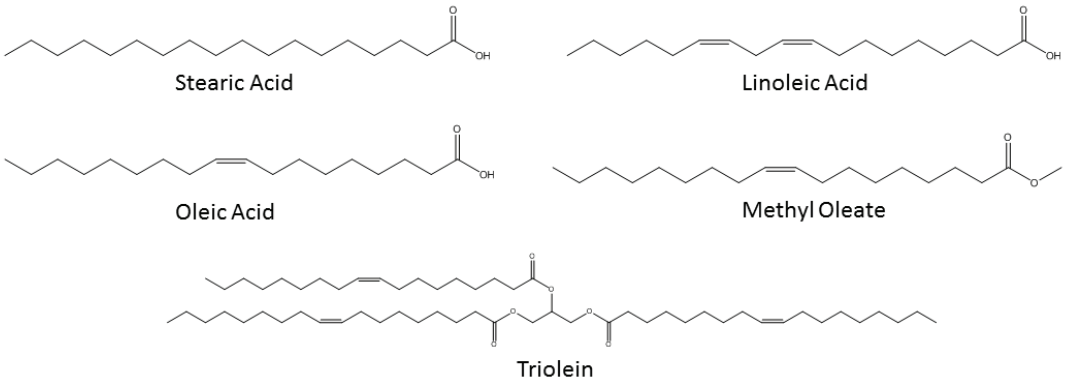

Fig 2.1 A few model compounds (fatty acids, methyl esters and triglycerides).

These various feedstocks can be processed with conventional hydrotreating catalysts like Ni or Co promoted molybdenum sulfide (MoS_2) supported on alumina in a refinery setup to produce hydrocarbons in a temperature range of 300-450 °C and hydrogen pressures of 50-180 bar. These processes have high yields and carbon recovery rates. The reaction chemistry for TGs, methyl esters and FAs is quite similar. Among the latter two, FAs are the most common intermediates. These reactions initiate with the hydrolysis of the ester group present in TGs or alkyl esters and saturation of double bonds in the long alkyl chain, if any. The hydrolysis reaction occurs on the Lewis acidic sites of the alumina support [31] while the active sites on the metal enables the hydrogenation reaction. Then FAs undergo deoxygenation which include hydrodeoxygenation, decarboxylation, decarbonylation. Other reactions include cracking and hydrogenation to produce hydrocarbon final products mostly as straight chain alkanes. Meanwhile the carbon backbone of TGs is converted into propane and other gaseous products including CO, CO_2, H_2O and CH_4 are produced. We will limit our discussions to FAs only in this study.

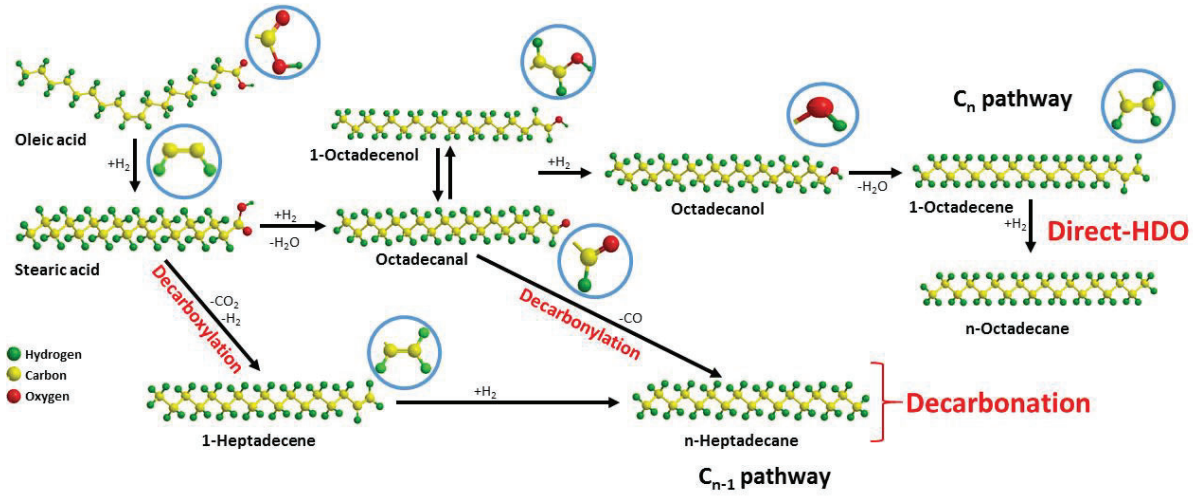

Fig 2.2 Reaction scheme for hydrodeoxygenation of oleic acid (OA).

Fig 2.2 describes the reaction scheme of hydrodeoxygenation of OA. Deoxygenation of FAs over transition metal sulfides (TMS) catalysts happens in following three ways-

a) A so called direct-HDO in which oxygen is removed as a water (H_2O) molecule

b) Decarbonylation (DCO) in which oxygen is removed as carbon monoxide (CO)

c) Decarboxylation (DCO_2) in which oxygen is removed as carbon dioxide (CO_2)

In the first route, a C_n alkane or alkene is formed as the final product with same number of carbon as in the fatty acid. In the latter two routes, a hydrocarbon (alkane or alkene) is formed with one less carbon.

For this thesis, the term decarbonation (DCOx) will be used to refer collectively to decarbonylation and decarboxylation, otherwise they will be separately stipulated. It should be noted that the hydrodeoxygenation or "HDO" is a broader term to define removal of oxygen while "direct-HDO" is specifically used when oxygenated products are converted to produce water as the side product.

2.2 Transition metal sulfides for HDO of FA

In a refinery complex, production of liquid transportation fuels contribute to a major share in the revenues generated. Crude oil could be broadly classified based on its sulfur content; less than 0.7% sulfur content is called Sweet and greater than 0.7% sulfur content is called Sour. Crude oil is distilled into lighter fractions to produce a mix of liquid fuels like gasoline, jet kerosene and diesel. In between they have to be further upgraded to meet the fuel specifications of the respective country. For example as of now the maximum limit of sulfur is 10 ppm in Europe, 15 ppm in USA and 10 ppm for on-road diesel while 50 ppm for off-road diesel in China. Meanwhile the fractions coming from the distillation tower, like light gas oil (LGO) or vacuum gas oil (VGO) from the vacuum unit have a relatively high sulfur content. So transition metal sulfides (TMS) have been traditionally employed in the refineries for hydrotreating processes. They are quite effective in removal of heteroatoms like sulfur, nitrogen, oxygen, halides and metals like V etc. However, in the petroleum industry TMS catalysts are used mainly for hydrodesulfurization (HDS) and hydrodenitrogenation (HDN). A typical composition of a TMS catalyst is cobalt or nickel promoted molybdenum-tungsten on a porous support such as alumina. They are in oxidized form when synthesized and then need to be sulfided in the presence of a sulfiding agent to form the active sulfided phase. These TMS catalysts have been found potent even for HDO reactions due to the similarity between the sulfur and oxygen atom.

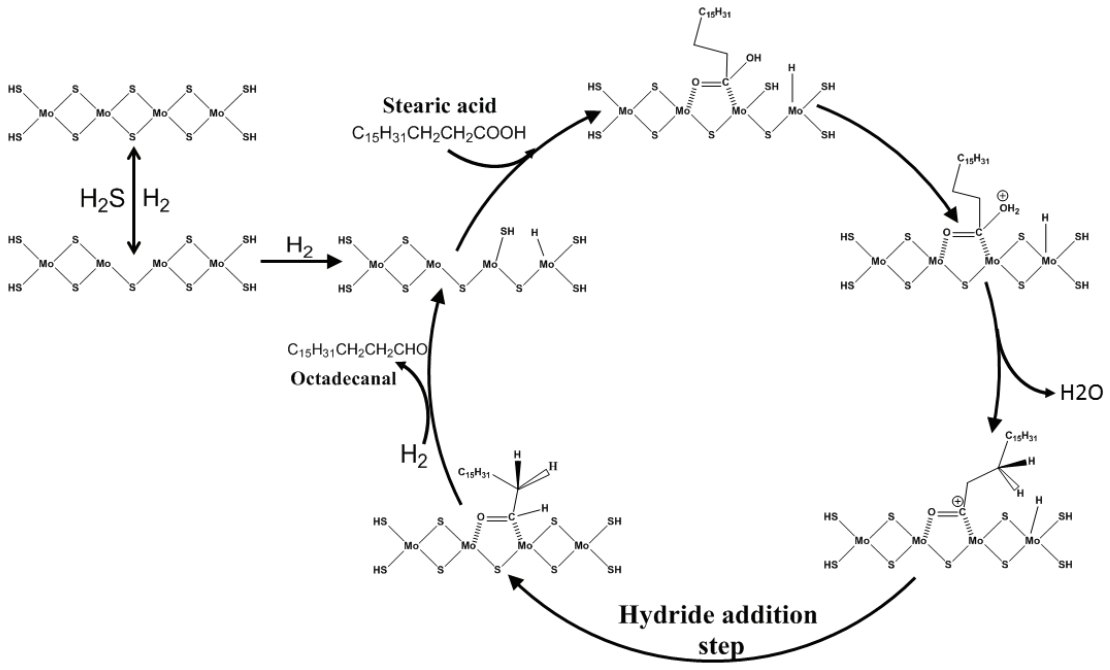

Fig 2.3 Catalytic cycle for first step of conversion of stearic acid (SA) to octadecanal (C18=O) in the overall reaction scheme.

Fig 2.3 depicts a proposed catalytic cycle for HDO of a FA molecule on TMS [32]. The first step is the creation of sulfur vacancies as sulfur from MoS_2 reacts with hydrogen to produce H_2S. There is always a dynamic equilibrium of these sulfur vacancies depending on H_2/H_2S ratio of the gas phase. Mortensen et al have suggested a similar catalytic cycle for a phenolic molecule that also starts with the creation of a sulfur vacancy [33]. Then a heterolytic dissociation of hydrogen molecule occurs which leads to a metal hydride (Mo-H) and sulfhydryl (-SH) group. A fatty acid molecule is adsorbed on the sulfur vacancy via its carbonyl group. This step is also consistent with that suggested by a DFT study [34]. After adsorption, the protonation of the hydroxyl group of the fatty acid molecule occurs by the SH group which is acidic in nature. In the next step, a water molecule is removed in tandem with the transfer of charge to carbon. This cation species undergoes a hydride addition step to yield the corresponding aldehyde. Finally, a hydrogen molecule reacts to yield a species with metal hydride (Mo-H) and sulfhydryl (-SH) which completes the catalytic cycle for conversion of stearic acid to octadecanal. NiMo (CoMo) catalysts were the first to be employed for the deoxygenation of molecules containing a carboxyl group like TGs, esters and FAs. Craig et al employed the sulfided form of transition based commercial catalysts for hydroprocessing of different vegetable oils like canola oil, palm oil, and soybean oil and renewable feedstocks like tall oil [35]. It yielded liquid paraffinic hydrocarbons in the C_{15} -C_{18} range with high cetane values. Laurent and Delmon tested hydrodeoxygenation of model compounds containing ester groups over CoMo/y-Al_2O_3 and NiMo/y-Al_20_3 catalysts [36]. They made an intriguing observation that the selectivity for the decarboxylation route decreases with the conversion of acids as there might be a competitive adsorption between the carboxylated reactants and hydrogen on the active sites. A comparative study over sulfided Ni, Mo and NiMo catalysts determined that Ni and Mo catalysts produce almost exclusively C_{17} and C_{18} hydrocarbons, respectively, while NiMo yields both hydrocarbons. Also it was concluded that the Ni/(Ni+Mo) ratio (range 0.2 to 0.4) is not so critical for the activity and selectivity of these catalysts

during HDO of TGs [37]. It is known that for traditional TMS catalysts employed for the HDS reaction, a ratio of 0.3 is preferred [38]. In another study to understand the exclusive role of active metal species and to separate the influence of support, unsupported TMS catalysts were tested [39]. Unsupported CoMo and NiMo catalysts were synthesized by the hydrothermal method then used in deoxygenation of vegetable oils. Based on the temperature programmed reduction (TPR) and experimental results, it was proposed that the Ni promoted catalysts have a higher hydrogenation activity attributed to an improved ability to create sulfur vacancies at lower temperature while CoMoS catalysts facilitated C-C bond cleavage on the saturated sites. These unsupported catalysts offer insignificant external mass transfer resistance. There was a recent study which comprehensively looked at the HDO of a range of model compounds (methyl oleate, oleic acid, triolein) over NiMo sulfide catalysts. It looked into the effect of temperature and pressure on the activity and selectivity during HDO. Even though NiMo and CoMo catalysts are widely popular for the refinery scale production of biofuels, there is still extensive research ongoing on novel catalysts for upgrading of FAs etc.

2.3 Other catalyst systems for HDO of FA

It is often debated that sulfided catalysts are not the best candidates for the upgrading of renewable feedstocks containing oxygen. This is mainly due to the reasons that sulfur leaching from these catalyst systems would contaminate the final product since oils from bio-origins have a low innate sulfur content. Many of these “sulfur-fee” alternative catalyst systems involve noble metals. The high cost of noble metals could be a barrier for scale-up of these catalyst systems, but they have contributed to develop an understanding of reaction mechanisms. In one pioneering work, Murzin and coworkers screened a broad range of catalysts - Ni, Mo, Pd, Pt, Ir, Ru, Rh, and Os on Al_2O_3, Cr_2O_3, MgO, and SiO_2 and activated C for deoxygenation of SA in a batch reactor. They found that Pd/C was the most active catalyst and established the promoting effect for deoxygenation in the following order Pd>Pt>Ni>Rh>Ir>Ru>Os [40]. However, all these catalyst systems are essentially only exclusively active for the decarbonation route. A novel sulfur-free catalyst with Ni supported on zeolite HBeta was used for deoxygenation of microalgal oil rich in FAs [41]. It was reported that this catalyst had a high selectivity for the HDO route i.e. C_{18} products with less than 1% of cracking. In a very recent study, bimetallic Pd-Au catalysts was postulated to be more stable than Pd/SiO_2 which deactivates rapidly during deoxygenation of OA due to self-poisoning of reactant molecules [42].

2.4 Catalyst Deactivation during HDO of FA

TMS catalysts are quite versatile and are effective for the hydrogenolysis of the bond between carbon and heteroatoms (like S, N, O etc.). These reactions occur on the active sites of the catalysts. But with time and exposure to feed these catalysts eventually undergo some degree of deactivation. It could be due to different reasons including loss of active sites, blocking of pore mouths, sintering etc. Although with respect to deactivation of TMS during HDO of FA and similar molecules, it mostly occurs due to the following phenomenon:

a. Loss in sulfidity of the catalyst

b. Coking

c. Inhibition due to water

d. Poisons present in renewable feedstocks

As the TMS catalysts are most active in the sulfide phase, a sulfiding agent like H_2S or DMDS has to be co-fed to keep the catalysts sulfided, unless H_2S or other sulfur containing compounds are formed due to desulphurization reactions. TMS catalysts based on MoS_2, have MoS_2 as a monolayer or clusters of slabs distributed over a support, such as alumina, surface. These hexagonally shaped slabs have coordinatively unsaturated sites (CUS) a.k.a sulfur vacancies [24, 38]. These vacancies are of a Lewis acid character and it is where O containing molecules (like oxygen in the carboxyl group of FAs) are adsorbed and undergo heterolytic cleavage. The role of the promoters like Ni (or Co) is to decrease the interaction of MoS_2 with alumina which results in considerably more active sites when compared to unpromoted MoS_2. However, it is plausible that some reactant molecules (like carboxylates) or poisons (like alkalis in renewable feeds) bind strongly or even irreversibly to subdue the labile nature of these sulfur vacancies. Since the sulfur content of renewable feeds rich in FAs like waste cooking oil, tall oil etc. is usually very low, during their upgrading a continuous input of a source of sulfur is needed. There are a few studies which have covered different aspects of the pertinence of keeping the catalysts in sulfided form [43-45].

In one of the seminal studies by Laurent and Delmon, the influence of H_2O, H_2S and NH_3 on NiMo and CoMo catalyst during deoxygenation on carboxylic esters were explored [46]. The activity of NiMo catalyst was found to be more sensitive compared to CoMo for maintenance of the sulfide phase during HDO of a carboxylic ester group [47]. It was also reported that hydrogen sulfide results in increased selectivity towards the decarboxylation route. To compare the effect of different sulfiding agents, Senol et al investigated HDO of aliphatic esters on NiMo and CoMo catalysts while varying the concentration of H_2S and CS_2 [44]. The promotion effect of H_2S on the total conversion of esters was found to be linear to its concentration, as it resulted in increased catalyst acidity. However, CS_2 suppressed the acid-catalyzed reactions resulting in lower HDO conversions. In another study, it was shown that the elimination of oxygen from the oils was enhanced when sulfiding agent (DMDS) was co-fed with the rapeseed oil [48]. Also, it was exhibited that in absence of sulfur in the feedstock, the changes in the active phase of catalyst were irreversible such that the next introduction of sulfur with feedstock resulted in only a partial revival of the catalyst activity. In this elaborative study, the influence of H2S on HDO of different model compounds like methyl oleate, oleic acid and triolein was studied [49]. It was observed that in the absence of H_2S there is a gradual drop in the catalyst activity for all three model compounds. Also, on increasing the H_2S concentration the selectivity for decarbonated (C17) products increased which suggests that H_2S cause inhibition of direct-HDO route.

Catalyst coking occurs when adsorbed species polymerize or condense into complex larger units in the catalyst pores. This phenomenon could have a deteriorating impact on the pore volume and available surface area of the catalyst. Coking is known to be ubiquitous and inevitable, but it is aggravated by feeds containing aromatics or heterocyclics, or in a hydrogen deficient environment or due to the presence of water. Immediate catalyst deactivation due to coking was observed during deoxygenation of unsaturated FAs over Pd/C at 300 °C under a scarce hydrogen (1 vol%) environment in dodecane as a solvent [50]. There was a related study to understand the nature

of deactivation on supported Pd catalysts [51]. An extensive characterization was done using XPS and TEM to conclude that there was no oxidation of the Pd surface with no sintering of Pd particles. Physisorption and chemisorption results suggested that a large loss of surface area and pore volume which pointed to the strong adsorption of organic species. In another study, the deactivation due to coking was studied as a function of the length of the catalyst bed [52]. The coke formation in the pores and on the catalyst surface was attributed as the main reason for catalyst deactivation. The coking profile of catalyst bed indicates that the larger pores of catalyst narrowed down due to gradual coking while smaller pores were obstructed partially or completely.

Since, biomass-based feedstocks contain a considerable amount of oxygen, as a result water is one of the common by-products from HDO reactions. The water molecules can interact with active sites or with the hydroxyl groups of the support (eg. Alumina) to affect the catalyst performance. The presence of water caused only a small decrease in the rate of reaction for Ni promoted molybdenum catalysts while for CoMo catalyst the rate of reaction dropped by 20% at the highest water concentration (1.7 mol/l) tested [46]. In one of the studies included in this thesis also found the same result that the water did not affect the HDO activity for NiMo catalysts [53]. Also, catalyst activity could be inhibited due to the presence of water as it can oxidize the active sulfide phase of these catalysts. There was a minor negative effect on the HDO activity at lower (<5000 ppm) concentrations of water, while at higher amounts the effect was neutral [49]. It was hypothesized that water could play a role in the keto-enol isomerization step which would have resulted in slightly higher activity for the direct-HDO route. Overall, to summarize the effect of water on HDO activity from above mentioned studies, there is a small negative impact at lower concentrations of water while it remained constant at higher water concentrations. It is difficult to say about the exact concentration at which the influence of water on catalyst activity starts to appear because of the different experimental conditions in these studies.

Senol et. al. investigated the effect of water on the activity of NiMo and CoMo catalysts during the HDO of aliphatic esters. Also, they evaluated the results if H_2S is co-fed with water[54]. The deoxygenation activity of the catalyst decreased on increasing the concentration of water in the feed for both catalysts. The drop in the yields of hydrocarbon products was more remarkable for Ni promoted compared to Co promoted catalysts. Interestingly, when H_2S was introduced in addition to water then the catalysts recovered their activities. NiMo catalyst recovered to the same level as the baseline while CoMo activity reached even a higher value. Since, water would always be present during HDO reactions, it becomes critical to have also sulfur present to maintain the catalyst activity and desired product quality.

Yoshimura and co-authors investigated upgrading of different waste feedstocks like waste cooking oil and liquid trap grease to hydrocarbons over sulfided catalysts [55]. This work did not study the contaminants in these waste feedstocks, however they found a change in product distribution of the products with time on stream. It was proposed that the active sites for hydrogenation in the CoMo catalyst were poisoned which resulted in the increase of unsaturated products with the elapse of reaction time. Also, the issue of sulfur leaching into products was reported for Co based catalysts which could explain the deactivation of catalysts to a certain extent. On the other hand, NiMo and NiW catalysts maintained their hydrogenation activity during the HDO of these low-grade waste oils in this study. In a similar study by Kubicka et. al, the catalyst deactivation was

studied during hydrodeoxygenation of waste vegetable oils [48]. A set of rapeseed oils from different stages of processing with varying amounts of different contaminants like alkali metals (K, Na etc.), P in form of phospholipids and free fatty acids were examined as feedstocks. The HDO experiments indicated an interesting phenomenon that the deoxygenation rate depends on the balance of cations (alkalis) and anions (phosphates from phospholipids) and not only on the absolute amount of impurities. Also, it was highlighted that the phospholipid molecules would decompose at the reaction conditions (310 °C and 35 bar) to yield alkali phosphates which would become deposited at the beginning of the catalyst bed such that the feedstock after that would be free of contaminants and deoxygenated to virtually the same extent. One of the feedstocks tested was waste rapeseed oil (separated during a water treatment process) that caused a damaging effect on the catalyst. It contained a high amount of alkalis and free fatty acids however, deactivation was majorly attributed to alkali metals. Another feedstock which is from a waste stream from vegetable oil processing units called trap grease was evaluated. It contained significant amounts of phosphorus and free fatty acid acids. The phospholipids species were different in trap grease as phosphate groups are acidic, as there is a low concentration of alkalis, while in rapeseed oil-based feedstocks phosphates are neutral, as counter ions (alkalis) are present. It was postulated that phospholipid would decompose to phosphoric acid which acts as an oligomerization catalyst for unsaturated hydrocarbons which would have accelerated the coke formation and deactivation. With phospholipids (from trap grease) the catalyst deactivation was so severe that it led to plugging of the reactor and pressure build-up and the experiment was shut-down early. A gradual loss of catalyst activity was observed for other feedstocks containing only a small amount of alkalis or phospholipids. There are a few patent studies as well which have highlighted that biomass-based feedstocks could have contaminants like chlorides, phosphorus, alkali metals and iron [56, 57]. It was found that a significant pressure drop across the catalyst bed developed during the hydrotreatment of bio-oil which resulted in untimely shutdown of reactors. It was suggested that the impurities such as phosphorus and alkali metals may be responsible for the deactivation of catalyst while a high iron content in the feed caused plugging of the catalyst bed. This study suggests that the iron content of the feedstock being hydrotreated should be less than 0.25 w-ppm for a smooth and efficient plant operation. It was claimed that the iron had the strongest correlation for build-up of catalyst bed pressure drop among other contaminants like P, Ca, Na and Mg based on the various feedstocks tested [57]. Another study in which different impurities like chlorine and potassium were evaluated is worth mentioning, however feedstocks in this study were not based on fatty acids and the catalyst tested was NiMo supported on ZrO_2[25]. To test the effect of potassium, the $NiMoS_2/ZrO_2$ catalyst was impregnated with potassium nitrate such that the molar ratio of K/(Ni+Mo) was 1. There was a large drop in the deoxygenation activity of the catalyst by around 80% compared to the baseline experiment. It was suggested that the vacancy sites on the slab edges of MoS_2 are readily blocked by potassium resulting in deactivation. To test the stability of this catalyst system, 0.3 vol% of 1-chlorooctane was employed as a model compound to represent organically bound chlorine. A drop in conversion was observed, however it remained stable during the co-feeding of chlorine compound. This suggests that the chorine is competitively inhibiting the active sites. It was proposed that the chlorine affected the hydrogenation activity as the concentration of unsaturated products increased. Also, it was found that the deactivation due to chlorine is reversible as the activity started to increase when chlorine feed was cut-off. Overall, there were limited studies which have explored the deactivation of catalyst due to impurities present in

renewable feedstocks. Thus, with the increasing production and adoption of advanced biofuels, it becomes pertinent to further study the catalyst deactivation and to contribute to the knowledge with high relevance to industry.

3 Methods

3.1 Catalyst Preparation

The γ-Al_2O_3 (PURALOX®, Sasol) with particle size range 150–200 µm and a surface area (199m^2/g), and a pore volume (0.48 ml/g) was used as support for preparation of NiMo and unpromoted Mo catalysts. These two catalyst systems were synthesized by using a conventional impregnation method on the alumina support using aqueous solutions of the following metal precursors, $(NH_4)_6Mo_7O_{24}{\cdot}4H_2O$ (Sigma Aldrich) and $Ni(NO_3)_2{\cdot}6H_2O$ (Sigma Aldrich). In the first step of the sequential impregnation, 15 wt% Mo was added dropwise from an aqueous solution of the Mo precursor into an aqueous solution of alumina and then freeze dried to remove water. A portion was removed at this stage and used as the unpromoted Mo catalysts for HDO experiments after calcination. Calcination was done at 450 °C with a ramp rate of 10 °C per min in air for 2 h. The second step was the loading of Ni. An aqueous solution of nickel salt was added to the aqueous solution of material prepared in the previous step and then dried to remove water. Again, this sample was calcined at 450 °C in air. These two catalyst samples were marked as Mo/Al_2O_3 and NiMo/Al_2O_3 [58]. This protocol was followed for Paper I, II and IV whereas the steps were slightly different for the catalyst employed in Paper III. In Paper III, the alumina support was in the form of larger particles instead of a powder. The catalyst prepared for placement in the refinery was supported on alumina spheres of diameter 4 mm, while for the laboratory batch reactor experiments in the same study, the catalyst was on gamma-alumina spheres (Sasol - 1.8/210) with a diameter range of 1.70-1.90 mm. The precursors for Ni and Mo were the same as above. However the major difference was in the drying step. The samples were dried by leaving in a fume-hood for overnight and further dried in a vacuum oven at 110℃ for 3 hours and later calcined at 450℃ for 4 hours with a temperature ramp rate of 5℃/min. The final metal loadings were – Ni (1.8%) and Mo (11%) on the 4 mm alumina spheres and Ni (2%) and Mo (12%) on the 1.8 mm alumina spheres, as determined via ICP analysis.

3.2 Other materials

Oleic acid (Fluka, technical grade 90%) was employed as a feedstock in Paper I and II. It was used as received. This technical grade OA mainly consisted of the two isomers of oleic acid (86%). The rest was other fatty acid impurities - 9-Hexadecenoic acid (palmitoleic acid) about 5%, hexadecanoic acid (palmitic acid) about 4%, tetradecanoic acid (myristic acid) about 3%, while

stearic acid and eicosenoic acid were less than 1% as per the GC analysis. We will refer to these acids, other than OA, as “Other acid impurities”. For Paper III and IV, stearic acid (Merck, reagent grade 95%) was used as a model compound. It contained only 1.5% tetradecanoic acid (myristic acid) impurity as determined by GC analysis. Octadecanal (stearaldehyde) and octadecanol (stearyl alcohol) were also employed in this study. Octadecanol of 99% grade was purchased from Sigma and used as is. Octadecanal was synthesized using a mild oxidizing agent (pyridinium chlorochromate) following a procedure as described elsewhere [59].

The iron oleate (FeOA) complex which was employed as poison in the HDO experiments in Paper I, was synthesized following a procedure reported elsewhere [60]. For Paper II, the poison compound was a phospholipid called L-α-Phosphatidylcholine (99%, Sigma-Aldrich, St. Louis, MO, USA), see Fig 3.1. We will abbreviate it, from here on, as PC. This molecule has a glycerol backbone with a hydrophobic long hydrocarbon chain with fatty acid residues linked via an ester group to a polar phosphate group and an organic group, called choline containing nitrogen. The approximate fatty acid composition of PC was - 33% 16:0 (palmitic), 13% 18:0 (stearic), 31% 18:1 (oleic), and 15% 18:2 (linoleic). Also, an additional experiment was done using choline hydroxide (48% in water, Fluorochem, Glossop, UK) to distinguish the effect of the choline moiety from the rest of the phospholipid molecule.

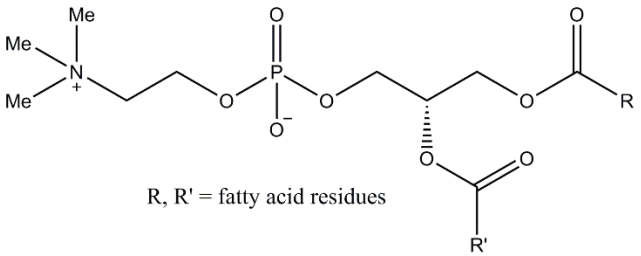

Fig 3.1 L-α-Phosphatidylcholine is the poison complex used in Paper II.

In Paper III, the poisons used were - Iron stearate, 1,2-Dipalmitoyl-sn-glycero-3-phosphate monosodium (3-sn-Phosphatidic acid) and potassium nitrate with their structures given in Fig 3.2. The iron stearate synthesis was same as that for iron oleate [60] whereas phosphatidic acid containing P and Na and potassium nitrate for K were purchased from Merck.

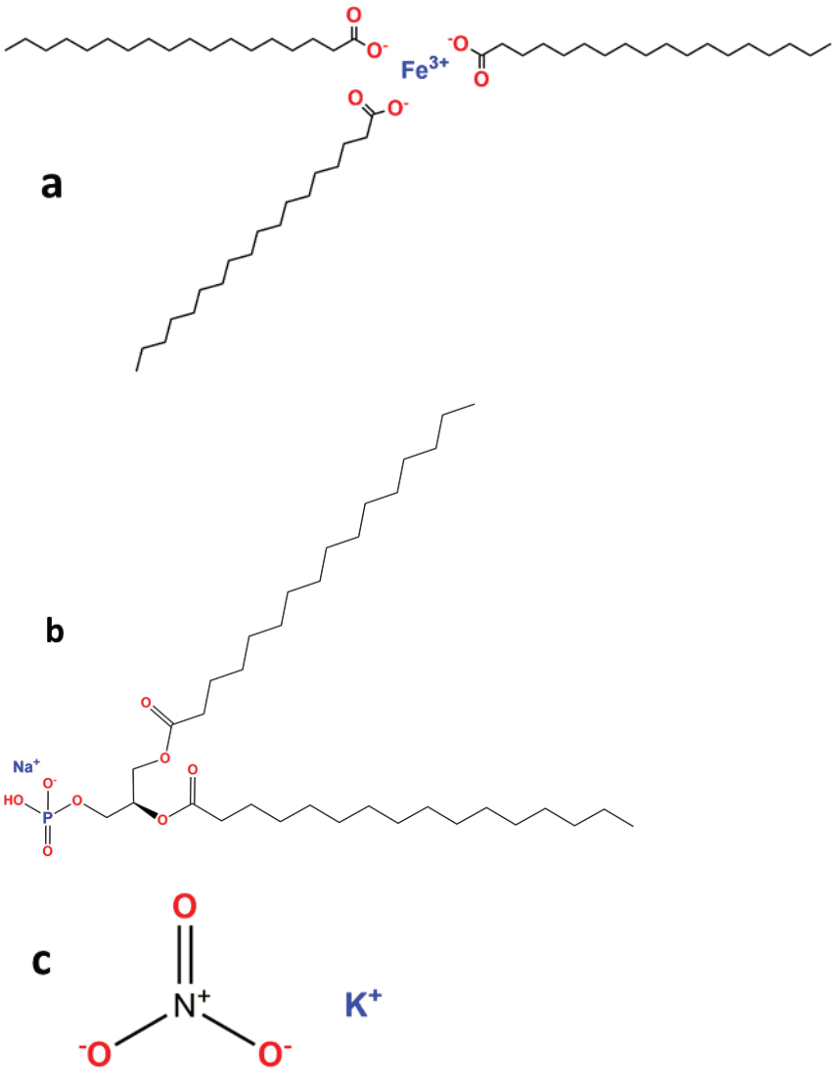

Fig 3.2 Structure of poison complexes used in lab HDO experiments – a. Iron stearate b. 1,2-Dipalmitoyl-sn-glycero-3-phosphate monosodium (3-sn-Phosphatidic acid) c. Potassium nitrate.

3.3 Catalytic activity measurements

All the HDO experiments in these four studies were performed in a 300 ml stainless steel autoclave (Parr instruments) equipped with an internal stirrer. The reactor was equipped with a liquid sampling line to collect small aliquots (0.8-1.2 ml) during the experiment. The sampling line was wrapped with heating tape to keep it warm and prevent solidification of the samples.

Table 3.1 Concentrations of poison in weight ppm studied for each catalyst and experiment abbreviations (Paper I).

Poison in feed (ppmw)	Catalyst	
	NiMo/Al_2O_3	***Mo/Al_2O_3***
0	NiMo_0 Fe	Mo_0 Fe
20	NiMo_20 Fe	-
100	NiMo_100 Fe	Mo_100 Fe
500	NiMo_500 Fe	Mo_500 Fe
2000	NiMo_2000 Fe	-

In the poisoning study with FeOA for Paper I, 1 g of catalyst and oleic acid (15 wt%) in dodecane (Sigma Aldrich) with a total volume of the reaction mixture of 150 ml was employed. A set of experiments with Mo/Al_2O_3 and $NiMo/Al_2O_3$ with different iron oleate (Fe poison) concentration was planned as given in Table 3.1. Poison (FeOA) was added at the beginning of the experiment. The poison concentration is reported in ppmw, i.e. milligrams of iron per weight (kg) of total liquid feed to the reactor. In Table 3.1; abbreviations for experiments are denoted by: (catalyst used) (concentration of poison), e.g. "NiMo_X Fe" where X is the concentration of iron in ppmw with respect to the total feed. DMDS (Sigma Aldrich) was used for the pre-sulfiding step as described elsewhere [61]. Meanwhile, a small amount of DMDS (0.1 ml) was added to the reaction mixture in each HDO experiment to maintain the sulfidity of the catalyst. Reactor conditions were kept constant for all experiments in this study - 60 bar H_2, 325 °C and with a stirring rate of 1000 rpm for 330 min. At the beginning of an experiment, first the reactor was flushed with nitrogen to remove any air, then with hydrogen. Then it was depressurized to 0.1 bar gauge and heating was switched on with a low rate (150 rpm) of stirring. After reaching the desired temperature, stirring was increased to 1000 rpm. Hydrogen was introduced at this point and this moment was considered as the start of experiment. Liquid samples were collected at progressive time intervals of – 15, 35, 55, 95, 155, 215, 275 and 330 min. At the time of liquid sampling, stirring was temporarily stopped to avoid any catalyst carryover. Fine particles of catalyst could damage the seals in the valves on the liquid sampling line. Pressure loss due to collection of liquid samples was replenished by topping up with hydrogen to maintain the same pressure throughout the experiment. Spent catalyst was recovered after the experiment after filtering with 200 ml of warm ethanol and dried for subsequent characterization. The mole balance was closed on the basis of initial moles of the feed (OA or SA) added to the reaction mixture and the measured concentrations of all components in the product samples. The mole balance was always within the range of ±10% unless otherwise stated.

In Paper II with PC complex, 0.5 g of catalyst with 10 wt% of oleic acid and solvent as dodecane with a total volume of 150 ml was used. The reaction conditions were 320 °C, with 54 bar of H_2 at a stirring rate of 1000 rpm and liquid samples were collected at 30, 60, 120, 180, 240 min time

intervals. The rest of the steps were same as for Paper I. The list of the experiments carried out in this study are presented in Table 3.2.

Table 3.2 Concentration of poison element in feed per mass of catalyst and abbreviations for the batch reactor experiments.

Name of the Experiment	Poison Compound	Poison in feed per mass of catalyst (wt%)		
		PC	Choline	Water
No Poison	-	-	-	-
PC 0.2	Phosphatidylcholine (PC)	0.2%	-	-
PC 0.4	Phosphatidylcholine (PC)	0.4%	-	-
PC 0.9	Phosphatidylcholine (PC)	0.9%	-	-
PC 1.3	Phosphatidylcholine (PC)	1.3%	-	-
Choline	Choline hydroxide	-	1.3%	1.3%
H_2O	Water	-	-	1.3%

Paper III consists of two segments – First the characterization of the spent model catalyst placed in the refinery operation and different protocols tested to revive the catalytic activity of spent catalysts. Then the second segment, focused on how different key poisons, identified in the spent refinery catalyst, influenced catalytic activity and spread through the catalyst particles.

Fig 3.3 gives the project flow scheme of first segment of Paper III. NiMo catalyst spheres were prepared in our labs and sent to the refinery. The catalyst was kept in a specialized open canister and loaded in the hydrotreater employed for the production of HVO biofuels. The catalyst canister was placed in the active bed of the reactor unit. This catalyst sample (around 100 g) was exposed to the actual feed and harsh refinery conditions. The renewable content of the processed feedstock was rich in molecules like fatty acids, alkyl esters and triglycerides etc. Also, the reactor unit was flushed with hydrogen to remove any residual hydrocarbons from the catalyst bed as per the routine shutdown procedure. This catalyst had been in the refinery for several months before it was sent to our lab for further analysis. These samples were analyzed via elemental analysis and ICP to identify and quantify different contaminants. The catalyst sample sent to the refinery was in form of spherical particles (diameter 4 mm). They were crushed and sieved to a particle range of 100-500 µm and labelled as Spent[R], where [R] represents the refinery sample. Two portions were taken from the batch of Spent[R], one was calcined at 450°C for 4 h to remove any carbon, sulfur and other volatiles and was labelled as Calcined[R], while the second portion was washed in a Soxhlet setup and labelled as Washed[R]. The washed sample (2 g) underwent two rounds of solvent extraction with the solvents hexane and ethanol (100 mL each) for 6 h. After the Soxhlet treatment, these samples were dried in a fume hood for 12 hrs. A portion of the fresh catalyst, that was retained and not sent to the refinery, was crushed to a particle range of 100-500 µm and labelled as Fresh[R]. These four samples will collectively be referred to as the "refinery samples" in the following sections of this thesis. The refinery samples were evaluated for their catalytic activity during HDO of SA at these experimental conditions - Catalyst 0.4 g, Stearic acid (SA) as feed 4 g, Dodecane as solvent 150 ml, Pressure 50 bar (H_2) and Temperature 300 °C

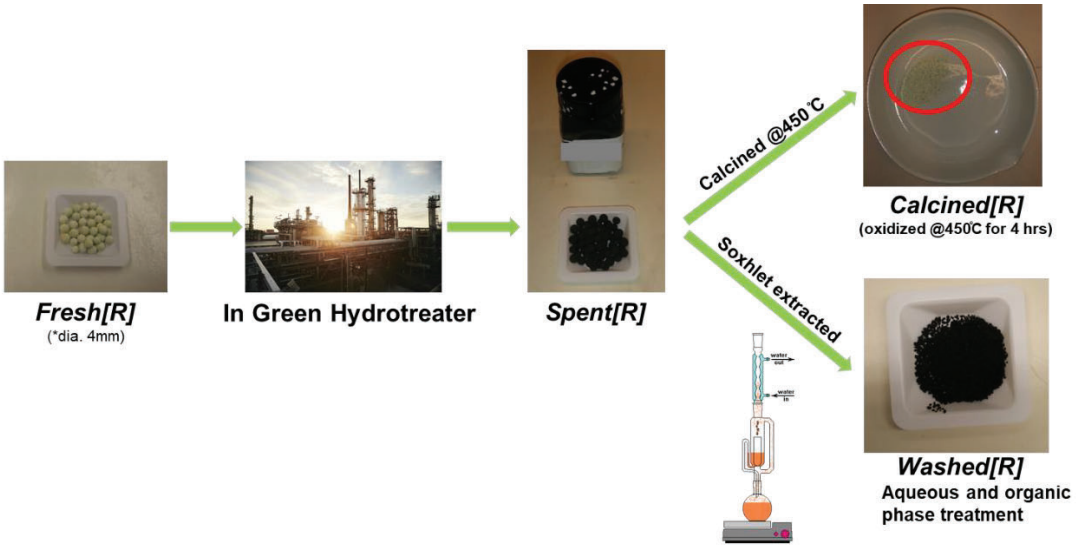

Fig 3.3 Project flow scheme for first segment of study in Paper III.

In the second segment of the Paper III, the effect of different key poisons, identified from spent refinery samples, on HDO activity was tested. Three different concentrations (1, 2 and 5 wt%) of different poisons with Fe, K and phospholipid containing P and Na were evaluated. The concentration of poisons added to the reaction mixture were on the basis of the respective element (Fe, K and P) weight to the catalyst weight. It should be mentioned that the calculation for phospholipid was on the basis of P, though it contained Na as well. The corresponding amounts of Na were 0.7, 1.5 and 3.7 wt% respectively. The experiments were named in following manner – "X y%" where X is the poison element and y is the amount of poison added. For example, "K 2%" denotes the experiment with potassium as poison and 2 wt% of poison per mass of catalyst. However, the experiments with different concentrations of phospholipids will be referred as "P/Na y%" where for the sake of clarity y% is the exact amount of P only, however it should be noted that the corresponding amounts of Na in the phospholipid are somewhat lower as mentioned above. The amount of poison compound added to the reaction mixture for P and K was determined by the number of moles of the element required and multiplying it with the molecular weight of the compound containing the poison element. It was different for Fe as the molecular formula for the iron complex is not known. So, it was based on the ICP analysis of iron stearate synthesized in the lab. The following two formulas were used to calculate the respective amounts of poison in wt% and mass of poison complex to be added to the reaction mixture.

$$\text{Poisoning element dosage (wt\%)} = \frac{amount\ of\ poison\ element\ (g)}{wt.of\ catalyst\ (g) * 100}$$

$$\text{Mass of poison complex} = \frac{poison\ element\ (wt\%) * Molecular\ weight\ of\ poison\ complex}{Atomic\ mass\ of\ poison\ element * 100}$$

Also, three additional experiments were done, first with no poison to establish the baseline activity, second with iron nitrate ($FeNO_3$) to distinguish the effect due to anions with different stearic hinderance potential i.e. nitrate and stearate and the third to examine the combined effect using a mix of all three poisons (Fe, K, P and Na). The last two experiments with iron nitrate and mix of poisons were denoted as "FeN 2%" and "Mix 2%" respectively. Table 3.3 lists all the

experiments in the second segment of Paper III. The poisoning complexes employed were Iron stearate, potassium nitrate and 1,2-Dipalmitoyl-sn-glycero-3-phosphate monosodium (3-sn-Phosphatidic acid). The catalyst used was NiMo supported on gamma-alumina spheres with a diameter range of 1.70-1.90 mm. HDO experimental conditions for this segment were - Catalyst 1 g, Stearic acid (SA) as feed 4 g, Dodecane as solvent 150 ml, Pressure 50 bar (H_2) and Temperature 300 °C.

Table 3.3 Concentration of poison element in feed per mass of catalyst (in ppm) and abbreviations for the batch reactor experiments.

Name of the Experiment	Poison Compound	Poison element in feed per mass of catalyst (in ppm)			
		Iron (Fe)	Potassium (K)	Phosphorus (P)	Sodium (Na)
Fe 1%	Iron Stearate	10000	-	-	-
Fe 2%	Iron Stearate	20000	-	-	-
Fe 5%	Iron Stearate	50000	-	-	-
P/Na 1%	3-sn-Phosphatidic acid	-	-	10000	7000
P/Na 2%	3-sn-Phosphatidic acid	-	-	20000	15000
P/Na 5%	3-sn-Phosphatidic acid	-	-	50000	37000
K 1%	Potassium Nitrate	-	10000	-	-
K 2%	Potassium Nitrate	-	20000	-	-
K 5%	Potassium Nitrate	-	50000	-	-
Mix 2%	Mixture of above three	6666.7	6666.7	6666.7	5000
FeN 2%	Iron Nitrate	20000	-	-	-

For the kinetic study (Paper IV), the same experimental setup was used as above, though only a 0.04-0.4 g of NiMo catalyst was used for HDO of different feeds like stearic acid (SA), octadecanal (C18=O), octadecanol (C18-OH) and mixture of stearic acid & octadecanol in dodecane with the same total liquid volume of 150 ml. Reaction conditions for the baseline experiment were- 5 wt% of stearic acid, 50 bar H2, 300 °C, stirring speed of 1000 rpm and 0.4 g of pre-sulfided catalyst. Table 3.4 lists all the experiments carried out in the second study with different parameters tested. Most of the protocols were kept the same as the previous study. The same conditions were used for sulfiding of the catalyst but DMDS was not added at the beginning of the reaction to avoid any side reactions. During thermal decomposition of DMDS, hydrogen is consumed while methane is produced which is an additional process that would have to be considered for the kinetic modeling. The pressure drop from sampling and pressure increase from hydrogen top-up were duly recorded at each sampling interval. Gas samples were collected at the end of the experiment. An additional baseline experiment was done to collect gas samples at 40 and 90 min intervals.

Table 3.4 Reaction conditions for the kinetic experiments.

Feed component	Pressure (bar)	Temperature (C)	Feed (wt%)	Stirring (RPM)	Catalyst wt. (g)
Stearic acid	40,50,70	300	5	1000	0.4
Stearic acid	50	275,300,325	5	1000	0.4
Stearic acid	50	300	2,5,8	1000	0.4
Stearic acid	50	300	5	500,900,1000	0.4
Stearic acid, Octadecanal, Octadecanol	50	275	5	1000	0.04

3.4 Product analysis

Liquid samples from HDO experiments were analyzed using a GC-MS equipped with a flame ionization detector (FID) (Agilent 7890-5977A). Data analysis was done using MassHunter data analysis software with NIST library. It had a non-polar HP-5 capillary column (L=30m, Dia.=0.25mm & Film=0.25 µm). BSTFA (N,O-bis(trimethylsilyl) trifluoroacetamide (Sigma Aldrich, ≥99.5%) was used to do silylation of the samples. Silylation increases the volatility and elution of oxygenate species so that peaks in the chromatogram are well separated and sharp. A three-point calibration of the FID was done with high purity external standards of oleic acid, stearic acid, 1-octadecanol, octadecanal, octadecane, heptadecane, hexadecane, pentadecane and tetradecane. Moreover, the peaks from other minor compounds were quantified using the effective carbon number method based on the closest related calibrated compound.

The following are the formulas used in this thesis for quantities that assess the experimental results:

$$\text{Conversion of oxygenates} = \left(1 - \frac{moles\ of\ oxygenates\ in\ the\ sample}{moles\ of\ starting\ oxygenates}\right) \times 100$$

$$\text{Yield\% of C17 \& C18 and minor products} = \frac{moles\ of\ product\ produced}{moles\ of\ reactant\ in\ feed} \times 100$$

$$\text{Initial rate of reaction} = \frac{Initial\ mmoles\ of\ oxygenates - mmoles\ of\ oxygenates\ in\ first\ sample}{time\ (hr) * wt.of\ catalyst\ (g)}$$

$$\text{Rate of formation of C17} = \frac{mmoles\ of\ \mathrm{C17}\ in\ first\ sample}{time\ (hr) * wt.of\ catalyst\ (g)}$$

$$\text{Rate of formation of C18} = \frac{mmoles\ of\ \mathrm{C18}\ in\ first\ sample}{time\ (hr) * wt.of\ catalyst\ (g)}$$

$$\text{Selectivity of C17} = \frac{mmoles\ of\ \mathrm{C17}\ at\ end\ of\ the\ reaction}{mmoles\ of\ \mathrm{C17}\ \text{and}\ \mathrm{mmoles\ of\ C18}\ at\ end\ of\ the\ reaction}$$

$$\text{Selectivity of C18} = \frac{mmoles\ of\ \mathrm{C18}\ at\ end\ of\ the\ reaction}{mmoles\ of\ \mathrm{C17}\ \text{and}\ \mathrm{mmoles\ of\ C18}\ at\ end\ of\ the\ reaction}$$

Unsaturated isomers of C17 and C18 are formed during the penultimate step of the reaction scheme, but they are readily hydrogenated to yield final alkane products. Thus, all isomers of

alkenes and alkanes have been combined and will be reported henceforth together as C17 and C18 products.

3.5 Catalyst characterization

3.5.1 Nitrogen physisorption

For supported catalysts, the number of active sites depends on the surface area, and surface area is dependent on parameters like particle size and morphology, surface texturing, and porosity. Porosity and pore structure are very important factors affecting the activity of a given catalyst. Nitrogen physisorption is a phenomenon in which, when N_2 gas comes in contact with a solid surface (at 77k), a specific number of molecules are attracted to the surface of the solid by van der Waals forces. The number of physisorbed molecules depends on the relative pressure (p/p_0) of the nitrogen gas at equilibrium. N_2 physisorption was carried out at -196 °C on a Micromeritics ASAP 2010 instrument for pore structure analysis. Catalyst samples (approx. 300 mg) were degassed at 225 °C under vacuum conditions for 3h. Specific BET surface area (SBET) was calculated from the adsorption data in the relative pressure range of 0.05–0.2. The pore size distribution curves were calculated using the Barrett–Joyner–Halenda (BJH) method based on analysis of the desorption branch of the isotherm.

3.5.2 Elemental analysis

Carbon, hydrogen and sulfur content of the spent catalyst samples were determined by elemental analysis. In elemental analysis, the sample undergoes combustion at 800 °C in excess of oxygen. Then the gaseous combustion products are trapped. These gases are separated through a column and measured by a thermal conductivity detector (TCD). C and H content was determined on a CE Instruments elemental analyzer model EA111 while for S, analysis was carried out on a Fisons elemental analyzer model NA2000.

3.5.3 ICP analysis

For quantification of the metal contents (Ni, Mo and Fe), inductively coupled plasma sector field mass spectrometry (ICP-SFMS) technique was employed. The sample is dissolved in HNO_3 and digested in a microwave oven, and then fed into the instrument where the sample is ionized with inductively coupled plasma (ICP) and then quantification and separation of ions is done using a mass spectrometer. In this study, ICP analysis was carried on a Thermo Element XR instrument.

3.5.4 Temperature programmed reaction

Temperature programmed reaction of spent catalysts with hydrogen was carried out to gain insights about the effect of poison (Fe) on sulfur vacancies (CUS). An amount of 50 mg of catalyst sample was placed in a quartz tube under a continuous flow of 20 ml/min at ambient conditions. Catalyst samples compared were - (NiMo_0Fe and NiMo_500Fe). These samples were degassed in a stream of argon gas at 350 °C. Then they were cooled down to ambient temperature after which they were exposed to a stream of Ar containing 100 ppm hydrogen for 1 h. Then the concentration of hydrogen in the gas stream was increased to 400 ppm and maintained at that level for 30 min. After that, the temperature was ramped up to 800 °C at a rate of 10 °C/min during continuous dosing of hydrogen. The temperature was finally maintained at 800 °C for 30 min. The

H_2 and other eluents in the outlet gas stream were monitored with a Hiden Analytical HPR 20 quadrupole mass spectrometer (MS).

3.5.5 X-ray Photoelectron Spectroscopy (XPS)

The surface composition of catalyst and the oxidation state of different species from poison complexes were examined using XPS. It was carried out on a Perkin Elmer PHI 5000 VersaProbe III Scanning XPS Microprobe. XPS analysis was used for following elements - Fe, P, K, O, S, Ni, Mo, Al and C in Paper II and III. The catalyst samples were exposed to a monochromatic Al-Kα source with a binding energy of 1486.6 eV in the vacuum chamber (less than 2×10−8 torr) and a high resolution spectra for the above mentioned elements were recorded. The raw data was analyzed using Multipack and CasaXPS software. The C1s binding energy of 284.8 eV was taken as the reference for all spectra.

3.5.6 Scanning electron microscopy (SEM)

The distribution of different contaminants through the catalyst particles was examined using a scanning electron microscope (FEI Quanta200 ESEM) which was equipped with an Oxford Inca Energy Dispersive X-ray (EDX) system. The catalyst spheres from Paper III were cut into half using a surgical knife then these hemispherical particles were put on carbon tape with the flat surface facing up. The sample chamber was evacuated at a low vacuum mode of 1 Torr. The EDX analysis was done along the radial axis of the flat surface for three different particles for each sample. The radial analysis was done at different lengths depending on the size of the spheres. For the refinery samples with a diameter of 4 mm, the analysis was done from surface (edge) to the center and from surface to a depth of 500 µm while for the samples (diameter 1.8 mm) from lab experiments, it was done from the surface (edge) to the center and from surface (edge) to a depth of 300 µm. The distribution of a given metal was calculated on an average basis for the three analyzed particles and then normalized against the maximum value in each analysis.

3.5.7 Transmission electron microscopy (TEM)

The relative distribution of poison (Fe) with respect to active metals (Ni and Mo) was determined by TEM-EDX mapping. HAADF-STEM imaging of catalysts samples after being exposed to poison under the reaction conditions was analyzed by a FEI Titan TEM, operating at 300 kV, equipped with EDX. Samples for TEM analysis were prepared by making a suspended solution in ethanol and then letting it dry on the carbon coated copper grid at room temperature. Length of slabs and stacking degree for MoS_2 was also measured using ImageJ software. TEM-EDX mapping was done at four different spots for repeatability and for sufficiently long periods in order to stabilize the signal collection.

3.6 Kinetic modeling methods

Kinetic studies are critical to connect the microscopic picture of molecules undergoing reactions to the macroscopic picture of reaction engineering which extends to commercial scale. Needless to say, kinetics is one of the key disciplines in the field of catalysis. Even, a simple model based on power-law kinetics could predict the dependence of the individual components on the rate of a

chemical process. This is critical information to predict how a reactor behaves in a given range of temperature and pressures.

3.6.1 Reactor Model

A pseudo-homogeneous ideal batch reactor was assumed for the model that comprised a set of differential equations for each component –

$$\frac{dN_j}{dt} = \sum (\gamma_{ij} r_i) W$$

where N_j is the number of moles of component j, γ_{ij} is the stoichiometric coefficient for component j in reaction i, r_i the rate of reaction of reaction i and W is the mass of catalyst. The batch reactor was assumed to operate under isothermal conditions all the time and the rates of all reactions were considered to be dependent on the concentrations of components in the liquid phase. The liquid and gas phases were considered to be in a state of quasi–equilibrium. The compositions and densities of vapor and liquid phases were determined by calculating the vapor-liquid equilibrium (VLE) based on the Predictive Soave-Redlich-Kwong (PSRK) group contribution equation of state (EOS) by Holderbaum and Gmehling [62]. There have been other studies which have suggested PSRK EOS is most suitable for VLE estimations of similar feeds containing fatty acids for HDO reactions [63]. The PSRK critical constants and group interaction parameters were taken from literature [64]. The amount of hydrogen added to the reactor at the start of the experiment was calculated by an iterative approach using the EOS. All calculations in this kinetic study were carried out using a customized MATLAB R2014b program.

3.6.2 Reaction Equilibrium

The temperature dependence of equilibrium constants (K_{eq}) for reactions were calculated from equations with the form:

$$K_{eq} = \exp(\frac{A}{T} + B\ln(T) + CT + DT^2 + ET^3 + F)$$

where the parameters A, B, C…etc. were calculated from standard state thermochemical properties of the components. In cases where published thermochemical properties were not available they were estimated from the Joback Method [65].

An equilibrium between octadecanal and octadecanol was considered which has been suggested by other studies as well. It could influence the selectivity between direct-HDO and decarbonation products. The rate of this reaction was multiplied by a driving force factor (β), that would approach zero as equilibrium is reached. This driving force factor was:

$$\beta = 1 - \frac{a_{C18OH}}{a_{C18=O} a_{H2} K_{eq}}$$

3.6.3 Parameter estimation for kinetic model

Reaction rate constants were expressed according to a modified Arrhenius equation:

$$k_i = k_{ref} exp\left(\frac{E_i}{R}\left(\frac{1}{T_{ref}} - \frac{1}{T}\right)\right)$$

This formulation was used to reduce the strong correlation between the pre-exponential factor and the activation energy. Thus the rate constant at the reference temperature (k_{ref}) and the activation energy (E) were the estimated kinetic parameters. The reference temperature used was 300°C, the mean experimental temperature.

For parameter optimization, the 'simulannealbnd' function in Matlab 2014b's optimization package was used to perform non-linear regression. Simulannealbnd is a global optimizer based on the simulated annealing method. The objective function of the parameter optimization was to minimize the sum of squares of the residuals (SSR) calculated from

$$SSR = \sum_{j} \sum_{i} w_i \left(y_{ij}^{exp} - y_{ij}^{sim} \right)^2$$

where the residuals were computed from differences between the simulated (y_{ij}^{sim}) and experimentally (y_{ij}^{exp}) measured yields of component *i* from experiment *j*. The residuals for intermediate species, with lower concentrations, were typically weighted up by a factor (w_i) corresponding to the approximate ratio of average concentrations of a high concentration component (e.g. reactants and final products) to the low concentration component.

4 Results and Discussion

This thesis is based on four independent studies presented in **Papers I, II, III and IV**. In the first study (**Paper I**), the effect of iron Fe as poison was investigated for HDO of OA over MoS_2/Al_2O_3 and $NiMoS/Al_2O_3$. In the first study, HDO experiments demonstrated the influence of a poison (Fe) on the change in activity and selectivity of two catalyst systems. Then to elucidate the role played by Fe, spent catalysts samples were characterized using the above mentioned characterization techniques. Results from temperature programmed reaction (with H_2) and TEM-EDX analysis helped to correlate the results from the experiments.

In the last study (**Paper IV**), we carried out HDO of SA at different conditions by varying parameters like – temperature, H_2 pressure, feed concentration and stirring speed. Also, reaction with other feeds like octadecanal (C18=O) and octadecanol (C18-OH) were carried out to gain a deeper understanding about the reaction scheme, and relative rates of competing reactions (e.g. decarboxylation and decarbonylation). Then, a pseudo homogeneous ideal batch reactor model, an EOS model for phase equilibrium and a kinetic model based on a proposed reaction scheme was used to predict experimental results. Results from simulations were compared to experimental results.

4.1 Fe poisoning during HDO of OA

4.1.1 HDO of OA over NiMo catalysts

A typical reaction scheme for HDO of OA, as illustrated in Fig 4.1, includes- firstly a fast hydrogenation of the double bond present on the long alkyl chain to produce stearic acid. Then the acid functionality is reduced to yield an aldehyde (octadecanal). Octadecanal is the common intermediate for the two possible routes of decarbonylation and direct-hydrodeoxygenation [20, 25, 40]. This scheme from stearic acid was also confirmed by experimental observations in the kinetic modeling study (section 4.4). So, the carbonyl group (-C=O) exhibits tautomerism to exist in the enolic form which is saturated to form 1-octadecanol [20]. The alcohol is further deoxygenated to give unsaturated products. A number of alkene isomers were seen in the GC chromatogram which suggests that a carbon cation intermediate was involved. Alkene isomers were hydrogenated to octadecane. While for the DCOx route, oxygen is removed in the form of CO/CO_2 molecules either from Octadecanal or Stearic acid to produce C17 alkenes. They are subsequently hydrogenated to form heptadecane as the final product. Selectivity from these two

main routes were quantified by summing the hydrocarbons (both alkenes and alkanes) having the same carbon length. The oxygenate conversion was based on a sum of the oleic and stearic acid remaining.

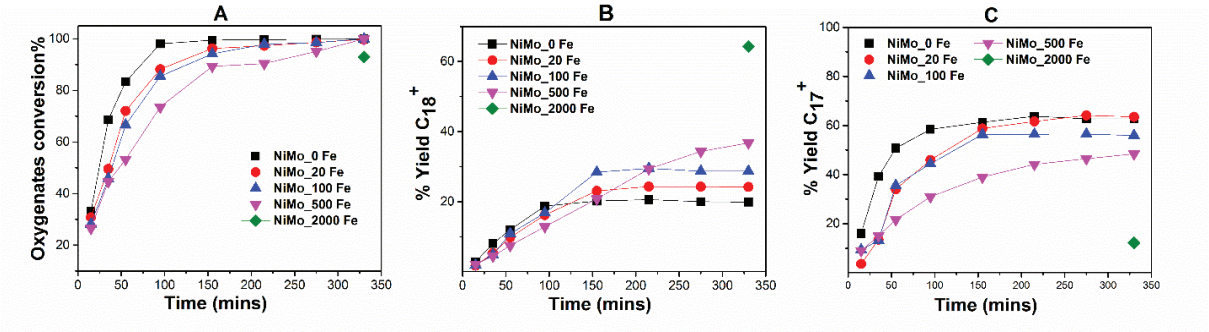

Fig 4.1 A, B and C: Oxygenate conversion and selectivity for major products during HDO of Oleic acid over NiMoS/γ-Al_2O_3 with varying concentrations of poison (Fe-oleate).

In Fig 4.1, the yield of the major products including "C17+" (sum of heptadecane and isomers of heptadecene) and "C18+" (sum of octadecane and isomers of octadecene) are depicted along with oxygenate conversion for varying concentration of poison. It can be observed in Fig 4.1A that complete conversion of oxygenates was achieved after varying times except for the highest poison experiment (NiMo_2000Fe), where even after 330 min, 7% of oxygenates remained in the reaction mixture. Also, note that we have only one data point for this experiment, since a poor mass balance was observed for intermediate samples. As a result, the experiment was repeated and only one sample from the reaction mixture was collected and analyzed. The deactivation effect of Fe on the catalyst is apparent by comparing the time to achieve complete oxygenate conversion with increasing poison concentration. It required 95 min to reach complete oxygenate conversion for the baseline NiMo_0 Fe experiment, while for the NiMo_500 Fe experiment it required more than three times the reaction duration. This suggests that Fe could be blocking the active metal sites. In the given experimental setup during HDO of OA on NiMo catalyst, we see from the baseline experiment that decarbonation is the preferred route while direct HDO is minor.

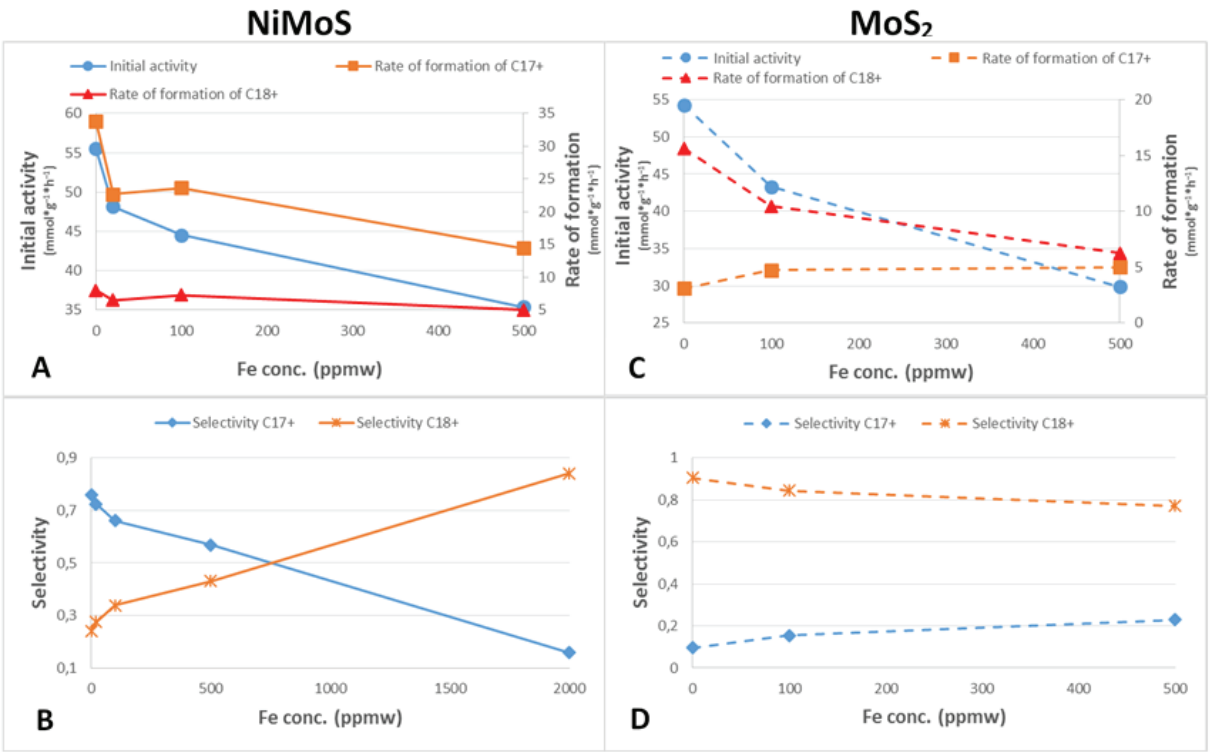

Fig 4.2 A B, C and D: Comparison of initial activity for oxygenate conversion and rate of formation for C17 & C18 and final selectivities (after 330 mins) for DCOx & HDO routes for different poison (Fe-oleate) concentrations with NiMoS (solid line) and MoS_2 (dash line).

In Fig 4.2, the initial activity of the catalyst and selectivity with the poison (Fe) concentration is compared. From Fig 4.1B, 4.1C and 4.2B, the effect of Fe on the selectivity of products is evident. With increasing Fe concentration, the selectivity for C17+ decreases while C18+ formation becomes the preferred route at the Fe concentration of 2000 ppmw. From comparing the baseline experiment with the NiMo_500 Fe experiment, it can be seen that the selectivity for the DCOx route has decreased from 0.76 to 0.57 (Fig 4.2B). Consequently, there is an increase in the selectivity for C18+ products with increased poison. We could see from the results that the effect due to deactivation of the catalyst on the DCOx route is more than compared to the direct-HDO (in Fig 4.2A). It should be mentioned that in a refinery setup, the direct-HDO product is often preferred as it retains more carbon atoms in the valued products and represents higher carbon yield [20]. Also, the consumption of hydrogen in these two routes is different. So if selectivity and activity of the catalyst is changing due to a poison, then it could have a negative impact on the product yield.

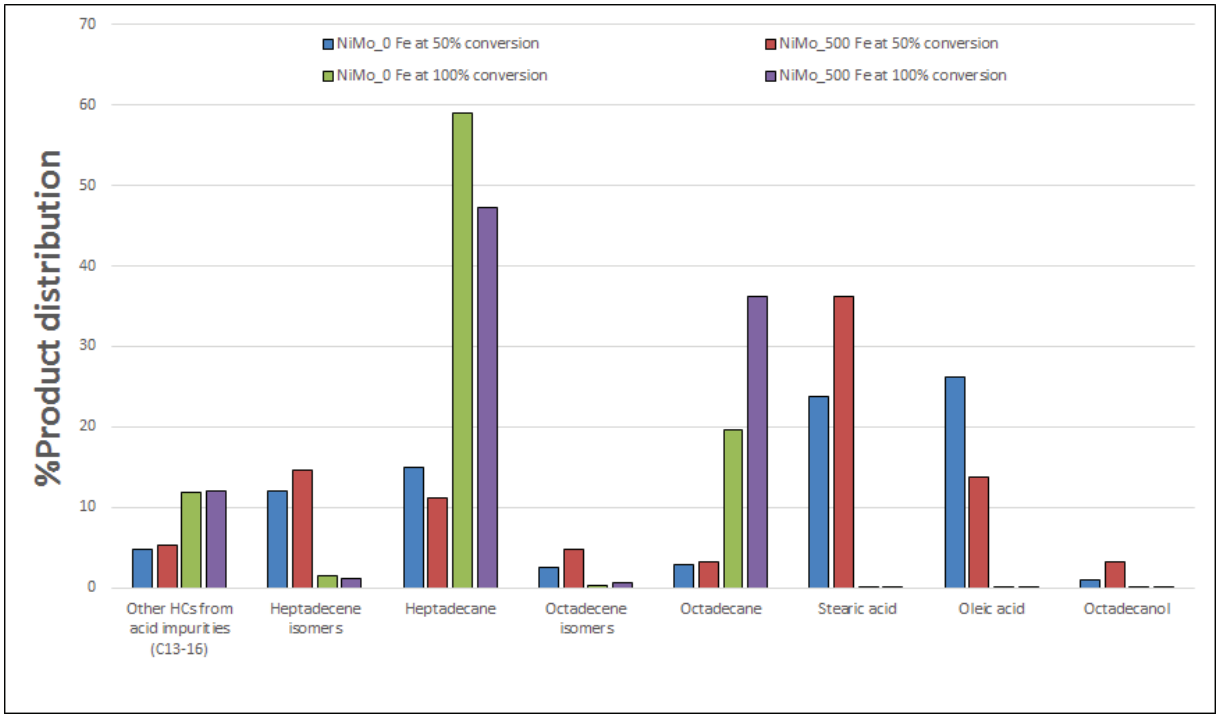

Fig 4.3 Product distributions for NiMo catalyst with no poison (NiMo_ 0 Fe) and high poison (NiMo_500 Fe) at 50 and 100% oxygenate conversion respectively. Results at 50% conversion interpolated from experiments.

The product distributions for NiMo_0 Fe and NiMo_500 Fe experiments at 50 and 100% oxygenation conversion are compared in Fig 4.3. Here, the values from the experimental data were interpolated to estimate the amounts of the respective components at 50% conversion. For both the catalyst systems, complete oxygenate conversion was achieved within 330 mins. Other acid impurities accounted for around 12% yield of products for both cases at 100% conversion. This also suggests that introduction of Fe did not enhance cracking with the NiMo catalyst at the given reaction conditions. There was an interesting observation regarding the alkene/alkane product ratio. It seems that hydrogenation capability of the active sites depleted with the addition of Fe. For both C17 and C18 products higher alkene/alkane ratios were observed even at the same conversion with increasing Fe. This is well in accordance with previous studies where it is postulated that the conversion of alkenes is delayed until most of the oxygenates are converted, since they bind very strongly to the active sites. It is evident from Fig 4.1 that all reactions are slowed down due to presence of Fe. In Fig 4.3, at 50% conversion, SA is 12% higher for the experiment with Fe (NiMo_500 Fe) when compared to the baseline experiment. Also, other intermediates like octadecanal and octadecanol were found to go via a larger maximum for the poisoned experiment.

4.1.2 HDO of OA over Mo catalysts

The unpromoted molybdenum catalyst was tested since the shift in selectivity with NiMo discussed in the above section was peculiar. Therefore HDO of OA was carried out on MoS_2 at different Fe concentrations, as shown in Table 3.1. Fig 4.4 A, B and C compare the three experiments with varying Fe concentration (0, 100 and 500 ppmw) for oxygenate conversion and for selectivity of the two main routes. The reaction chemistry was similar to the one seen with Ni

promoted catalysts with two main differences. On the MoS_2 surface, much larger amounts of octadecanol were observed during the course of the reaction. Here, direct-HDO was found to be the major route, unlike for the Ni promoted catalyst. Irrespective of the Fe concentration in the feed, it was clear that selectivity is in favor of C18+ products (Fig 4.2D and 4.4B). From Fig 4.4B, the conclusion could be drawn that MoS_2 active sites have a higher tendency for hydrogenation reactions, which results in a selectivity of more than 80% for the direct-HDO route. This characteristic of Mo based catalysts has been reported in other studies as well [49]. A similar trend of decrease in activity could be observed with the increased Fe in the feed, where a longer duration is required to reach complete conversion of oxygenates. From Fig 4.2C, it could be seen that there is a drop in the initial activity, so clearly Fe seems to be blocking the active sites on the catalyst surface. It has been reported that for such catalyst systems activity order is NiMo>Mo>Ni on alumina [30]. The same order can be observed from the experimental results in this study.

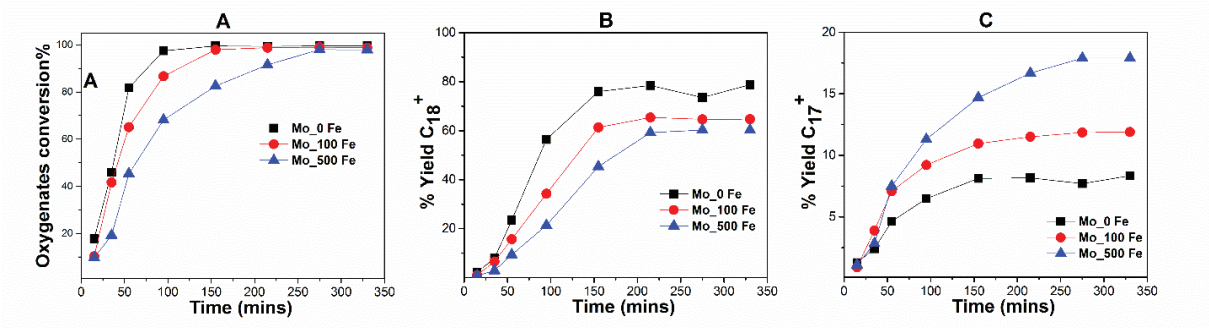

Fig 4.4 A, B & C: Selectivity of major products during HDO of Oleic acid over MoS_2/γ-Al_2O_3 with varying concentrations of poison (Fe-oleate).

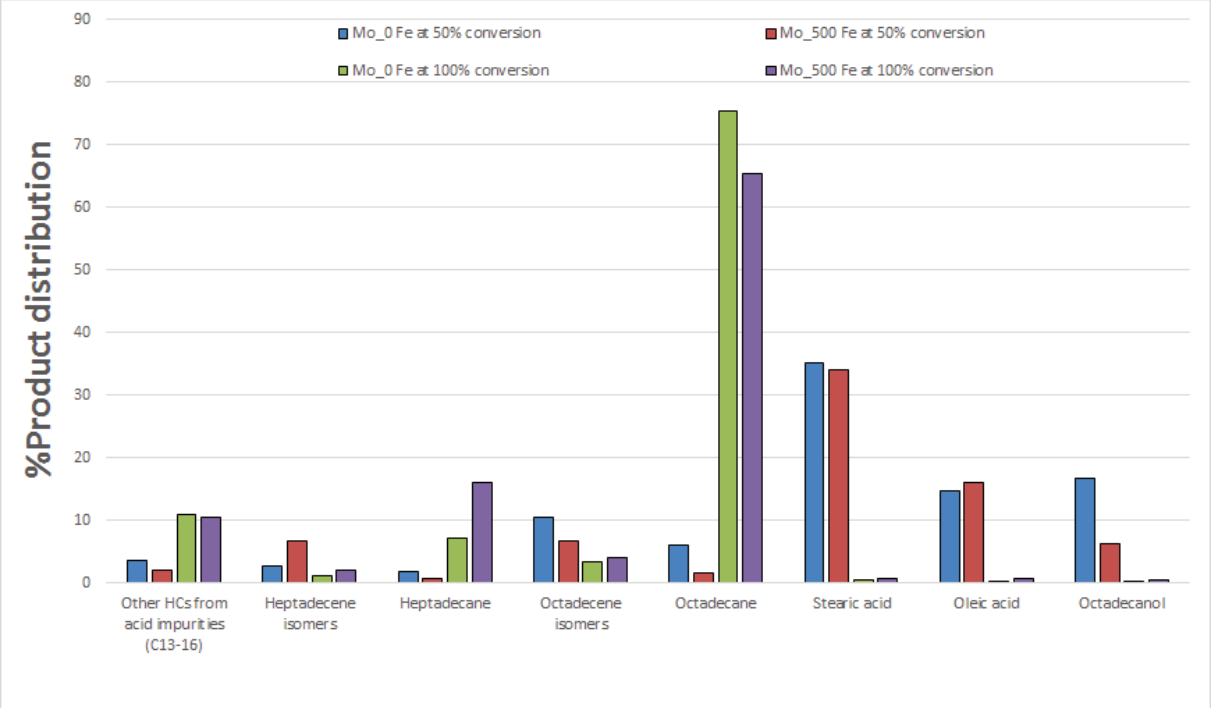

Fig 4.5 Product distributions for MoS_2 catalyst with no poison (Mo_ 0 Fe) and high poison (Mo_500 Fe) at 50 and 100% oxygenate conversion respectively. Results at 50% conversion interpolated from experiments.

By comparison of the two catalysts systems, the drop in activity for MoS_2 was larger (44%) than that of NiMoS (36%). The promotional effect of Ni on molybdenum catalysts have been explained mechanistically with the reasoning that at the Ni promoted sites, the antibonding S-metal d states are below the fermi level due to the weakening of the bond between S-S on the edge. The promoting effect of Ni is due to the weakening of the metal-sulfur bond, which results in the creation of more sulfur vacancies, hence higher activity. The selectivity trend observed in this catalyst (MoS_2) was opposite to the one seen above for NiMoS. When Fe concentration was increased from 0 to 500, a drop from 80 to 60% was recorded for yield of products via direct-HDO i.e. C18+ hydrocarbons. On the other hand, yield of heptadecane and its isomers increased from 8 to 18% during the same range of Fe concentration. Fig 4.2 presents the same results in terms of selectivity with a plunge in the C18+ products with a modest jump in the decarbonation route products. Fig 4.5, compares the product distribution for the unpromoted molybdenum catalyst for 0 and 500 ppm Fe at 50 and 100% oxygenate conversion. The impact of Fe on the hydrogenation activity of the catalysts is evident from the increased alkene/alkane ratio. At 50% conversion, the alkene to alkane ratio for 0 and 500 ppm experiments was 1.5 and 10.4 respectively for the decarbonation route products while that for C18 products it was 1.8 and 4.4 for Mo_0 Fe and Mo_500 Fe experiments respectively. Higher amounts of oxygenates present were observed in the reaction mixture at the same time point for MoS_2, compared to that of the NiMoS catalyst. This implies that the impact of Fe poison has a larger influence on the Ni promoted catalyst, though in absolute terms, the unpromoted catalyst lost two-third of its activity.

4.1.3 Catalyst deactivation and characterization

To further comprehend the change in activity and selectivity of these two catalyst systems, extensive characterization of the samples was carried out. Table 4.1 displays the textural and compositional properties of both fresh and spent catalyst samples. In a patent study, it has been suggested that a renewable feed containing Fe species could lead to a rapid increase in the pressure drop due to reactor plugging [50]. The surface area and pore volume decrease due to coke formation and irreversible adsorption of certain species during the reaction. As evident from Table 4.1, both the surface area and pore volume dropped by 23 and 16% respectively for the NiMo_Fe catalyst compared to the fresh sample, while much less of a drop was observed for the baseline experiment (6 and 7%). This decrease is substantial, considering it was only a short HDO experiment of 330 min. Thereafter, elemental analysis was carried out to estimate the carbon content of the spent catalysts. Coking was quite low (0.76 to 1.3 wt%) for all the catalyst samples, except for NiMo_2000 Fe where it was 3.5 wt%. However, that could be explained by the fact that the conversion of oxygenates was not completed by the end of the experiment. Since these molybdenum based catalysts have an active phase in sulfided form, we looked into the sulfur content of the recovered catalyst from different HDO experiments. On the basis of calculations, the sulfur content of the MoS_2 and NiMoS catalysts would need to be 6.1 and 7.2 wt% respectively to achieve complete sulfidation of the active phase. However, from Table 4.1, it could be seen that the sulfur content was in the range of 6-11 wt%, which suggest that there was not much loss in the sulfur from the active phase. Slightly higher amounts of sulfur present could be attributed either to loosely bound sulfur species on for example the support or some uptake by Fe to form FeS-like compounds.

Table 4.1 Textural properties and elemental content of sulfur and carbon on fresh and recovered catalyst samples.

Sample	BET surface area [m^2g^{-1}]	Pore Volume [cm^3g^{-1}]	Average Pore Size [Å]	S [wt%]	C [wt%]
γ-Al_2O_3	199	0.48	97.6	<0.1	0.1
NiMo (fresh)	141.5	0.31	87.6	<0.1	0.04
Mo (fresh)	154.5	0.33	88.2	<0.1	0.04
NiMo_0 Fe [a]	131.3	0.29	86.6	8.3	0.9
NiMo_20 Fe[a]	-	-	-	6.9	0.76
NiMo_100 Fe[a]	-	-	-	7.7	1.17
NiMo_500 Fe[a]	118.9	0.24	80.8	7.6	0.72
NiMo_2000 Fe[a]	-	-	-	10.9	3.52
Mo_0 Fe[a]	144.7	0.31	87.1	6.0	1.1
Mo_100 Fe[a]	-	-	-	5.8	1.3
Mo_500 Fe[a]	132.3	0.26	81.7	5.8	1.6

[a] after 330 min of HDO reaction

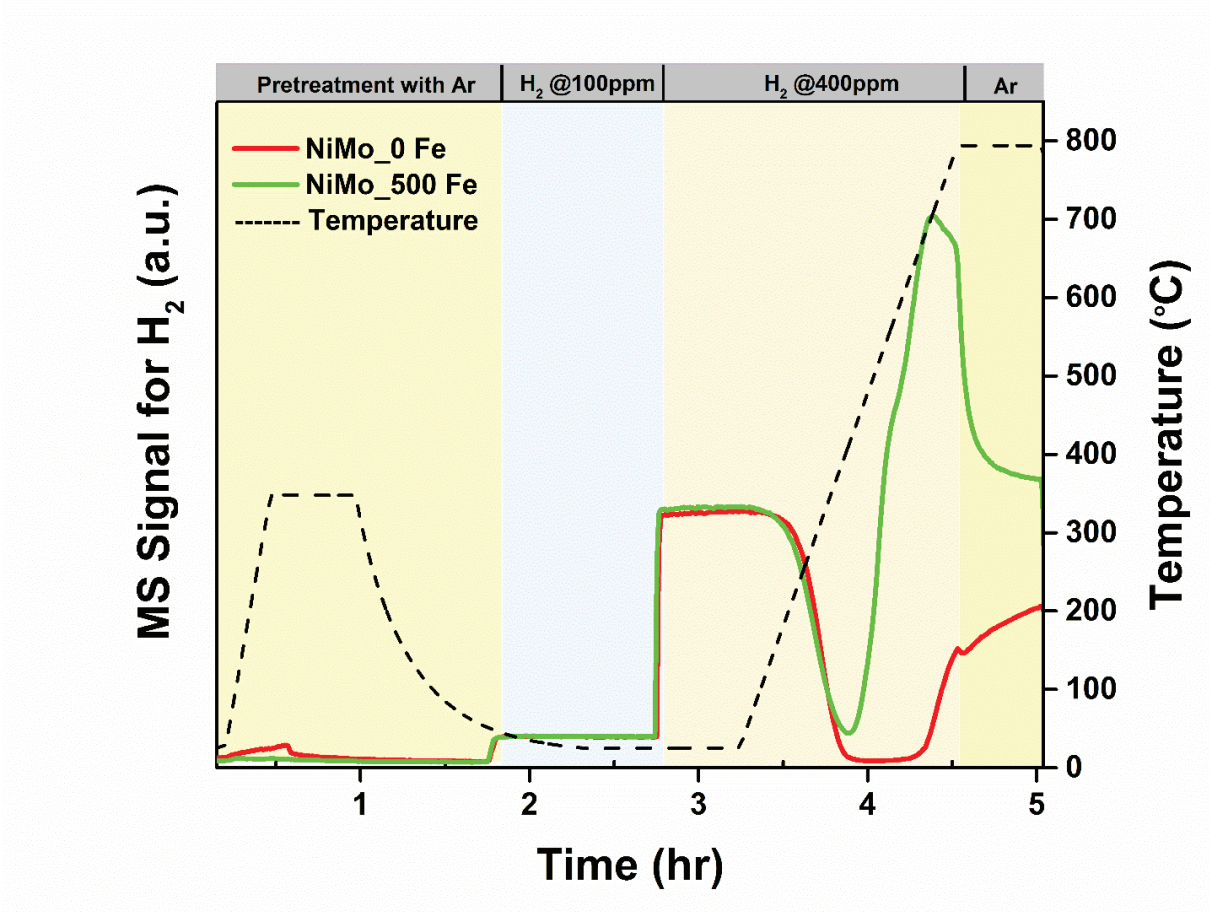

Fig 4.6 Pretreatment and H_2 temperature programmed reaction on recovered catalyst samples NiMo_0 Fe and NiMo_500 Fe.

Results of temperature programmed reaction with hydrogen are depicted in Fig 4.6. In this analysis, spent catalyst from NiMo_0 Fe and NiMo_500 Fe experiments were used. There was a negligible hydrogen adsorption at ambient temperature. It started only at a higher temperature

of about 200 ˚C. After further increasing the temperature, the NiMo_500 Fe sample desorbed approximately the same amount of hydrogen starting at around 400 ˚C. Hydrogen was more reactive with the sample from the baseline (NiMo_0 Fe) experiment, as many sulfur containing species like H_2S were observed by the mass spectrometer. This suggests that the labile sulfur was present much more in the absence of Fe poison. As explained in Section 2.2 above, for TMS catalyst systems, the creation of sulfur vacancies is the first step of their catalytic cycle. Sulfur vacancies have a direct correlation to the activity of such catalyst systems. Fe salts are known to be moderately oxidative in nature, so it could be postulated that the active sulfide phase has been oxidized and rendered inert for reaction with hydrogen even at higher temperatures by the Fe poison.

Table 4.2 ICP analysis results of fresh and recovered catalysts and liquid phase following reaction.

	Atomic ratio		**Liquid Phase**
	Ni/Ni+Mo	**Fe/Fe+Ni+Mo**	**Fe (mg/kg)**
NiMo (fresh)	0.36	<0.01	-
Mo (fresh)	-	<0.01	-
NiMo_0 Fe	0.37	0.01	<0.2
NiMo_20 Fe	0.36	0.05	<0.2
NiMo_100 Fe	0.36	0.07	<0.2
NiMo_500 Fe	0.37	0.28	<0.2
NiMo_2000 Fe	0.37	0.57	<0.2
Mo_0 Fe	-	0.01	<0.2
Mo_100 Fe	-	0.09	<0.2

In Table 4.2, the results from the ICP analysis of fresh and spent catalyst samples are shown. The liquid phase after the HDO experiment was also analyzed. Fresh catalyst samples – MoS_2 had 9.2 wt% of Mo and NiMoS had 3.3 wt% of Ni and 9.3 wt% of Mo respectively. Atomic ratio for Ni/Ni+Mo was constant for fresh and spent catalyst, which indicates that there was no leaching of metal from the catalyst, and thus no reactions in the homogeneous regime. In Table 4.2 it could also be observed that no Fe was detected in the reaction mixture (liquid phase), which confirms that all Fe uptake was by the catalyst. In case of the Alumina_500 Fe experiment, most of the Fe remained in the liquid phase. These results allow us to propose that the Fe is being deposited on or near the metal centers of these catalyst. It could be postulated that the Fe deposition is related to the catalytic activity. When Fe oleate complexes are adsorbed at the catalytic sites, the oleate ligand is deoxygenated while Fe is deposited at or near the active sites. This is in accordance to that observed for hydrodemetallisation (HDM) during hydrotreating of fossil feeds, where the metals present in petroporphyrins like V and Ni are deposited at the active catalytic sites [51].

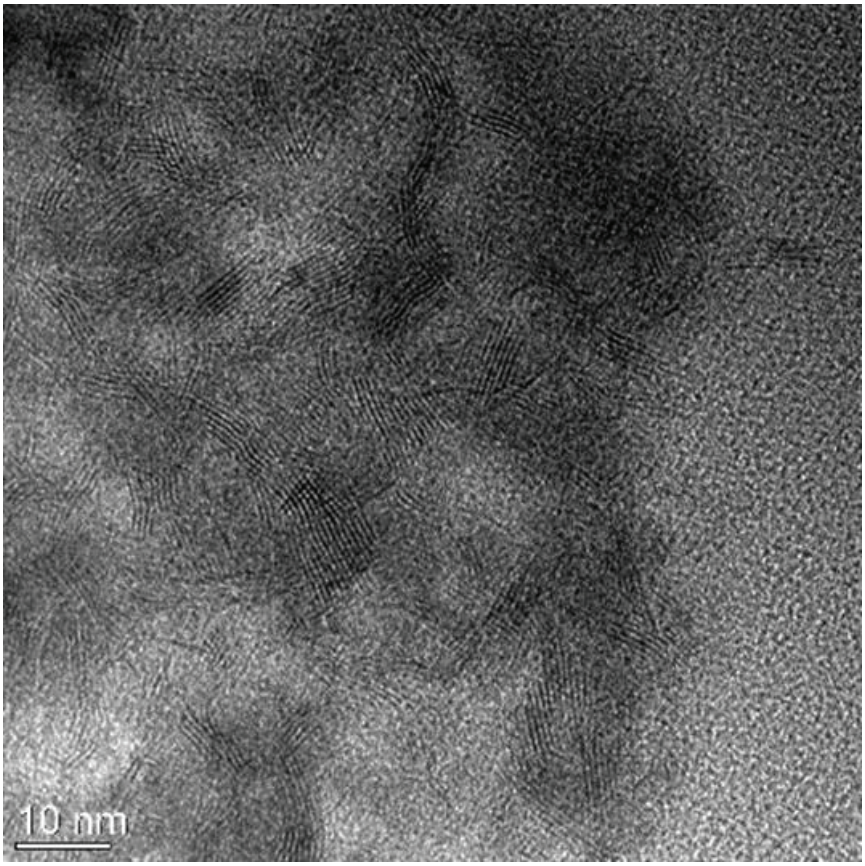

Fig 4.7 HR-TEM image of catalyst recovered after 330 mins of HDO (NiMo_500 Fe) experiment.

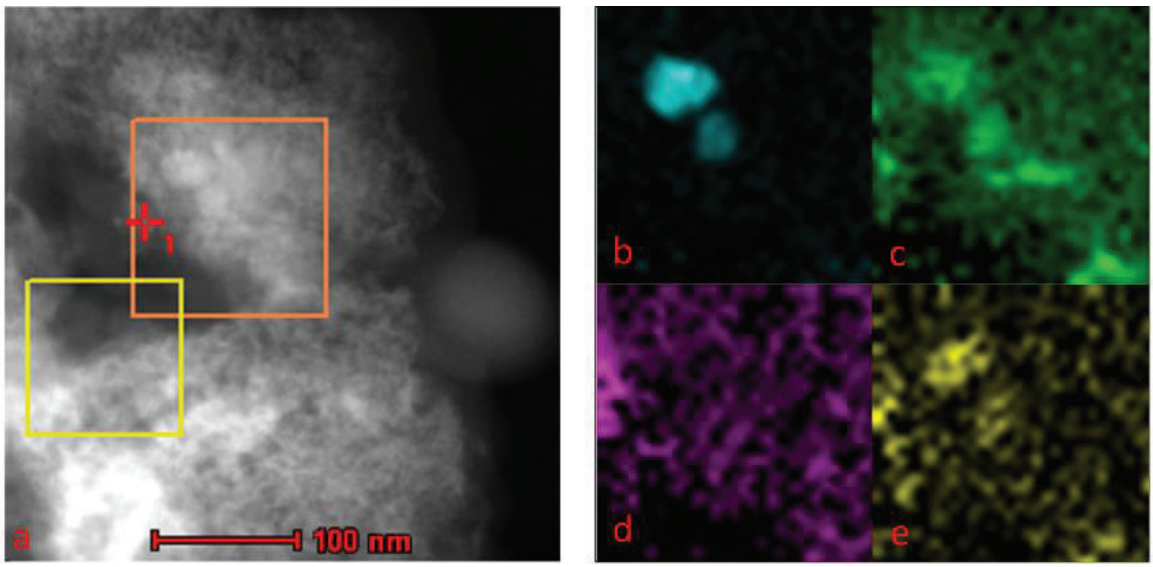

Fig 4.8 (a) HAADF-STEM image NiMoS recovered after 330 mins of HDO (NiMo_500Fe) experiment and corresponding EDX mapping according to elements: (b) nickel (c) iron (d) molybdenum and (e) sulfur.

TEM was employed to analyze the morphological structure of the MoS_2 slabs and dispersion of the active metal centers. Moreover, Fe poisoned catalyst samples were analyzed with TEM-EDX mapping to determine the distribution of Fe relative to Ni and Mo. Fig 4.7 shows an HR-TEM image of the catalyst recovered after 330 mins of HDO (NiMo_500 Fe experiment). Fig 4.8 depicts the

EDX mapping of the same sample for elements: nickel, iron, molybdenum and sulfur. The edge planes of the MoS_2 slabs are clearly seen which are oriented in line with or at a small angle from the electron beam in Fig 4.7. Moreover, the MoS_2 slabs in NiMo_500 Fe samples seem to be blurry and less distinct. This could be due to oxidation by Fe salts. This may suggest that Fe poisons promote oxidation and prevent the resulfiding of the MoS_2 phase. This theory is in concurrence with the results shown for temperature programmed reaction with H_2 in Fig 4.6, where the spent catalyst in absence of Fe was observed to form H2S to a much greater degree than the catalyst poisoned by Fe. In the EDX elemental maps of Fig 4.8, the section inside the orange square was scanned for a long duration to determine the distribution of Fe, Ni, Mo and S. It is interesting to find that the distribution of Fe was closely overlaying on the signals from Ni, although Fe is present on other areas as well. This suggest that Ni promoted sites (NiMoS) would have been affected more compared to the base catalyst by Fe poisoning during HDO of Fe oleate. There are Ni rich sites on NiMoS catalyst as well the sites where Ni is absent. Ni-rich sites are selective for decarbonation while sites where Ni is scare would act like the MoS_2 phase which favors the direct-HDO route. Since, Ni-rich sites would be affected more due to Fe poisoning, then decarbonation activity selectively decreases and effectively direct-HDO is favored. We could also extend the possibility of formation of FeMo phase with the fact that Fe is a weaker promotor, compared to Ni, to enhance DCOx route. It has been shown in previous studies that Fe is a weaker promotor for HDS catalysts [52]. Thus, it is probable that Fe could have a weak promotional effect for HDO reactions, if the deposited Fe can partially form a FeMo phase.

4.2 Influence of Bio-Oil Phospholipid on the Hydrodeoxygenation Activity of NiMoS/Al_2O_3 Catalyst

4.2.1 Effect of phosphatidylcholine as P contaminant

Fig 4.9 shows the conversion of oxygenates (sum of oleic acid and stearic acid) and yields of C17 and C18 hydrocarbon products in presence of varying concentration of the phosphorus containing complex. Four different concentrations of poison (phosphatidylcholine) were tested, in addition to a baseline experiment with no poison (see Table 4.3). The experiment with the lowest concentration (0.2%) of phosphatidylcholine in the reaction mixture has not been shown as it had a negligible effect on the catalytic activity of the HDO reactions. It can be observed in Fig 4.9 (a) that the rate of conversion of fatty acids slowed down with an increase of poison in the reaction mixture. The conversion of oxygenates for the highest poison experiment i.e. PC 1.3 wt% was 47% while for the experiment with no poison, it was around 74% after 2 hours. Comparing the ratios of oleic acid to stearic acid and alkenes to alkanes (for both C17 and C18), it suggests that the presence of phosphorus also strongly decreases the hydrogenation rate of double bonds. Interestingly, the effect of phosphatidylcholine on the two reaction routes yielding C17 and C18 hydrocarbons were different. It can be seen in Fig 4.9 (b) & (c), that the yield of C17 and C18 products were 59 mol% and 19 mol% for the baseline experiment while for the highest poison experiment, they were 39 mol% for C17 and 19 mol% C18 at the end of the experiment. Table 4.4 lists the initial catalyst activity and rate of formation of C17 and C18 hydrocarbons for the related experiments. Here, it can be seen again that the decarboxylation route was affected more than the direct-HDO route. In baseline and PC 1.3 wt% experiments, at a comparable oxygenate conversion i.e. 46 and 47% respectively, the selectivity for C17 products dropped modestly by 11%

from the no poison to the highest poison experiment. From Fig 4.9 (b) and Table 4.4, it is apparent that the drop in yield of C17 products is co-related to the increasing amount of phosphorus complex introduced.

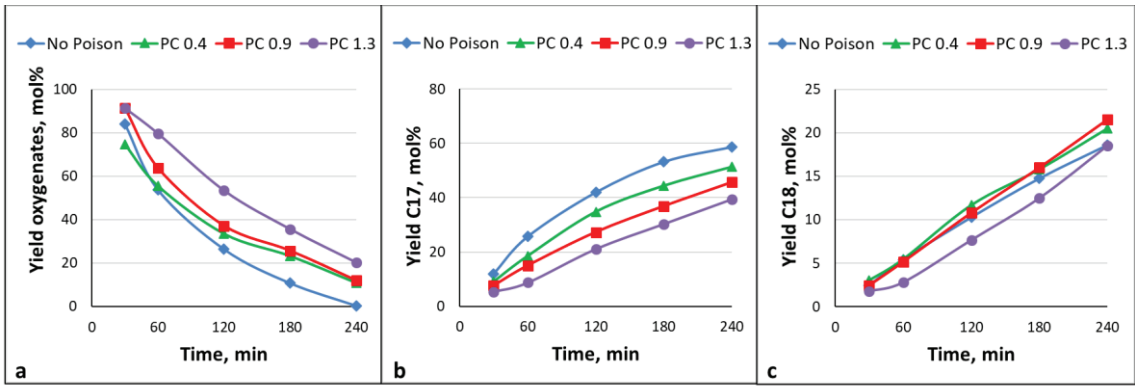

Fig 4.9 Oxygenates yield (a), yield of C17 (b) and C18 (c) hydrocarbons during HDO of oleic acid over NiMo catalysts with varying phosphatidylcholine concentration; Experimental conditions - Catalyst 0.5 g, Stearic acid (SA) as feed 10 wt%, Dodecane as solvent with a total volume of 150 ml, Pressure 54 bar (H_2) and Temperature 320 °C.

Table 4.3 Concentration of poison element in feed per mass of catalyst and abbreviations for the batch reactor experiments.

Name of the Experiment	Poison Compound	Poison in feed per mass of catalyst		
		PC	Choline	Water
No Poison	-	-	-	-
PC 0.2	Phosphatidylcholine (PC)	0.2%	-	-
PC 0.4	Phosphatidylcholine (PC)	0.4%	-	-
PC 0.9	Phosphatidylcholine (PC)	0.9%	-	-
PC 1.3	Phosphatidylcholine (PC)	1.3%	-	-
Choline	Choline hydroxide	-	1.3%	1.3%
H_2O	Water	-	-	1.3%

Table 4.4 Initial rates of oxygenates conversion and alkane formation measured at 1 h.

Experiment/ Initial rates	$r_{oxygenates}$ (mmol/g/h)	r_{C17} (mmol/g/h)	r_{C18} (mmol/g/h)
NiMo_0 PC	59.1	65.8	13.8
NiMo_0.4 PC	46.3	47.3	13.9
NiMo_0.9 PC	32.2	38.2	13.2
NiMo_1.3 PC	27.6	23.8	7.6
NiMo_Choline	45.9	39.5	14.9

This change in the production of the two different hydrocarbons i.e. heptadecane and octadecane at the end of the experiment with increasing amount of poison is highlighted in Fig 4.10. As it can be seen the decarbonation route has affected more compared to the direct-HDO route with the introduction of phosphatidylcholine. The yield of C17 hydrocarbons dropped from 58 to 39% from the no poison to PC 1.3 wt% experiment while the production of C18 products was unaffected by the amount of poison added. Also, it was observed that the share of unsaturated products (C17 & C18 combined) in the reaction mixture at the end of experiment due to the presence of PC

complex increased. It is evident that the phosphorus poison affected the hydrogenation activity of the catalyst such that the amount of unsaturated products increased almost three-folds for the highest poison experiment (PC 1.3 wt%) compared to the baseline with no poison.

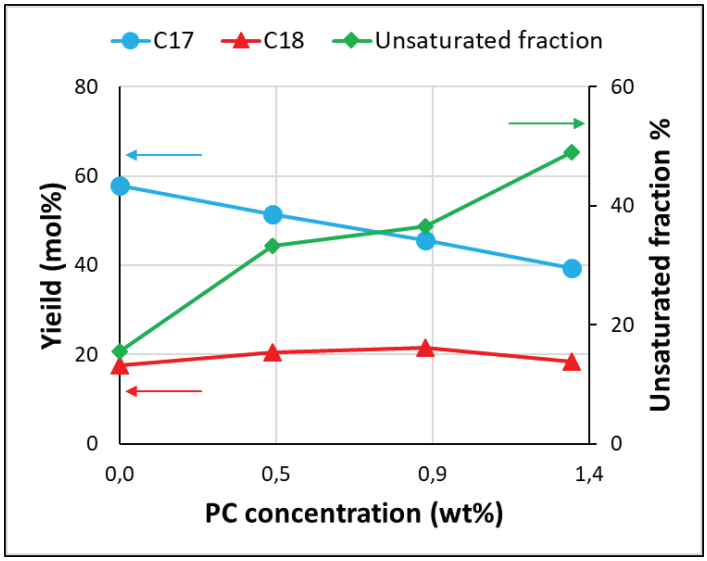

Fig 4.10 Comparison of C17 and C18 selectivity and Unsaturated fraction with varying concentrations of PC complex.

4.2.2 Effect of choline on catalyst deactivation

As it can be seen in Fig 3.1, the phosphatidylcholine molecule has three components - a non-polar hydrocarbon tail, a hydrophilic phosphate group, and an organic choline group containing nitrogen. It can decompose at given reaction conditions via acid hydrolysis to yield smaller molecules like fatty acids, glycerol, phosphoric acid and choline [66, 67]. The fatty acid formed upon decomposition of the phospholipid molecule corresponds to 6.7 wt% of the initial oleic acid (OA) amount in the reaction mixture for the highest poison concentration experiment. This has been taken into account during the material balance calculations. Other components like glycerol are expected to be converted to propane under the H_2-rich environment of the experimental conditions used. It has been suggested that the decarboxylation route can be severely affected with the introduction of amines like di-aminopropane [46]. There are some similarities between choline and amine compounds as both have a strong Lewis base character and can negate the acidity of the catalyst and/or neutralize the effect of H_2S. Also, choline could degrade into trimethylamine at high temperature and pressure conditions. Thus, to isolate and distinguish the poisoning effects of the choline molecule with rest of the phosphorus containing complex, an experiment was performed with an equivalent amount of choline present as that for the experiment with 1.3% PC in the feed. Fig 4.11, depicts the conversion of fatty acids and hydrocarbons products formed over time comparing the following experiments - baseline, PC 1.3%, and choline in the reaction mixture. It can be seen that the conversion of oxygenates is slower in presence of phosphatidylcholine than just choline. After 240 mins, the amount of oxygenates remaining in the reaction mixture were – 0% (for baseline), 20% (for PC 1.3%) and 8% (Choline). From Fig 4.11 (b) & (c), it can be observed that the impact on the rate of production of C17 and C18 products due to these two potential poisons was different as well. However, the selectivity for C17 hydrocarbons at similar oxygenate conversion was approximately 0.7 for both the poisons. Gas samples collected at the end of the experiments with phosphatidylcholine and choline did not show any amounts of ammonia. Thus, the possibility that ammonia had an impact

on the catalyst deactivation at these reaction conditions can be ruled out. However, the choline itself did seem to cause deactivation, although we don't know if it remained in its original form or was converted into something else during the experiments.

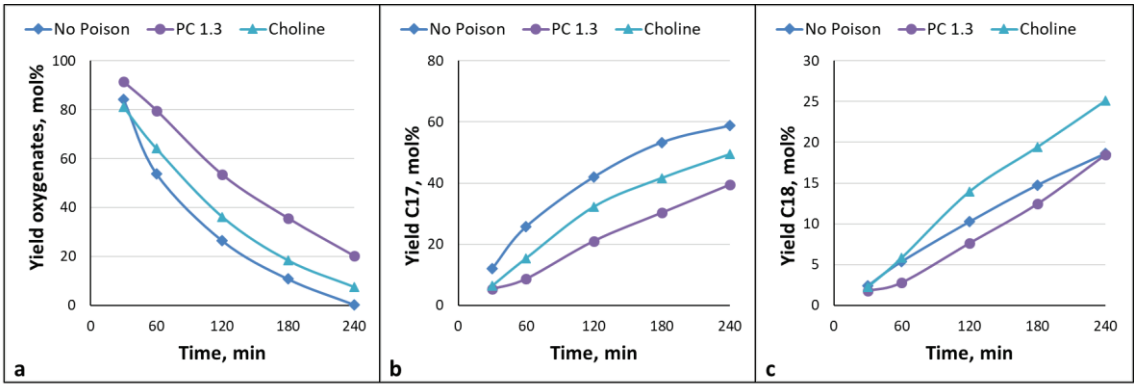

Fig 4.11 Oxygenates yield (a), yield of C17 (b) and C18 (c) hydrocarbons during HDO of oleic acid over NiMo catalysts with various poisons or no poison; Experimental conditions - Catalyst 0.5 g, Stearic acid (SA) as feed 10 wt%, Dodecane as solvent with a total volume of 150 ml, Pressure 54 bar (H_2) and Temperature 320 °C.

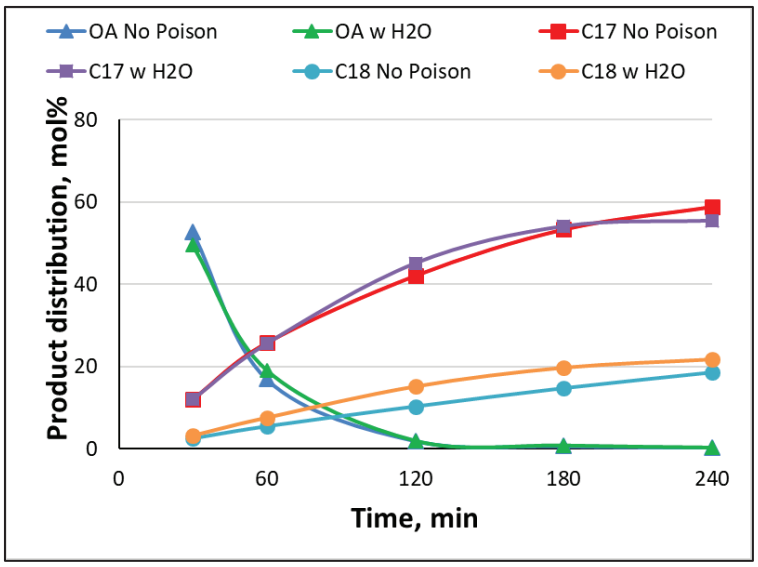

Fig 4.12 Product distribution during HDO of oleic acid over NiMo catalysts with no poison and water (24ppmw); Experimental conditions - Catalyst 0.5 g, Stearic acid (SA) as feed 10 wt%, Dodecane as solvent with a total volume of 150 ml, Pressure 54 bar (H_2) and Temperature 320 °C.

Since the choline containing solution contained water, an additional experiment was carried out with an equivalent amount of water to determine whether the water also had some influence on deactivation. Fig 4.12, presents the concentration of oxygenates and yields of C17 and C18 over time compared to the baseline experiment. Also, it has been shown in other studies that the presence of water can affect the catalytic activity during hydrodeoxygenation reactions depending on the amount of water present. Coumans et. al. concluded that water had a slightly negative effect on HDO activity for concentrations lower than 5000 ppm while it was unchanged at concentrations exceeding 5000 ppm [49]. Accordingly, at these low concentrations of water tested in our study, there was no change in the catalyst activity and selectivity. The conversion and yield plots of the baseline experiment and the experiment with water (24 ppmw) overlapped

at all sampling points. Thus, it can be concluded that the deactivation of catalyst caused by the phosphorus part is more severe than that from the choline moiety alone.

4.2.3 Catalyst characterization

Textural properties of the catalyst

Nitrogen physisorption was done to determine the change in catalyst surface area, pore volume and pore size due to the influence of the PC complex present in the feed. The results for fresh catalyst, spent catalysts from no poison and PC 0.4 wt% experiments are listed in Table 4.5. Surface area, pore volume and pore size dropped by 27, 33 and 11% respectively for the NiMo_0.4 PC sample compared to the fresh catalyst. It is known that coking initiates due to the chemisorbed species from undesirable side reactions. It has been shown that the coke formation affects the textural properties of the catalysts. So, the elemental analysis was carried out to quantify carbon deposition on catalyst samples recovered after the experiments. Table 4.6, presents the results from elemental analysis. The amount of carbon increased with the increasing dosage of the poison complex. However, it should be pointed that some of the carbon can be attributed to unconverted oxygenates at the end of the experiment. A loss of sulfur indicates that the catalyst has oxidized during HDO reactions which can contribute to the deactivation of catalysts. As it is seen in Table 4.6, the amount of sulfur in all spent catalysts was about 7.5% which rules out the possibility of a loss in activity due to depletion of the active sulfided phase of these catalysts. A small amount of nitrogen (approx. 0.4 wt%) validates the presence of nitrogen which is likely due to the choline moiety of the PC complex.

Table 4.5 Textural properties of fresh and spent catalyst samples.

Sample/ Analysis	BET surface area [m^2g^{-1}]	Pore Volume [cm^3g^{-1}]	Avg Pore Size [Å]
Synthesized	143	0.33	62
NiMo_0 PC	126	0.27	62
NiMo_0.4 PC	105	0.22	55

Table 4.6 Elemental analysis of listed samples.

Sample/ Analysis	Carbon [wt%]	Sulfur [wt%]	Hydrogen [wt%]	Nitrogen [wt%]
Sulfided	0.4	1.3	9.22	<0.05
NiMo_0 PC	2.96	1.57	7.3	<0.05
NiMo_0.4 PC	5.34	1.65	7.39	0.36
NiMo_0.9 PC	5.9	1.3	7.4	0.3
NiMo_1.3 PC	7.74	1.73	7.47	0.37

ICP analysis of recovered catalyst and liquid samples

The ICP results depicting the concentrations of active metals, i.e. Ni and Mo, and poison element, i.e. P, of various samples is listed in Table 4.7. As it can be seen the atomic ratio of Ni/(Ni+Mo) was almost the same for fresh and spent catalysts, so it could be concluded that there was no leaching of active metals during the experiments. Comparing the amount of P added with respect to the catalyst at the beginning (theoretical) and the amount of P via ICP on recovered catalysts at the end of the experiment, indicates that there was a smaller uptake of P by the catalyst. Also, the reaction mixture at the end of the experiment contained only a small amount of phosphorus. It was surprising to note that the amount of P on recovered catalysts from two experiments – PC 0.4 wt% and PC 0.9 wt% was not proportional to the amount of poison added at the beginning. This could be explained due to the fact that these catalysts were washed off with warm ethanol when recovered from the reaction mixture. This was done to remove the unconverted oxygenates from the catalyst surface, but it seems to have also washed away the loosely bound phosphorus species as well.

Table 4.7 ICP-SFMS data for spent catalyst and liquid phase.

Catalyst	P added in liquid, ppm	Theoretical maximum P in catalyst, wt.%	Actual P in Catalyst (ICP), wt.%	Atomic ratio of Ni/(Ni+Mo)	P remaining in liquid phase (ICP) ppm
As Synthesized	-	-	-	0.37	-
NiMo_0.4 PC	179	4.09	1.98	0.39	8.37
NiMo_1.3 PC	532	12.16	1.27	0.41	11.1

XPS and TEM analysis

XPS analysis with P2p core level spectra for the poisoned spent catalyst is presented in Fig 4.13. P2p signals from all three samples with different poison amounts (0.4, 0.9 and 1.3 wt%) exhibit that phosphorus is present in its +5 oxidation state. The peak at 133.8 ± 0.2 eV suggests the formation of metal-phosphate like complexes, which could impact the catalyst activity. Also, a broadening of peak corresponding to phosphate species is observed with the increasing amount of poison employed in the experiments. Phosphate complexes with alumina support can result in a lowering of surface area and other textural changes like pore plugging and blocking of active phase, which would lead to a drop in catalyst activity [68]. This has been validated by BET results as well (see Table 4.5). Also, the possibility of phosphides formation was ruled out as there was no peak below the binding energy of the 130 eV region.

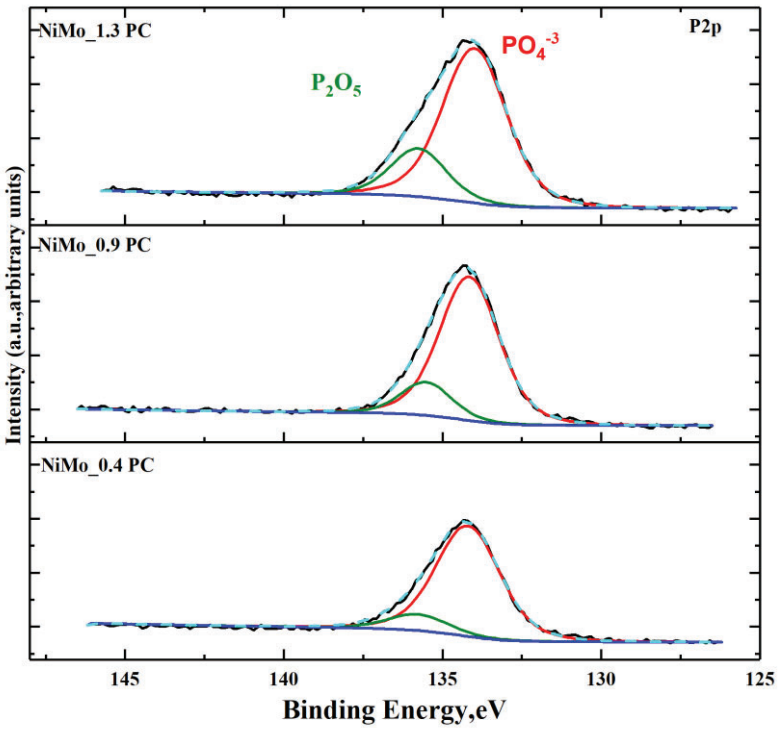

Fig 4.13 P2p core level spectra for the recovered catalysts exposed to PC.

Additionally, TEM analysis was carried out on the spent catalyst samples to examine the active phase dispersion and morphology. Bright field (BF-TEM) micrograph and EDX analysis on the NiMo 1.3 PC sample can be seen in Fig 4.14. This micrograph exhibits the typical lamellar structure of the Ni promoted molybdenum sulfide phase [15, 25]. There was an increase in stacking degree of the MoS_2 phase with the introduction of the P complex. The stacking degree for the spent catalysts from the no poison and 1.4 wt% PC experiments were 2.3±1 and 4.4±1.7 respectively. Similarly, there was a slight increase in the average slab length from 3.8±1.7 (NiMo_0 PC) to 5.3±3.2 (NiMo_1.4 PC). It has been proposed that the higher stacking degree leads to higher accessibility of the inactive basal planes of MoS_2 by edge atoms i.e. nickel. The observed decrease in stacking degree suggests a drop in the dispersion of the active MoS_2 phases on the alumina was caused by exposure to phosphatidylcholine [69]. This phenomenon results in a lower coordination between the Ni promoter and MoS_2 to maintain the active NiMoS phase in presence of the phosphorus complex. This explains the drop in catalyst activity and change in selectivity with the introduction of PC compound to a certain extent.

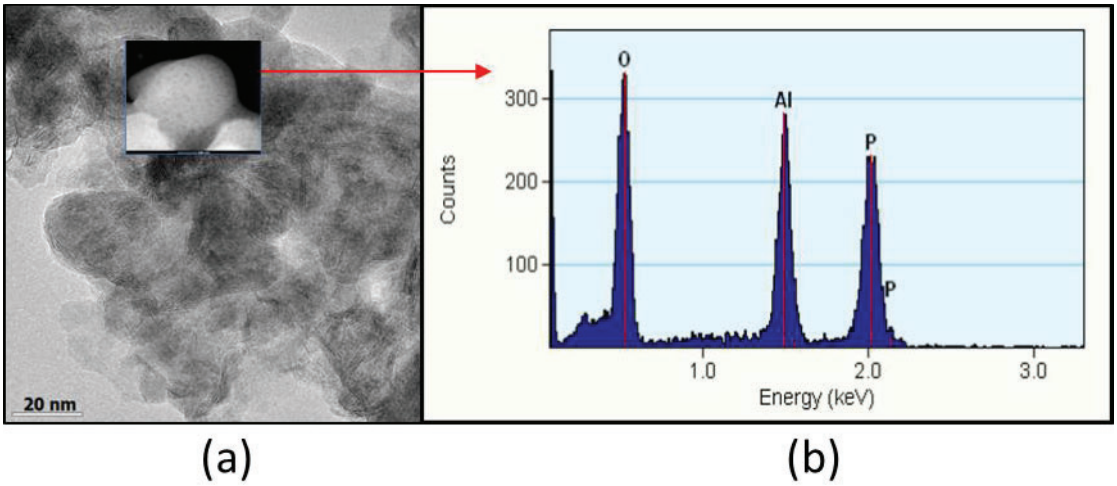

Fig 4.14 TEM analysis on the spent catalyst representing (**a**) BF-TEM micrograph, inset in (**a**) shows a characteristic area of the support (and **b**) energy dispersive X-ray (EDX) analysis on the characteristic area in (**a**).

In Fig 4.14, a particle (region) with only alumina can be seen, which also has a signal corresponding to P (see Fig 4.14 (b)). It has been reported that γ-alumina can interact with phosphoric acid via hydroxyl groups present on surface to yield phosphates. Also, it has been found that the alumina has a strong affinity towards polar phosphate groups. Thus, it is highly likely that the decomposition of PC can give intermediates which can react with hydroxyl groups of the alumina support to form aluminum phosphates ($AlPO_4$). This has been corroborated by the XPS and TEM-EDX results. Also, STEM-EDX analysis of the selected area was done to observe the distribution of poison with respect to the active metals and support. EDX mapping of poisoned catalysts is shown in Fig 4.15. It seems that the phosphorus is well distributed all over the support (alumina) particle. This suggest that phosphorus is strongly attached to the support like as a result of complex formation with alumina.

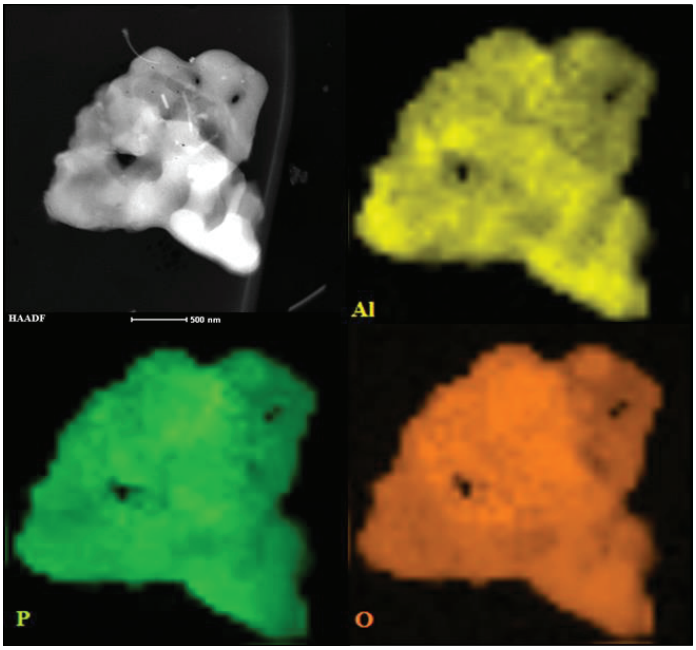

Fig 4.15 HAADF-STEM imaging and EDX mapping on a single particle showing Al, O, and P elemental distribution.

Temperature programmed oxidation and elemental analysis

Coking on catalyst can block the active metal sites and decrease the pore volume leading to severe deactivation. It has been shown in a previous study that the carbonaceous species can block the active sites of MoS_2 i.e. the edges and corners to deteriorate the catalytic activity [70]. Fig 4.16 presents the profiles of carbon oxides (sum of CO + CO_2) produced when the recovered samples that underwent temperature programmed oxidation (TPO). Also, the profile of water (H_2O) produced has been shown for one experiment (NiMo_0.9PC) for comparison. Fig 4.16a is divided into two regions A and B. In the first region (200-300 °C) water was formed at relatively higher concentrations than in the second region (300-600 °C). For all the analyzed samples, a similar trend for H_2O was seen while for carbon there were two distinct regions. Region A (on left) corresponds to the soft coke fraction which mainly consists of residual adsorbed oxygenates with lower C/H mass ratio. The soft coke tends to oxidize in a lower temperature range. While the fraction of coke in region B is of a refractory nature. This refractory coke is complex in nature with high C/H mass ratio. It binds strongly to the catalyst/support surface and requires higher temperature for combustion [71]. Fig 4.16b presents the total carbon content and C/H mass ratio in two regions on recovered samples with varying phosphorus poisoning levels. The total carbon content estimated by TPO increases with the amount of poison added. Also, it could be seen that the C/H ratio is much lower and independent of poison concentration in the 200-300 °C region, for reactant, intermediates and products, the C/H mass ratio is ca. 6. On the other hand, the C/H mass ratio corresponding to refractory coke is much higher which is reflected with the addition of more poison in the reaction mixture. Though, a certain amount of coke corresponds to the unconverted oxygenates but at higher poison loading the complex coke is attributed to the presence of phosphorus complex. Thus, it can be concluded that according to these results the phospholipid complex promotes the formation of greater quantities of refractory coke which should contribute to deactivation.

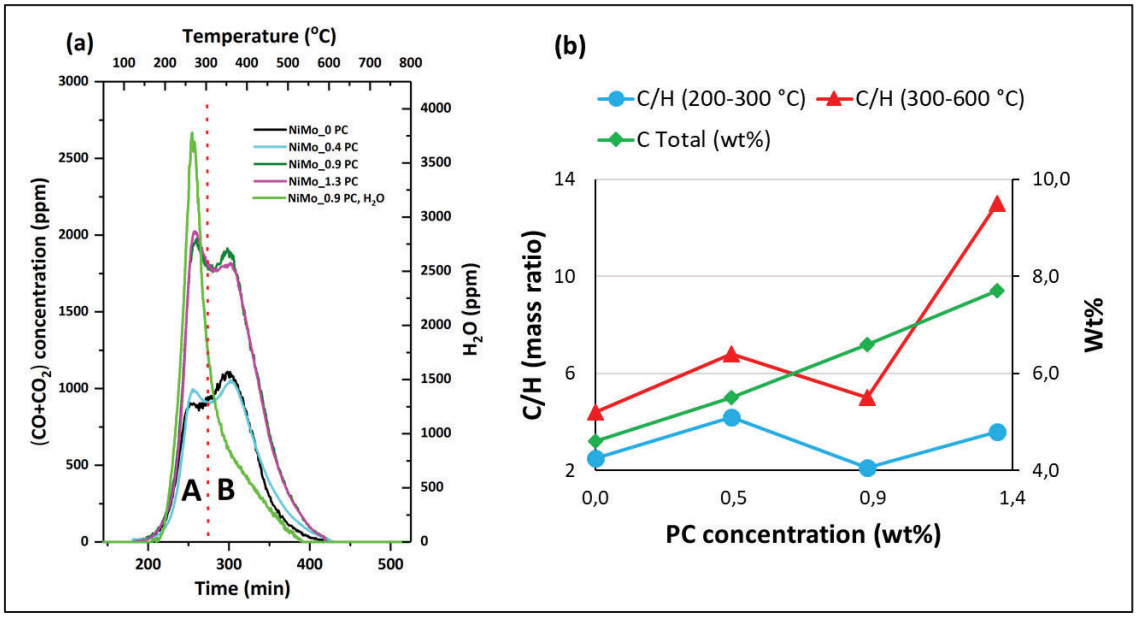

Fig 4.16 (a) CO, CO_2, and H_2O profile during TPO of the recovered catalyst; (b) measurement of carbon (C) and hydrogen (H) content (wt.%) of the recovered catalysts from TPO.

4.3 The role of catalyst poisons during hydrodeoxygenation of renewable oils

4.3.1 Catalyst characterization of catalysts used in refinery

The results from elemental analysis of catalysts used in refinery ***Fresh[R], Spent[R], Calcined[R] and Washed[R]*** are listed in Table 4.8. The carbon content of the sample recovered from refinery reactor was 1.1 wt% which was in the same range as that of the Fe study (Paper I discussed in section 4.1) where the catalyst was NiMo on alumina and oleic acid as feed. The coking is one of the main causes of deactivation during HDO reactions. Also, HDO reactions are more exothermic than HDS which can increase the rate of coking. However, as a routine shutdown procedure in the refinery, the catalyst bed was stripped with hydrogen before unloading which might have removed some of the carbon deposits from the catalyst. The sulfur content of the fresh catalyst sample was negligible while that of spent and washed samples was 6 and 6.6 wt% respectively. This is in a reasonable theoretical range to consider the catalyst to be fully sulfided.

Table 4.8 Textural properties, elemental and ICP analysis of model catalyst samples used in refinery operation.

Samples / Analysis	*Alumina [R]*	*Fresh [R]*	*Spent [R]*	*Washed [R]*	*Calcined [R]*
BET surface area [m^2g^{-1}]	139	120	94	-	119
Pore Volume [cm^3g^{-1}]	0.40	0.32	0.24	-	0.32
Avg Pore Size [Å]	116	107	102	-	109
Carbon [wt%]	0.1	0.0	1.1	0.0	0.1
Hydrogen [wt%]	0.3	0.8	1.1	1.2	0.5
Sulfur [wt%]	<0.1	0.2	6.0	6.6	0.0
Nitrogen [wt%]	<0.05	0.1	<0.05	0.0	<0.05
Nickel [wt%]	<0.1	1.8	1.8	0.5	1.7
Molybdenum [wt%]	<0.1	11	11	7	10

ICP results shows that the fresh catalyst samples contained 1.8 wt% Ni and 11 wt% Mo (refer Table 4.8). The amount of Ni and Mo was same for the Spent[R] sample as well which indicates that there was no leaching during refinery operations. It should however be noted that the amount of Ni and Mo on the washed sample was found to be considerably less. So, the same protocol of Soxhlet extraction was executed on the fresh catalyst sample and it was later found by ICP analysis that there was no loss of Ni and Mo. It seems that during the time on stream in refinery, the active metals (Ni and Mo) became dislodged from the support due to coking or other contaminants. This resulted in leaching of Ni and Mo during Soxhlet extraction. It has been observed during steam reforming reactions that carbon whiskers are formed. These carbon whiskers (or pillars) cause the displacement of Ni particles from the support by encapsulating them [72]. Then, some of the metal particles (Ni and Mo in this case) are being removed as carbon is washed away during the Soxhlet protocol. However, the Soxhlet extraction method was successful in removing the coke from the spent catalyst sample. The calcination treatment was effective in removing most of the carbon and sulfur from the Calcined [R] sample, with no loss of active metals (Ni and Mo). Additionally, the calcined sample recovered its surface area and pore volume compared to the fresh sample values. The major contaminants in the refinery samples are presented in Table 4.9. The first and

second group elements like Na, K, Ca and Mg have been summed up and classified as Alkalis for the sake of brevity. A detailed ICP analysis for about 70 elements was done on these refinery samples. On comparing fresh and spent catalysts samples, the increase in Fe, P and Alkalis was the largest. Also, as it can be seen in Table 4.9, some amount of poisons was removed during the Soxhlet extraction. The calcined sample lost a major portion of P while Fe and alkalis were removed to a certain extent as well.

Table 4.9 ICP analysis of refinery catalyst samples.

Contaminants (ppm)	Samples			
	Fresh[R]	Spent[R]	Washed [R]	Calcined[R]
Phosphorus, P	10	5000	2200	1400
Iron, Fe	50	3000	200	1300
Alkali (Na,K,Ca, Mg)	1200	2700	1000	1500

SEM-EDX analysis of the spent catalyst sample was done to see how these three major contaminants i.e Fe, P and Alkalis distribute through the catalyst particles. In Fig 4.17, the SEM EDX of Spent [R] sample from the refinery with normalized concentrations of Fe, P and Alkalis is plotted at two different lengths – surface to the center (depth of 2000 μm) and surface to a depth of 500 μm. The highest concentration for all three poisons was recorded at or near the surface. For Fe and P, their concentrations dropped to almost zero at a depth of 150 μm or so. In case of Alkalis, the concentration did not fall as much, since there were some Alkalis present in the support material to begin with. There seems to be a similarity in the concentration profiles of Fe and P which could be related to the similar nature (like large-size molecule, polarity etc.) of the poisoning compounds containing Fe and P. The distribution of active metals (Ni and Mo) were quite uniform throughout the particle (refer Fig S3 in Paper III).

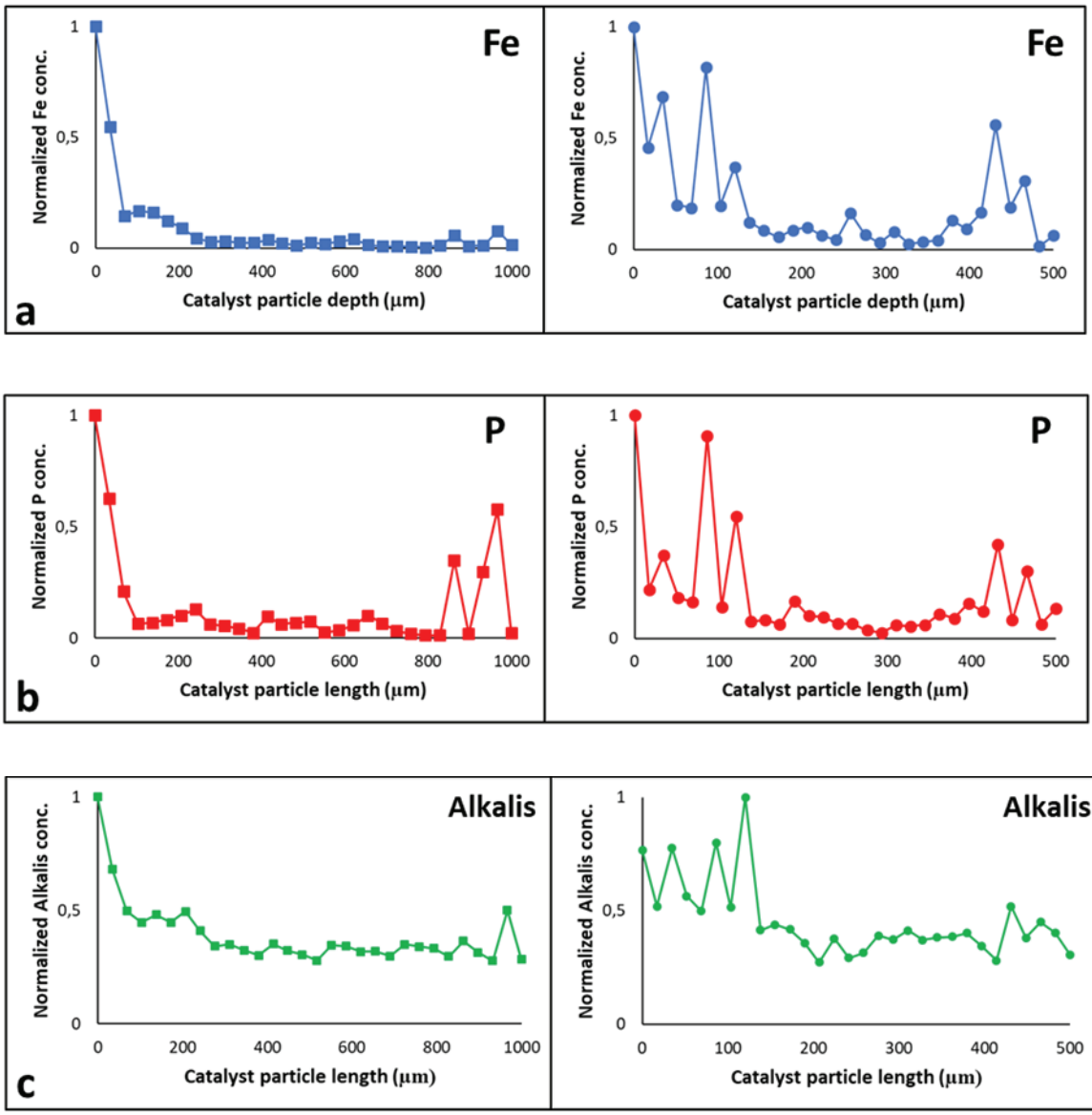

Fig 4.17. SEM EDX radial analysis of Spent[R] catalysts from refinery showing normalized distributions of poisons (a) Fe, (b) P and (c) Alkalis from the surface to center of spherical particle, i.e. 0 depth to a depth of 1000 µm (left) and 500 µm (right) into the particle.

4.3.2 Comparison of fresh, spent and regenerated catalysts

The catalyst activity of the refinery samples – ***Fresh[R], Spent[R], Calcined[R] and Washed[R]*** was compared during HDO of stearic acid at 50 bar of total pressure and 300 °C in the presence of hydrogen in a batch reactor. Fig 4.18 compares the results from these experiments.

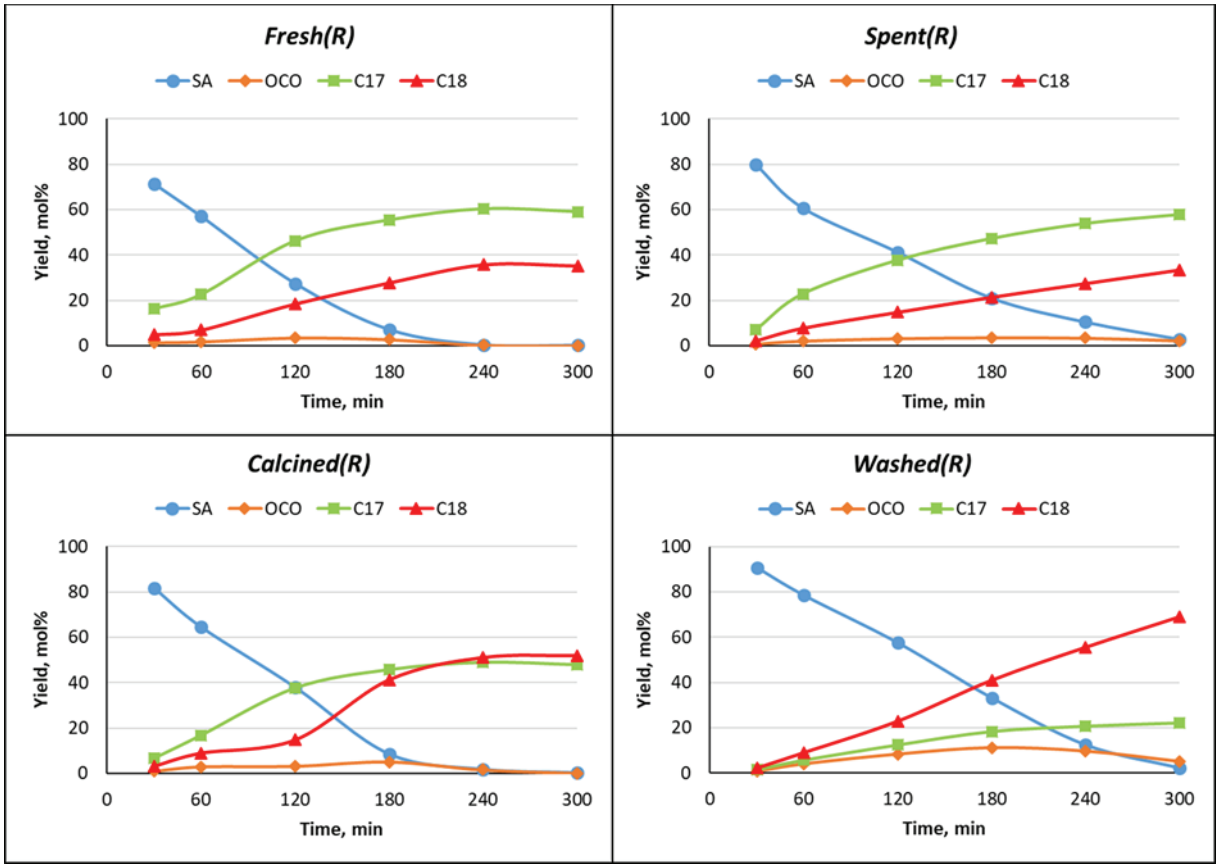

Fig 4.18 Laboratory experiments for HDO of stearic acid over refinery catalyst samples – Fresh [R], Spent [R], Calcined [R] and Washed [R]; Experimental conditions - Catalyst 0.4 g, Stearic acid (SA) as feed 4 g, Dodecane as solvent 150 ml, Pressure 50 bar (H_2) and Temperature 300 °C. SA – Stearic acid, OCO – Octadecanol, C17 – alkanes and alkenes isomers of C17 hydrocarbons, C18 – alkanes and alkenes isomers of C18 hydrocarbons.

The yield profiles of stearic acid (SA), octadecanol (OCO), heptadecane (C17) and octadecane (C18) are plotted against time. The conversion of SA was fastest for the fresh catalyst sample with the decarbonation route being preferred at the given reaction conditions. For the fresh catalyst sample, the yield of the other hydrocarbon product i.e. C18 via direct-HDO route was only 36 mol%. It is interesting to note that the selectivity for two routes was the same in the case of the Spent [R] sample as that of the fresh catalyst. Although, as expected, the conversion of SA was slower for the spent catalyst compared to the fresh catalyst. The activity and product selectivity of these four different refinery catalysts during HDO experiments is presented and compared in Fig 4.19.

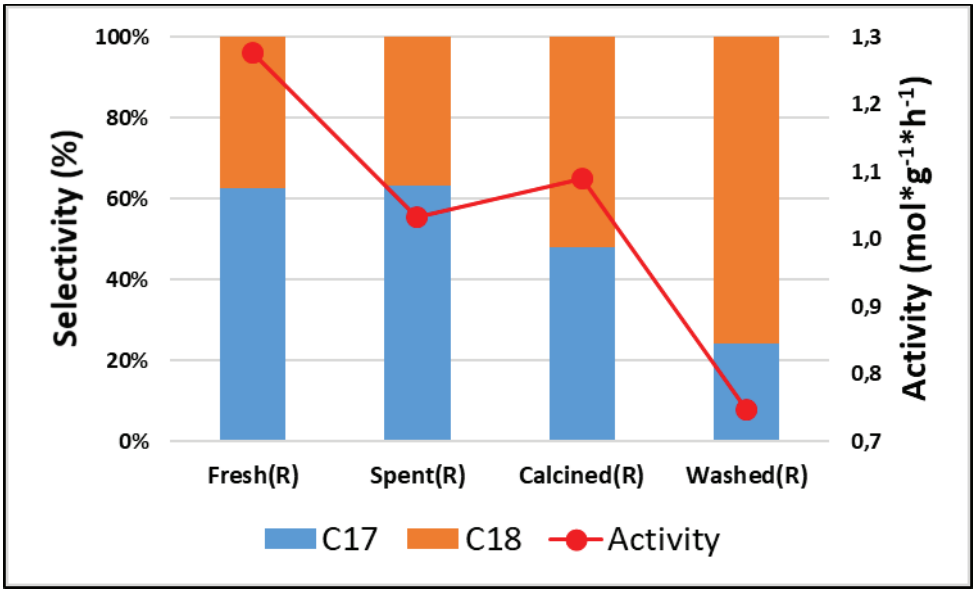

Fig 4.19 Comparison of catalyst initial activity and selectivity (C17) for Fresh [R], Spent [R], Calcined [R] and Washed [R] samples.

As it can be seen from the catalyst initial activity plot, the catalyst has lost its activity after being in the refinery for several months under harsh conditions and a range of contaminants are present in renewable oils. The catalyst activity of the fresh sample was higher by 24% compared to the spent catalyst. The calcination treatment helped a bit and resulted in a 6% increase in catalytic activity. This is due to the fact that most of the carbon and phosphorus were removed which made the active sites more accessible. The product distribution for the calcined sample was different than to that of the fresh sample. Now, the direct-HDO route was the major route with a contribution of 52%. For the Washed [R] sample, a loss of 28% in catalyst activity was observed. This can be explained due to the leaching of active metal species discussed in the previous section 4.4.1. The loss of Ni was larger than Mo due to the Soxhlet extraction which was evident from the product distribution of hydrocarbons. Selectivity for C17 and C18 products were 24% and 76% respectively. This is an expected scenario since the unpromoted MoS_2 catalyst prefers the direct-HDO route [15].

4.3.3 The role of poisons during HDO

a. The effect of Iron (Fe)

A complex of Fe containing compound, i.e. iron stearate, was employed at three different concentration of 1, 2 and 5 wt% to evaluate the effect of iron (Fe) on catalyst deactivation. It should be noted that the amount of poison is the total amount of the poison element added with respect to catalyst mass in the batch reactor. However, the amount of Fe found on the spent catalyst (recovered after the batch experiment) was significantly less. For example, in the Fe 5 wt% experiment, it resulted in only 1480 ppm of Fe on the spent catalyst as per the ICP analysis. This amount is in the same range as that of the Fe deposited on the refinery sample (see Table 4.9). An additional experiment with iron nitrate ($FeNO_3$) at 2 wt% was carried out to differentiate the anions with different stearic hinderance potential i.e. nitrate and stearate. Catalyst activity was compared on the basis of conversion of stearic acid. The yields of two major products i.e. C17 and C18 hydrocarbons were plotted while intermediates like octadecanal and octadecanol were

insignificant at the given reaction conditions. Fig 4.20 presents the yields of stearic acid and production of C17 and C18 hydrocarbons at 30, 60, 120, 180, 240 and 300 min time intervals.

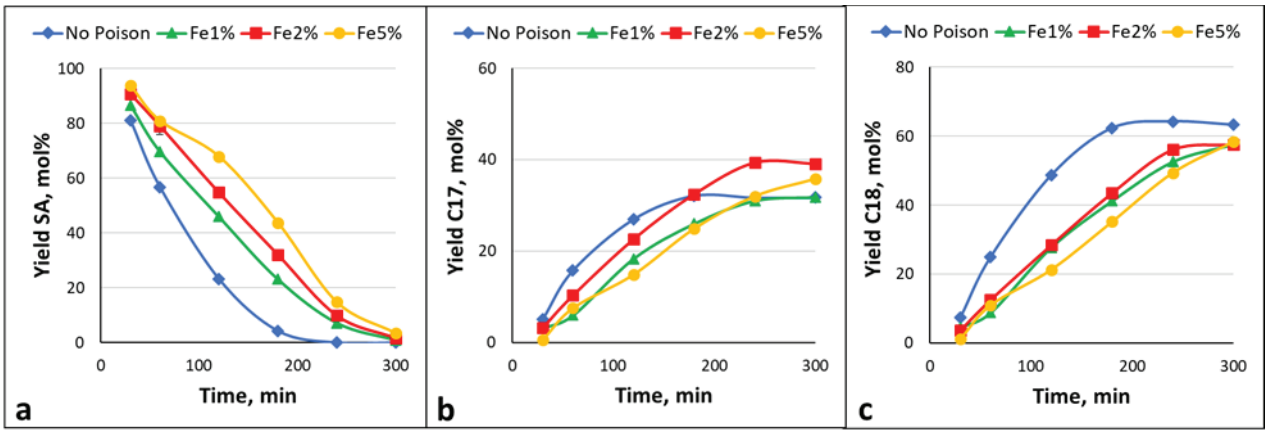

Fig 4.20 Yield of SA (a), yield of C17 (b) and yield of C18 (c) hydrocarbons during HDO of stearic acid over NiMo catalysts with varying iron complex concentration (Fe in feed per mass of catalyst); Experimental conditions - Catalyst 1 g, Stearic acid (SA) as feed 4 g, Dodecane as solvent 150 ml, Pressure 50 bar (H_2) and Temperature 300 °C.

It should be noted that for Fe 5% experiment, the carbon mass balance was slightly higher, still in the range of 100-110% since there was some additional stearate from the poison complex which resulted in increased initial moles of stearic acid in the reaction mixture to begin with. In Fig 4.20a, the stearic acid conversion was the fastest in the no poison experiment and rate of reaction decreased with the increasing amount of poison in the reaction mixture. To compare the 180 min samples, around 4 mol% of stearic acid remained in the "No Poison" experiment, whereas in case of Fe 5% experiment the amount of stearic acid left was at 44 mol%. However, there seems to be no apparent trend in the selectivity of C17 products at different Fe concentrations (see Fig 4.20b). In the case of direct-HDO route, the amount of C18 products formed in the presence of the Fe poison was lower than compared to the baseline experiment. It should be noted that the study (Paper I) discussed in section 4.1, it was found that that Fe could influence the selectivity of the NiMo catalysts during hydrodeoxygenation of Oleic acid [16]. It was concluded based on TEM-EDX analysis of spent catalyst samples that Fe preferentially deposits near the Ni-rich active sites which lead to suppression of the decarbonation route. This difference could be explained as the catalyst particles were of different sizes – in section 4.1 (Paper I), it was in a powder form (150–200 µm) while here (Paper III), it is spheres with a size range of 1.70-1.90 mm, thus several magnitudes larger in size. Hence, it is expected that the distribution of Fe would be more remarkable and uniform in the former case. Also, the objective of using larger spheres in this study was to introduce mass transfer limitations (closer to the refinery situation) and illustrate how that influenced the distribution of different poisons through the catalyst particle.

b. The effect of Potassium (K)

To study the impact of K, three different concentrations – 1, 2 and 5 wt% of potassium nitrate were added to the reaction mixture. Fig 4.21 exhibits the effect of K on oxygenate conversion and product formation via two routes. At 5 wt% K concentration, a substantial drop in

the rate of conversion of stearic acid was reported. For the no poison experiment only 4 mol% of stearic acid remained while it was 39 mol% of stearic acid for K 5% experiment after 180 min. In an earlier study, it was proposed that the vacancy sites on the slab edges of MoS_2 could be blocked by K which results in a large drop in HDO activity at a given poison to catalyst ratio [25]. A similar phenomenon is seen here (see Fig 4.21 a) as well, since there was not much drop in catalytic activity at 1 and 2 wt% concentration, since K may be insufficient to significantly block the active sites. The change in selectivity with the addition of K is shown in Fig 4.21 b and c, with a larger drop in the production of C18 products and a minor increase in the production of C17 products. There was a modest increase in C17 yield from 32 to 39 mol% whereas the decrease in C18 hydrocarbon was from 64 to 47 mol% when the baseline and the experiment with highest poison concentration were compared. So, it could be summarized that the poisoning effects due to K are not linear with the concentration. It seems that the amount of K at 2 wt% experiment is below a certain threshold limit to cause significant catalyst deactivation.

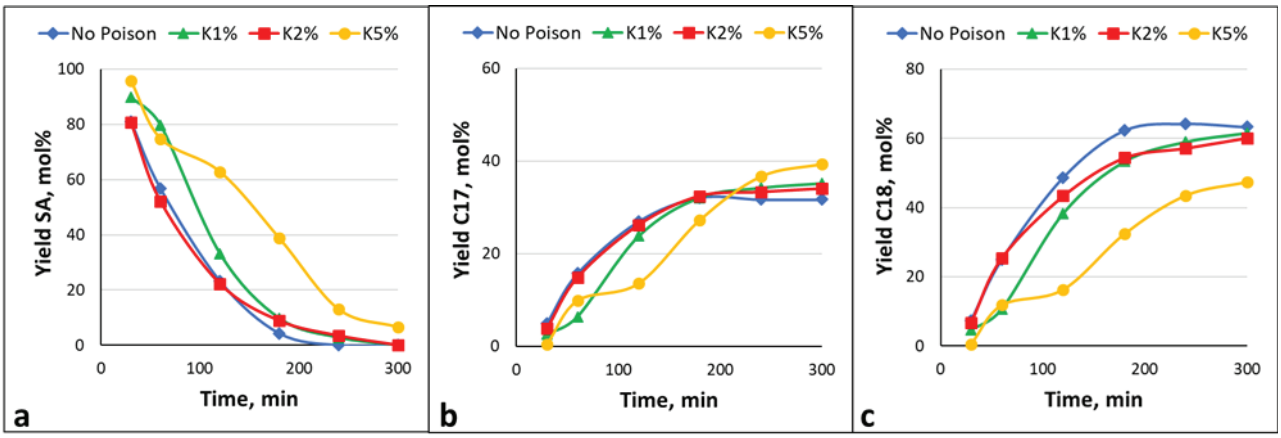

Fig 4.21 Yield of SA (a), yield of C17 (b) and yield of C18 (c) hydrocarbons during HDO of stearic acid over NiMo catalysts with varying potassium nitrate concentration (K in feed per mass of catalyst); Experimental conditions - Catalyst 1 g, Stearic. acid (SA) as feed 4g, Dodecane as solvent 150 ml, Pressure 50 bar (H_2) and Temperature 300 °C.

c. The effect of phospholipid containing P and Na

The catalyst deactivation due to fouling by P and Na was tested using a phosphatidic acid molecule at three different concentration – 1, 2 and 5 wt%. This is a type of a phospholipid molecule which undergoes hydrolysis decomposition to yield one molecule each of glycerol, phosphoric acid with a counter ion as sodium and two molecules of fatty acids. Phsopholipids are commonly present in biomass-based feedstocks as they are a major component of cell membranes in plants etc. Also, the other renewable feedstocks like waste cooking oil contains phospholipids in varying amounts [73]. It has been shown in previous studies that these phospholipids molecules can form deposits of phosphate complexes with alkalis or alumina which can lead to plugging of the catalyst bed. It is of high importance to know how the phospholipid molecules containing P and Na diffuse through the catalyst pores resulting in catalyst deactivation. The three different concentrations 1,2 and 5 wt% corresponds to P while it was 0.7, 1.5 and 3.7 wt% w.r.t Na. The effect of phospholipids on oxygenate conversion and product formation with varying amounts is presented in Fig 4.22. There was a negative impact on the conversion of stearic acid with increasing concentration of the P and Na containing compound (see Fig 4.22 a). The drop

in catalyst activity started to appear from concentration 2 wt% of P/Na and higher. At 180 mins, the amount of stearic acid remaining in the reaction mixture was 4 mol% with no poison, whereas it was 29 mol% with 5 wt% P/Na experiment. The change in selectivity was quite apparent with the introduction of phospholipid molecule. The contribution of the decarbonation route increased when P and Na were present in the 2-5 wt% concentration range. The addition of P can influence the textural and acidic properties of the catalyst which can have an impact on the selectivity of the catalyst [53, 74]. As it was observed in section 4.2 that the selectivity for C17 product decreased with the introduction of P containing phospholipid molecule. The amount of P employed in section 4.2 ranged from 179-532 ppm in liquid feed, which is equivalent to a dosing of 4-12 wt% in the units used in the current section of 4.4 for comparison. Though, it should be highlighted that the P complex used in these two studies was also different. In the previous study (refer section 4.2), it was phosphatidylcholine with choline as the head group which is different from the phosphatidic acid compound used in this study (section 4.3) which contained Na as a counter ion (see Fig 3.2b). While in the former case, the choline moiety would decompose to ammonia leaving no counter ion available. This could lead to the formation of phosphoric acid if no counter ion is present. Also, it has been proposed that severe catalyst deactivation is likely in the presence of phosphoric acid as it can act as an oligomerization catalyst [48].

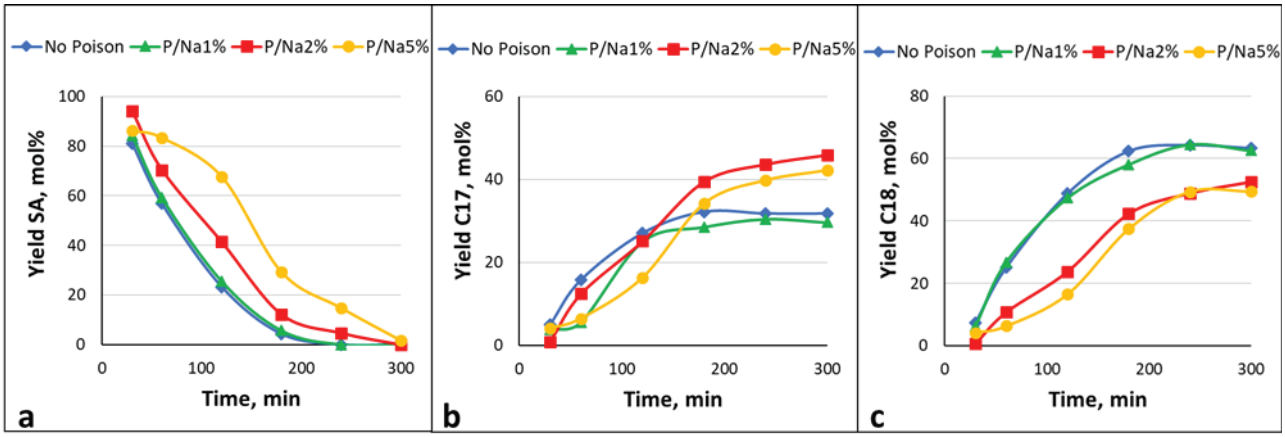

Fig 4.22 Yield of SA (a), yield of C17 (b) and yield of C18 (c) hydrocarbons during HDO of stearic acid over NiMo catalysts with varying phosphorus complex concentration (P/Na in feed per mass of catalyst); Experimental conditions - Catalyst 1 g, Stearic acid (SA) as feed 4 g, Dodecane as solvent 150 ml, Pressure 50 bar (H_2) and Temperature 300 °C.

d. Influence of type of Fe poison complex and combinations of poisoning metals

In this set of experiments, the effect of different Fe-bearing compounds and a mixture of all three poisons (discussed above) were tested. In Fig 4.23, the effect of two iron complexes with different anionic parts as stearate and nitrate have been compared. Also, a combination of Fe, P/Na and K with a total feed concentration at 2 wt% (0.67 wt% each) was evaluated. As it can be seen in Fig 4.23 a, the conversion of fatty acids was quite similar which suggest that the difference in influence of iron stearate and iron nitrate is rather negligible. Also, the final selectivities for C17 and C18 products was quite close irrespective of the anion. Thus, it can be derived that the counter ion of Fe complex does not seem to have much impact on the poisoning, at least for these two compounds. Also, the rate of conversion of stearic acid was similar for Mix 2 wt% and Fe 2 wt% experiments. This suggest that there were no significant synergies between Fe, P/Na and K where

they might have an increased catalyst poisoning. Their effects thus seem to be independent of each other.

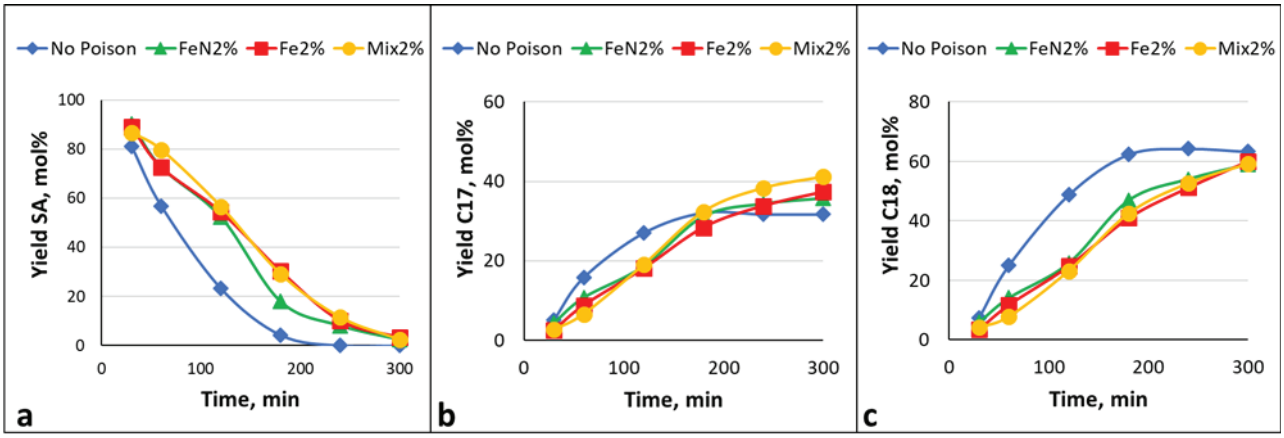

Fig 4.23 Yield of SA (a), yield of C17 (b) and yield of C18 (c) hydrocarbons during HDO of stearic acid over NiMo catalysts with poisons including iron nitrate (FeN), iron stearate (Fe) and mixture of Fe, P and K compounds ; Experimental conditions - Catalyst 1 g, Stearic acid (SA) as feed 4 g, Dodecane as solvent 150 ml, Pressure 50 bar (H_2) and Temperature 300 °C.

A comparison of catalyst activity and selectivity for the decarbonation route (C17) for all experiments in this study can be seen in Fig 4.24. It confirms that all three selected poison compounds were “effective” and caused catalyst deactivation. Also, for all three poisons Fe, P/Na and K, there was a drop in the catalyst activity with the increase in the concentration. At the highest poison concentration i.e. 5 wt% concentration, the activity of the catalyst plunged more than 50%. The most deactivation resulted from the iron complex especially at the lower concentration compared to the other two poisons. It has been proposed that these fatty acids molecules are known to bind very strongly on the active sites of catalysts which can cause the pseudo-deficiency of hydrogen at the catalytic sites [75, 76]. We know that the hydrogen is needed in each step along the direct-HDO route in the given reaction network [75]. So, indirectly, the decarbonation route should have been favored due to the scarcity of hydrogen. Thus if only the crowding of the poison molecules is taken into consideration then it should have resulted in higher selectivity for C17 products. This can be seen in Fig 4.24 b. There was increased selectivity for C17 hydrocarbons at the 5 wt% experiments for each type of poison used. However, it should be acknowledged that there are additional factors like stearic hinderance due to the poison containing molecule or poisoning element interactions with the active metal species or support etc. This will be quite difficult to fully understand the scope of these factors although the experiments with iron nitrate and mix of poisons have provided some insight. The increased selectivity for C17 hydrocarbons in phospholipids poisoned experiments could be explained due to the strong binding of P/Na containing molecules on the catalyst surface, leading to shortage of hydrogen molecules at the active sites. This seems to result in the increased contribution of the decarbonation route.

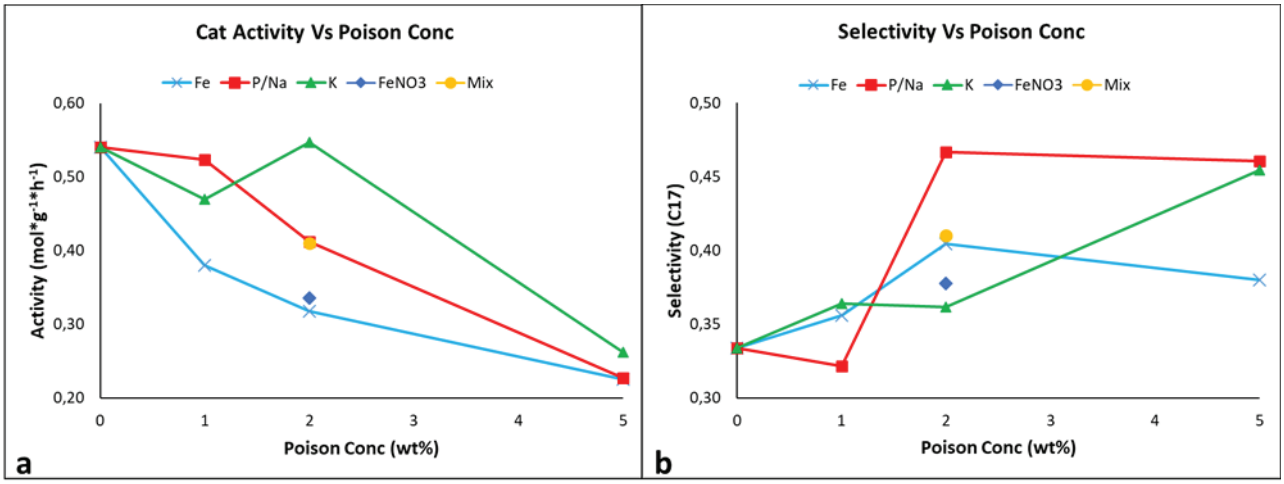

Fig 4.24 Comparison of initial activity (a) and C17 selectivity (b) for different poison concentrations (poison in feed per mass of catalyst) and their mixture at varying concentrations.

4.3.4 Catalyst characterization and distribution of poison in lab-tested catalysts

The results from N_2 physisorption, elemental and ICP analysis of samples used in the batch reactor are listed in Table 4.10. The amount of poison deposited on the catalyst from 5 wt% experiments were - 1480, 6950, 242 and 315 ppm for Fe, K, P and Na respectively (see Table 4.10). This indicates that there was a large variation in the amount of poison element deposited on the catalyst. The spent catalyst recovered after the experiment lost around one-third of its original surface area and pore volume for all three poisons from the highest poison concentration experiment. It seems that these poisons masked the active sites on the catalyst surface, corroborated by the drop in activity from results shown in Fig 4.24. Also, it is apparent that the poisons (Fe, K, P and Na) result in pore blockage. It was observed that there was a large reduction in pores with size greater than 70 Å (see Fig S1 in Paper III). Also, we compared an additional parameter i.e. drop in surface area per unit of deposited element after the experiment for the samples from catalysts from Fe, P/Na and K 5 wt% experiments. The amount of poison element deposited in ppm were 1480 (Fe), 557 (P+Na) and 6950 (K) while the surface area of spent catalyst samples were 123, 119 and 129 m^2g^{-1} respectively. It can be seen that the phosphatic acid caused the largest drop in surface area per quantity of deposited poisoning element. The amount of carbon deposited was in the range of 12-16 wt% for the 5 wt% experiments. However, it is difficult to conclude anything from the coking results as the conversion of oxygenates was not 100%.

Table 4.10 Textural, Elemental and ICP analyses of support, fresh, baseline and poisoned catalyst sample for laboratory batch reactor experiments.

Sample/ Analysis	BET surface area [m^2g^{-1}]	Pore Volume [cm^3g^{-1}]	Avg Pore Size [Å]	Carbon [wt%]	Sulfur [wt%]	Hydrogen [wt%]	Poison element [ppm]
Alumina	213	0.53	100	1.0	<0.1	1.0	-
Fresh NiMo	179	0.42	94	0.5	<0.1	0.7	-
No poison	171	0.37	92	1.3	5.7	1.0	-
Fe 5wt%	123	0.26	85	14.0	5.4	3.0	1480
P/Na 5wt%	119	0.27	89	12.8	5.7	2.7	242 (P); 315 (Na)
K 5wt%	129	0.28	86	16.5	5.3	3.2	6950

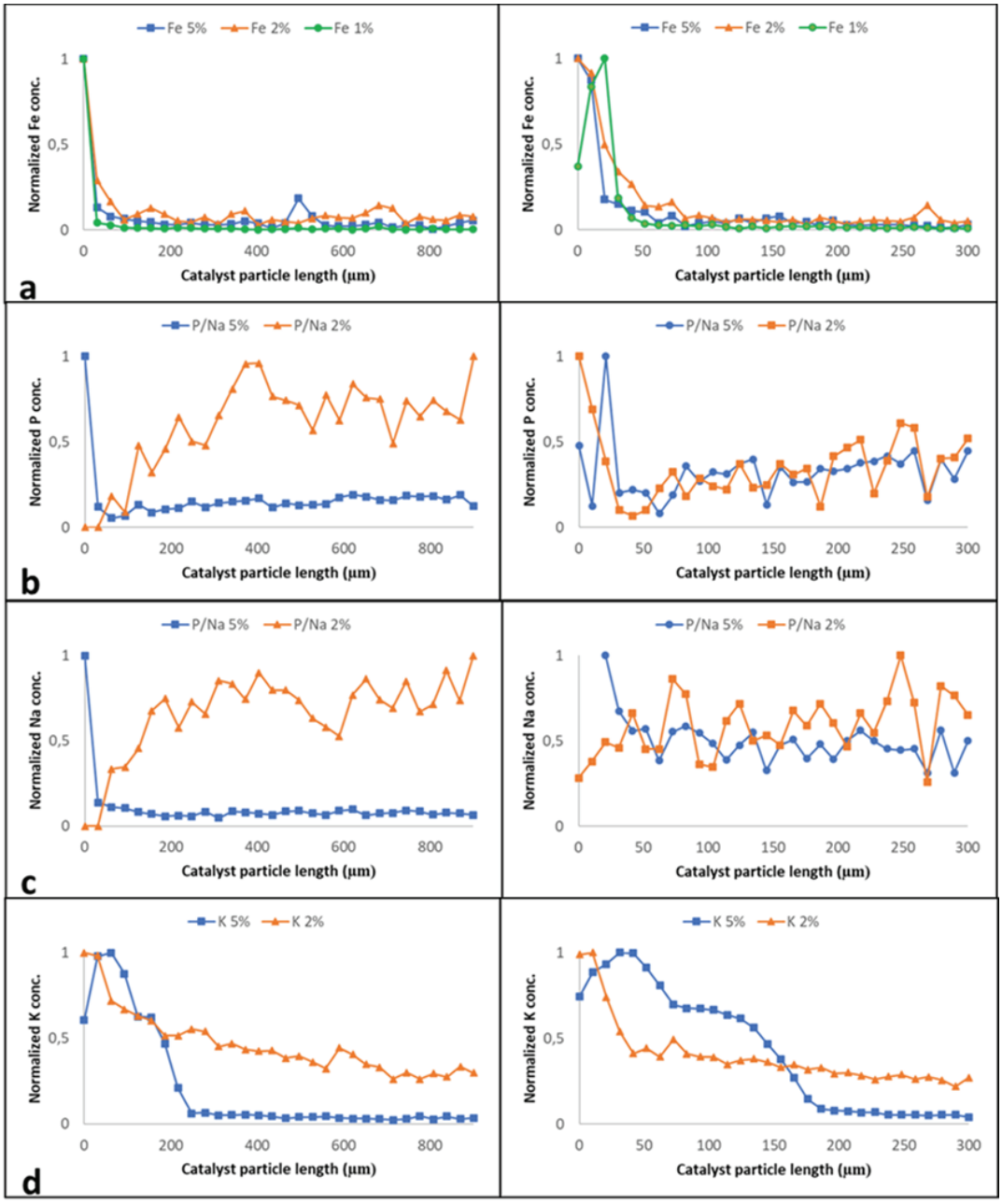

Fig 4.25 SEM EDX radial analysis of spent catalysts from poisoned experiments showing distributions of poisons (a) Fe, (b) P, (c) Na and (d) K from the surface to center of sphere (0 depth) to a depth of 900 µm (left) and 300 µm (right) into the particle.

SEM EDX radial analysis was done and the average normalized distribution of different poisons (Fe, P, Na and K) is presented in Fig 4.25. The normalized concentration along the catalyst particle length gives an idea about how these poisons deposited and how different poison species would have diffused through the catalyst pores. The spherical particles were cut into half and radial analysis was done at two lengths of 900 and 300 µm along the flat surfaces. The first measure of 900 µm is the distance from the surface (edge) to the center while second analysis over the length of 300 µm was to focus on the distribution near the surface. It must be pointed out that for SEM-EDX only a limited number of particles were analyzed which might result in some uncertainties.

Also, it is not possible to ensure that all the analyzed particles have been cut in the exact same way so that their exact cross-section is exposed and analyzed. Also, there could be some ambiguity with these highly localized poison concentrations due to higher than average concentration of Ni/Mo active sites. As it can be seen in Fig 4.25 (a), (b), (c) and (d), the distribution of poisons is somewhat varying through the analyzed length. In Fig 4.25 (a) for Fe, most of the metal seems to have deposited on the surface and the concentration dropped to the baseline at a depth of 100 μm or so. It was the same trend in the case of the Fe distribution in the refinery sample (refer Fig 4.17). The distribution pattern was similar at all three concentrations of the Fe complex employed. The higher concentration of iron deposited on surface or near to the surface for both cases – refinery and laboratory and batch experiments can be attributed to transport limitations in case of stearic acid and especially the poison compounds containing stearate ligands to a certain extent. The concentration profile of samples with phospholipid as poison is showcased in Fig 4.25 (b) for P and Fig 4.25 (c) for Na. The distribution of P and Na was found out to be highest at or near the surface which is similar to that of Fe at the highest (5 wt%) poison concentration. In case of lower (2 wt%) poison concentration, the distribution of P and Na was evenly distributed throughout the particle. The distribution profiles of P and Na were quite similar for 2 and 5 wt% samples which suggest that P and Na could be a part of a compound and diffusing as one entity. As the deposition of P and Na would happen near the surface, it would result in increased transport limitations so that the diffusion for the phospholipids, but also most likely for stearic acid (feed), is greatly reduced. This is validated by the BET results which shows that the surface area and pore volume decreased as the poisons deposits. The same could be observed for other poison elements i.e. Fe and K. The radial distribution for K was concentration dependent. The concentration of K near surface is highest as well but its gradient is different. The concentration profile of K comes to zero at a depth of around 200 μm. This could be explained either due to the smaller atomic size of K or the smaller steric hinderance of potassium nitrate when compared to iron stearate. The individual contributions of P and Na to the catalyst deactivation is quite difficult to determine. We think it is both P and Na together as parts of the phospholipid molecule causing changes in catalyst activity and selectivity as they are deposited in smaller amounts (compared to Fe and K).

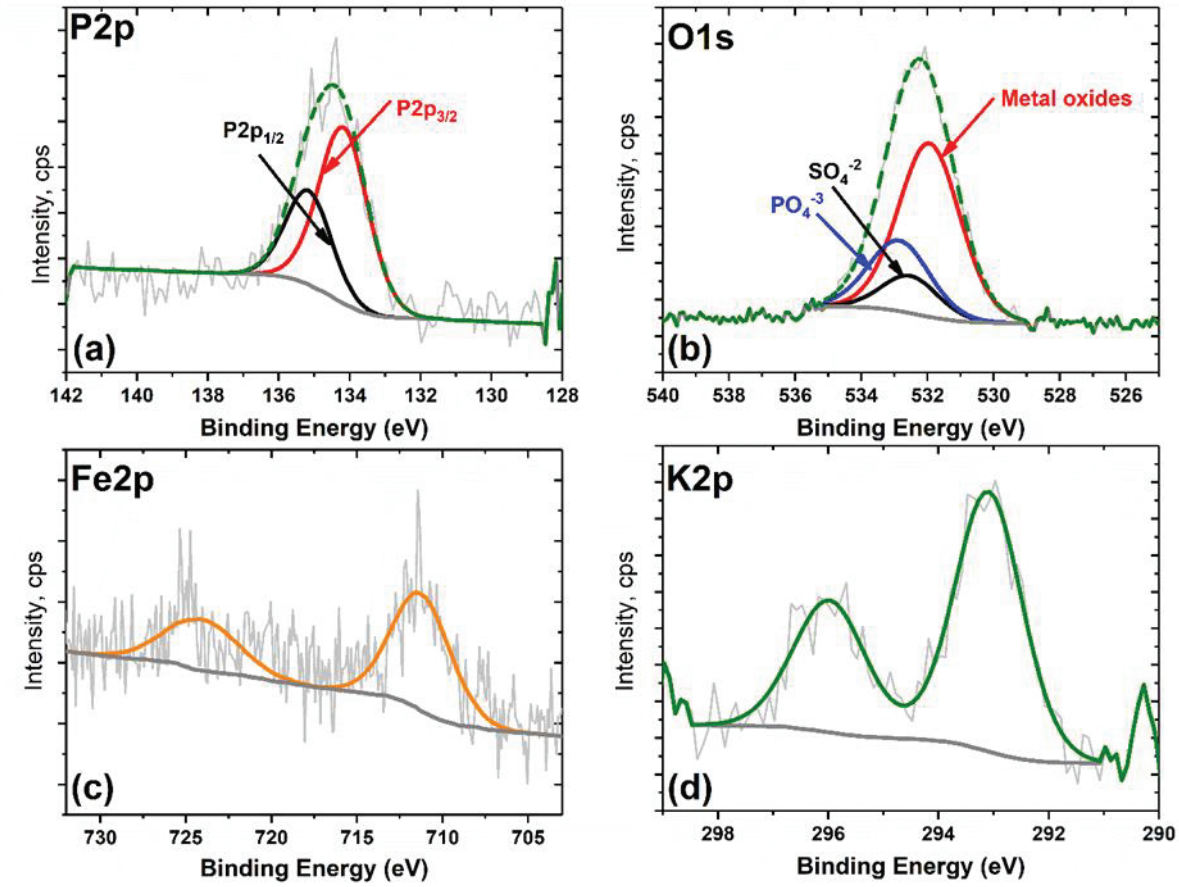

Fig 4.26 XPS analysis of spent catalysts from poisoned experiments showing core level spectra (a) P2p of P/Na 5 wt% sample, (b) O1s of P/Na 5 wt% sample, (c) Fe2p of Fe 5 wt% sample (d) K2p of K 5 wt% sample.

Fig 4.26 shows the XPS analysis of spent catalyst samples from 5 wt% experiments with core level spectra of P/Na, Fe and K corresponding compounds. Surface composition was determined at three depths of 0, 5 and 50 Å which confirmed the poisoning elements – Fe, P and K with an average of 2, 5 and 3 atomic% respectively. The amount of Ni on these three samples was found to be quite low at these superficial depths which was indicated by SEM EDX results as well (see Fig S4 in Paper III). The peaks at binding energies of 134.2 eV ($P2p_{3/2}$) and 135.1 eV ($P2p_{1/2}$) corresponds to the presence of P in the oxidation state of +5 as shown in Fig 4.26 (a) and (b) for the P2p and O1s core level spectra of P 5 wt% spent catalyst sample. Phosphate (532.9 eV) like species was confirmed by the deconvolution of O1s peak. It has been previously reported that phospholipids can interact with alumina support to yield $AlPO_4$ complexes resulting in deterioration of the support structure [53]. However, in this study the counter ion in phospholipid complex was Na and there is an overlapping distribution of P and Na so it is quite probable that alkali phosphates would have formed in these catalyst samples. These sulfided catalysts tend to superficially oxidize upon exposure to air during their handling and transferring to the XPS instrument [77]. This seems to be indicated by O1s peak at 532.5 eV which corresponds to sulfate species. In Fig 4.26 (c) and (d), from Fe2p (711.3 eV for $2p_{3/2}$ and 724.1 eV for $2p_{1/2}$) and K2p (293.1 eV for $2p_{3/2}$ and 295.9 eV for $2p_{1/2}$) peaks, it was concluded that the other two poisoned samples had species in the form of K^+ and Fe^{3+}.

4.4 Kinetic study for HDO of SA

4.4.1 Kinetic experimental results

A set of experiments were planned for the development of the kinetic model (see Table 3.4). Stearic acid, octadecanal, octadecanol, isomers of heptadecene and octadecene, heptadecane and octadecane were the common species observed in the liquid phase of these experiments. These following abbreviations were used for the given components - "Stearic acid – SA", "Octadecanal – C18=O", "Octadecanol – C18-OH". Saturated and unsaturated isomers of C17 and C18 molecules were lumped together and represented by "C17+" and "C18+". There were a few other compounds observed in the liquid phase which were less than 1% of the C-mole balance and thus ignored. These involved myristic acid, tridecane, tetradecane and stearyl stearate. Reaction schemes proposed by different research groups can be broadly divided into two groups, one in which C18-OH is the intermediate [53, 54] and the other in which C18=O is proposed to be the intermediate after catalytic reduction of SA [16, 20, 40]. Therefore, we carried out HDO experiments employing the intermediates like octadecanol and octadecanal to illustrate and confirm the overall reaction scheme for HDO of SA. Gaseous samples were analyzed and CO, CO_2 and CH_4 were detected in the gas samples. Decarbonylation and decarboxylation steps during HDO of SA would yield CO and CO_2 respectively. However, these could be formed from one another by the water gas shift (WGS) reaction as well. Table 4.11 presents the results from the gas analysis. These results also helped to establish the reaction scheme for HDO of SA.

Table 4.11 Concentrations of carbon containing compounds in dry gas at varying reaction time or at the end of the experiment (final).

Feed component	Time (min)	Pressure (bar)	Temp(°C)	Catalyst wt. (g)	CO (mol%)	CO_2 (mol%)	CH_4 (mol%)
SA	40	50	300	0.4	1.48	0.10	0.08
SA	90	50	300	0.4	1.78	0.49	0.18
SA	180 (final)	50	300	0.4	0.88	0.83	0.54
C18-OH	270 (final)	50	275	0.04	0.00	0.00	1.01
C18=O	270 (final)	50	275	0.04	0.58	0.02	0.04

4.4.1.a HDO of Octadecanol (C18-OH)

HDO of C18-OH was carried out at lower temperature and catalyst-to-feed ratio to monitor the conversion of reactants and formation of intermediates and products. The reaction conditions were as follows; 50 bar and 275 °C with 0.04 g of catalyst. At the end of the experiment i.e. 270 min, slightly more than half (53%) of the initial octadecanol molecules had reacted. The product distribution in the liquid phase was 51% of C18+ and 1.2% of C17+ hydrocarbons. Fig 4.27 depicts the change in the concentration of these species. Direct-HDO was found to be the major preferred route and the selectivity for C18+ hydrocarbons was 98%. The conversion of octadecanol and the formation of C18+ products was almost linear with time. Unsaturated hydrocarbons were the intermediates formed during the dehydration of octdadecanol, subsequently hydrogenated to

yield C18 alkanes. A small amount of C18=O was also observed from GC analysis of the liquid products. It suggests a minor formation of octadecanal from octadecanol. The presence of small amounts of aldehyde explains the low final yield of C17+ products of only 1.2%, which would have formed from the decarbonylation route. In the gas phase results, methane was the main carbon-containing component in the gas sample collected at the end of the experiment, while carbon oxides were in traces. Therefore, it could be concluded that C18-OH is the only intermediate for the direct-HDO route in a reaction scheme for HDO of SA over NiMo catalysts.

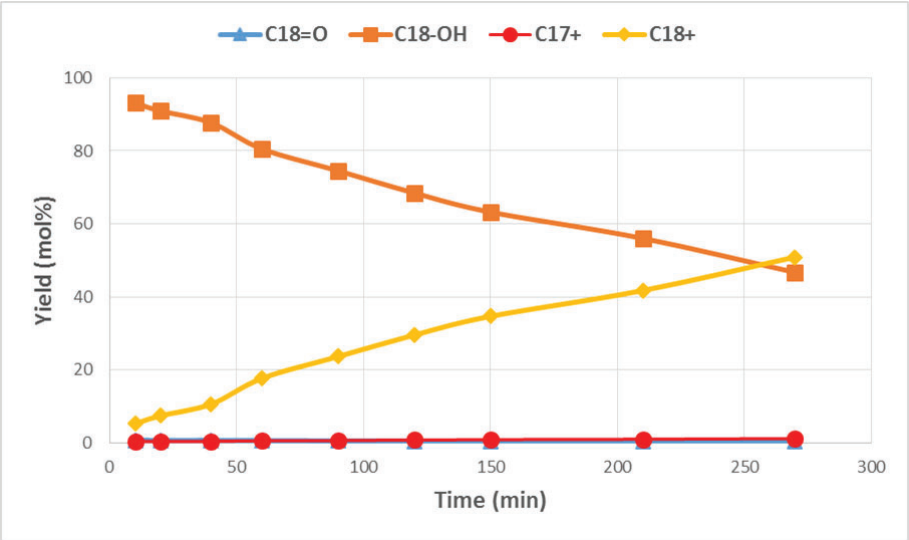

Fig 4.27 HDO of Octadecanol (C18-OH) at 275°C, hydrogen pressure 50 bar, feed 5 wt% C18-OH, catalyst mass 0.04 g, stirring rate 1000 rpm. Symbols are experiments, curves indicate trends.

4.4.1.b HDO of Octadecanal (C18=O)

HDO of Octadecanal (C18=O) was carried out at the same reaction conditions as above due to its high reactivity - 50 bar and 275 °C with 0.04 g of catalyst. As mentioned in Section 4.2.1, a few research studies suggest that HDO of SA proceeds via C18=O [16, 20, 40]. However, this has not been experimentally established since it has been observed only in trace amounts. Also, there is a lack of clarity about the contribution of decarboxylation and decarbonylation routes to yield C17+ hydrocarbons in the existing literature. Fig 4.28 depicts the concentration profile of C18=O, C17+ and C18+ during the HDO of C18=O. Octadecanal reacted at a fast rate such that it achieved 100% conversion in just 150 minutes. The formation of C17 hydrocarbons occurred quite fast as it attained a yield of 14% in the first hour of the experiment and remained constant thereafter. It is evident from Fig 4.27 and 4.28 that the selectivity for the direct-HDO route is higher with C18=O as feed compared to starting SA as feed. The sum of the final yields of C18-OH and C18+ could be regarded as the total selectivity for direct-HDO route when the conversion is not complete. When starting with C18=O feed (Fig 4.28) and for SA feed (Fig 4.29) at same conditions (275 °C and 50 bar) the contribution of direct-HDO were 85% and 73% respectively. The yield of octadecanol attained a maxima of 60% at 90 min and reacted very slowly afterwards. In the gas phase (refer Table 4.11), the major fraction was found to be CO, while CO_2 was detected in traces. This also validates that the most of the C17+ was likely formed from the decarbonylation route.

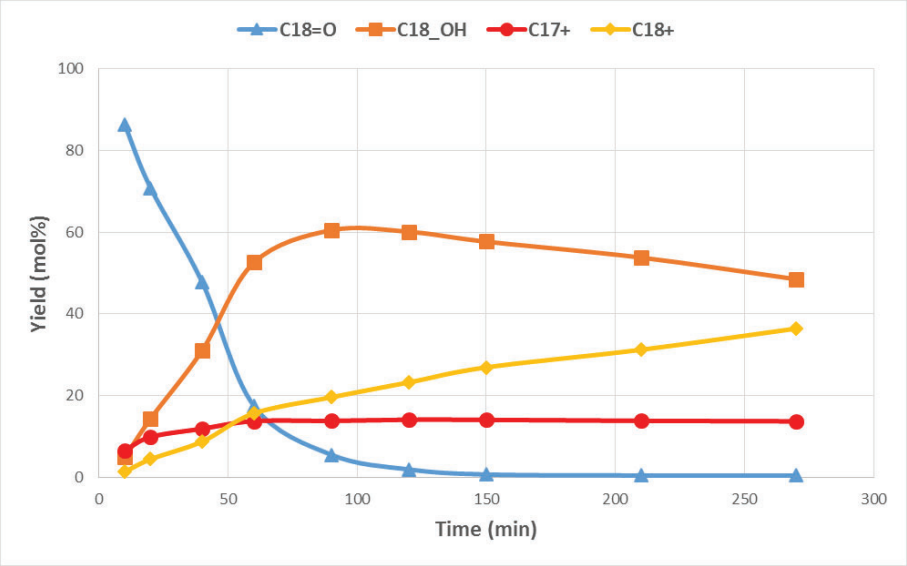

Fig 4.28 HDO of Octadecanal (C18=O) at 275°C, hydrogen pressure 50 bar, feed 5 wt% C18=O, catalyst mass 0.04 g, stirring rate 1000 rpm. Symbols are experiments, curves indicate trends.

4.4.1.c HDO of Stearic acid (SA)

A series of HDO experiments with SA as feed component over a range of temperature (275-325 °C), pressure (40-70 bar hydrogen), feed concentration (2-8 wt%) and stirring rate (500-1000 rpm) were carried out (see Table 3.4). Fig 4.29 represents the effect of temperature on the concentration profile of different molecules during the HDO reaction. It is evident that with the increase in temperature the rate of conversion of SA increased drastically. Time taken to achieve almost complete conversion of SA was 90, 120 and 180 minutes at 275, 300 and 325 °C respectively. Intermediates were octadecanal and octadecanol, as expected. Lower temperature resulted in a higher maxima concentration for the alcohol species with a typical concentration profile for an intermediate. Octadecanol went up to 44% at 275 °C while only 15% at 325 °C. The same effect was reflected in the selectivities for C17+ and C18+ hydrocarbons. The decarbonation route was preferred at the higher temperature. From the gas phase analysis (refer Table 4.11), the amount of CO during the initial time period of the experiment (at 40 and 90 mins) was much higher. The amount of CO went down as it was reduced to CH_4 via methanation.

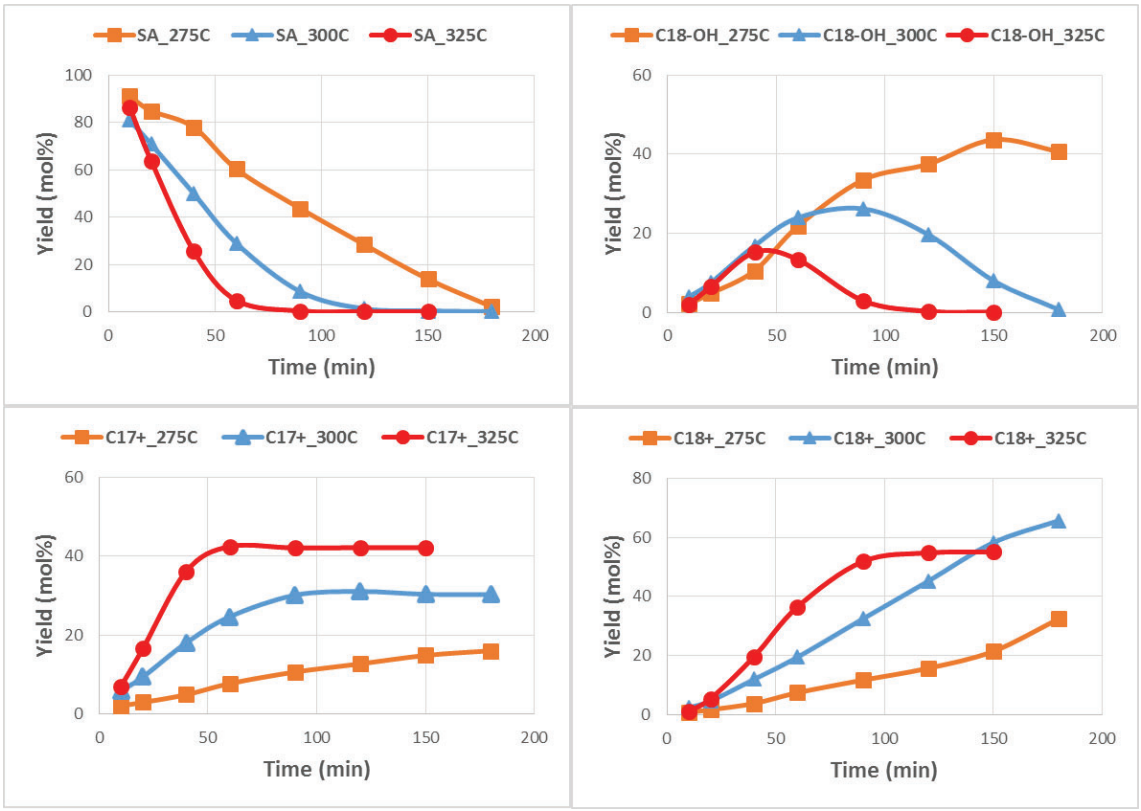

Fig 4.29 Temperature effect on HDO of stearic acid (SA) at hydrogen pressure 50 bar, feed 5 wt% SA, catalyst mass 0.4 g, stirring rate 1000 rpm. Symbols are experiments, curves indicate trends.

Fig 4.30 shows the results from experiments with varying hydrogen pressure (40-70 bar). It could be seen that the initial rate of decrease in yield of SA had a mild dependence on the H_2 pressure. However, it took approximately the same amount of time (120 mins) to achieve complete conversion of SA, irrespective of the H_2 pressure. However, as expected, higher pressure favored the direct-HDO rote since hydrogen is required at different steps along this route. Selectivity for the decarbonation route dropped from 38 to 23% while for the direct-HDO it increased from 58 to 73% as H_2 pressure varied from 40 to 70 bar.

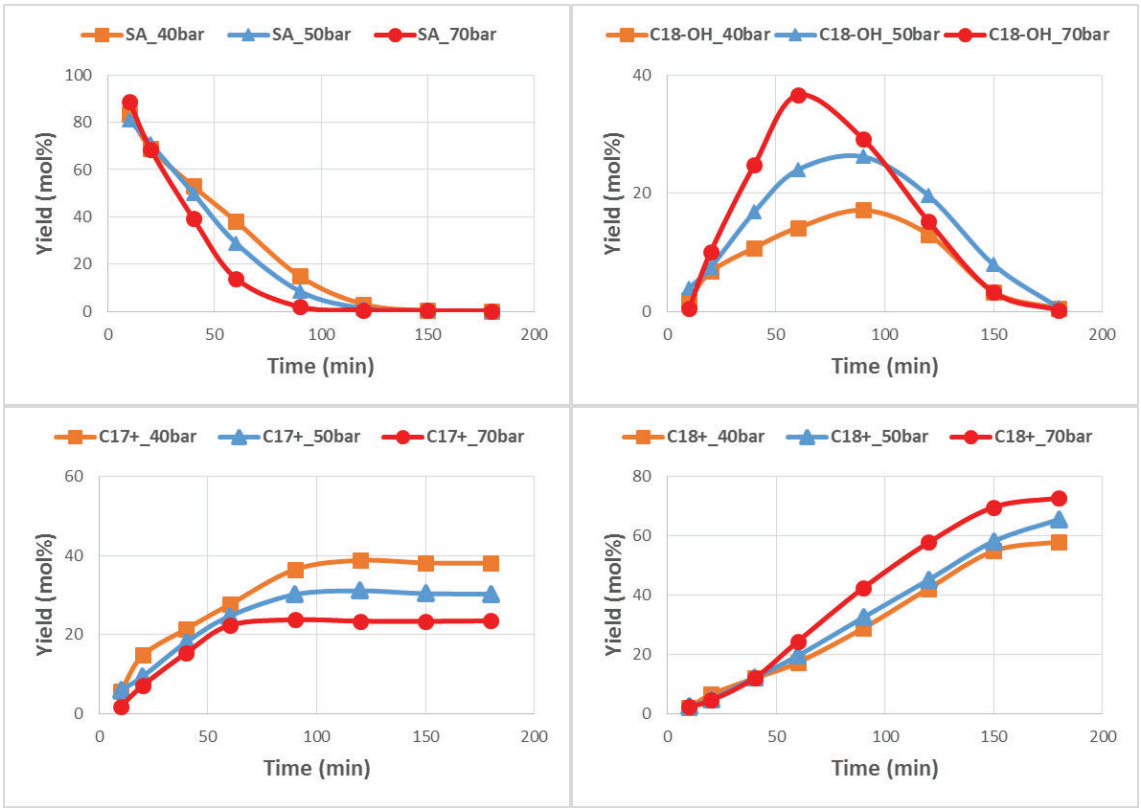

Fig 4.30 H_2 pressure effect on HDO of stearic acid (SA) at 300°C, feed 5 wt% SA, catalyst mass 0.4 g, stirring rate 1000 rpm. Symbols are experiments, curves indicate trends.

The effect of stirring rate in the range of 500-1000 rpm on HDO of SA has been showcased in Fig 4.31. There was not much difference in the products profiles for SA, C18-OH, C17+ and C18+ between 900 and 1000 rpm experiments. This suggests that the external mass limitations were absent at these high mixing rates. However, there were appreciable differences in the yield profile for the 500 rpm experiment. Octadecanol formed was much less (only 12%) when compared to higher stirring rates. This resulted in higher selectivity for C17+ products at lower stirring. It could be visualized that the transfer of hydrogen from gas to liquid to catalyst surface was restricted at low stirring rate (500 rpm). This resulted in low availability of hydrogen on catalyst surface, which therefore suppressed the direct-HDO route which requires more hydrogen per mole of fatty acid. It could be concluded that a stirring rate of c.a. 1000 rpm was sufficient to keep the liquid phase saturated with hydrogen throughout. It has been reported in the open literature that for similar reactor setups, stirring speeds of 1000 rpm or more are enough to avoid any limitations of external mass transfer for similar experimental conditions [16, 55].

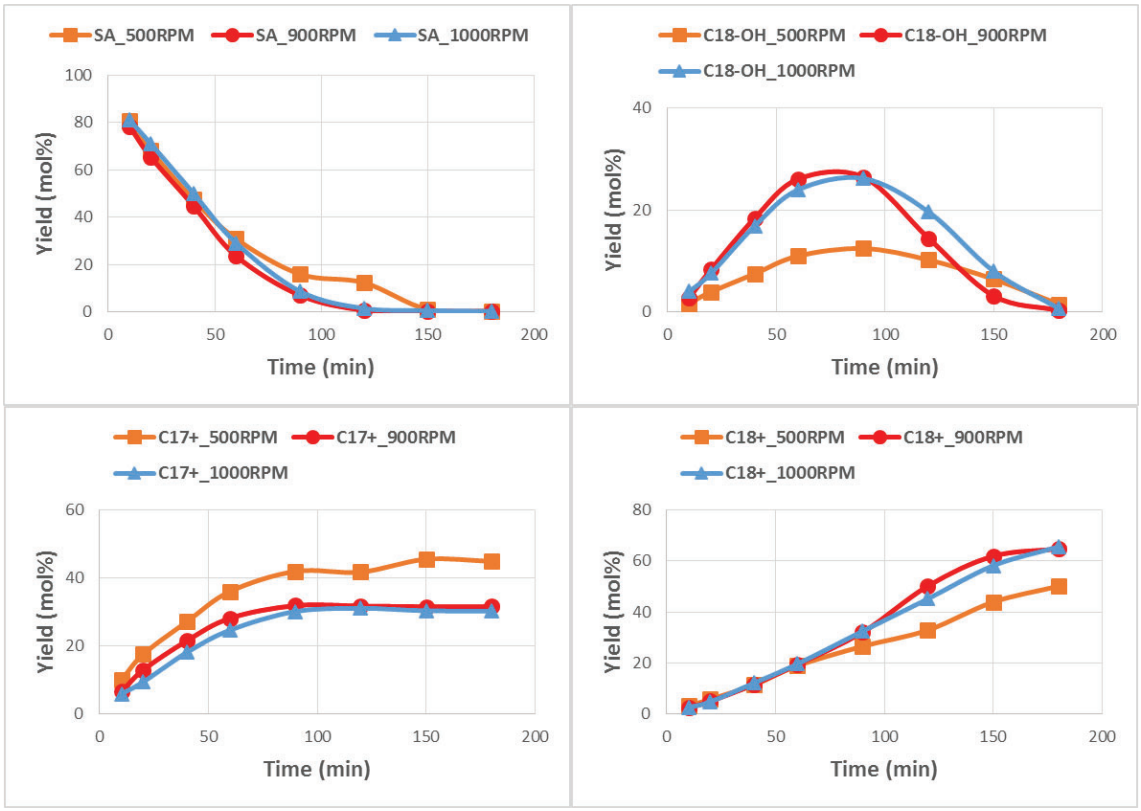

Fig 4.31 Stirring rate effect on HDO of stearic acid (SA) at 300°C, hydrogen pressure 50 bar, feed 5 wt% SA, catalyst mass 0.4 g. Symbols are experiments, curves indicate trends.

The influence of initial feed concentration during HDO of SA was tested for 2, 5 and 8 wt%. As shown in Fig 4.32, the rate of conversion of SA is higher at lower feed concentration. The concentration profile of SA indicates that the reaction with respect to SA is not first order, but instead less than unity. The duration to reach complete conversion was different for the 2, 5 and 8 wt% experiments. Initial feed concentration also had an influence on the selectivities of C17+ and C18+ products. The inhibiting effect of SA are illustrated in Fig 4.33. These results are from the baseline experiment with 5 wt% SA as feed, temperature 300°C hydrogen pressure 50 bar, catalyst mass 0.4 g, and stirring rate 1000 rpm. In Fig 4.33, products and intermediate yields are plotted against SA conversion. There is a rapid increase in the formation of C18+ products from 32 to 66% while C17+ products have plateaued at 30% at around 70% conversion. Also, there was a sudden increase in the conversion of the intermediate (C18-OH) once there was less SA remaining in the reaction mixture.

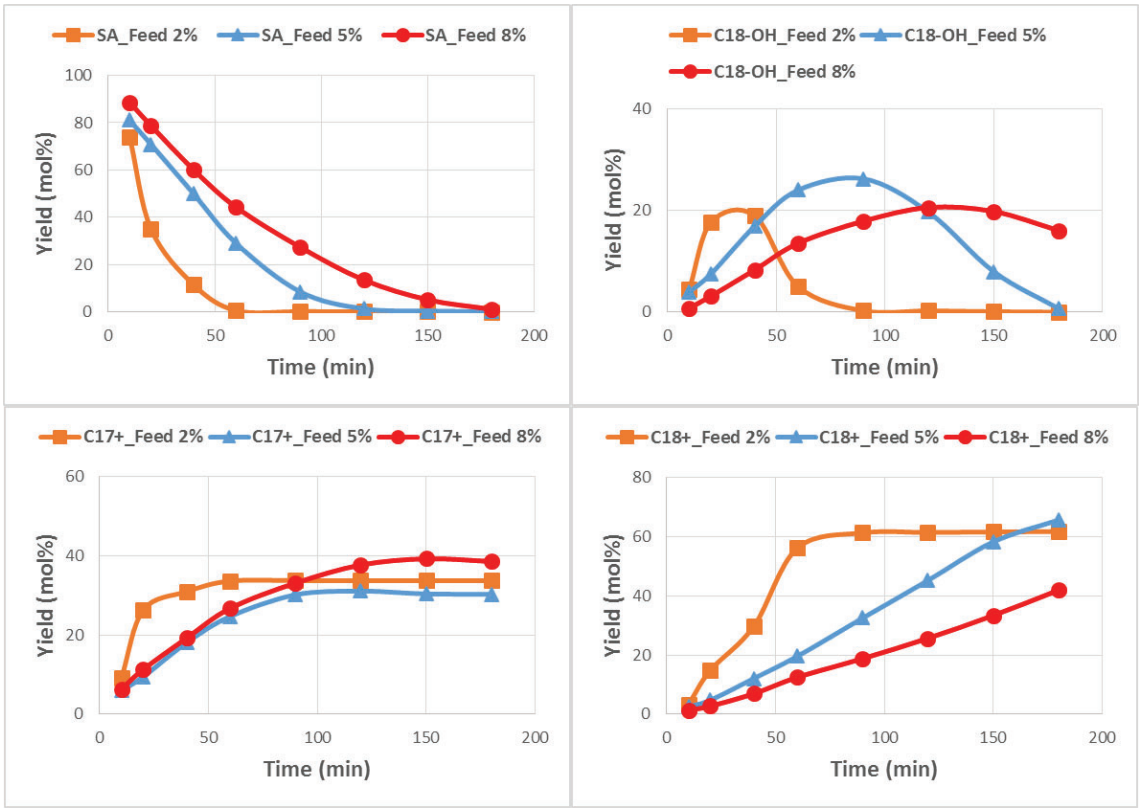

Fig 4.32 Initial feed conc. effect on HDO of stearic acid (SA) at 300°C, hydrogen pressure 50 bar, catalyst mass 0.4 g, and stirring rate 1000 rpm. Symbols are experiments, curves indicate trends.

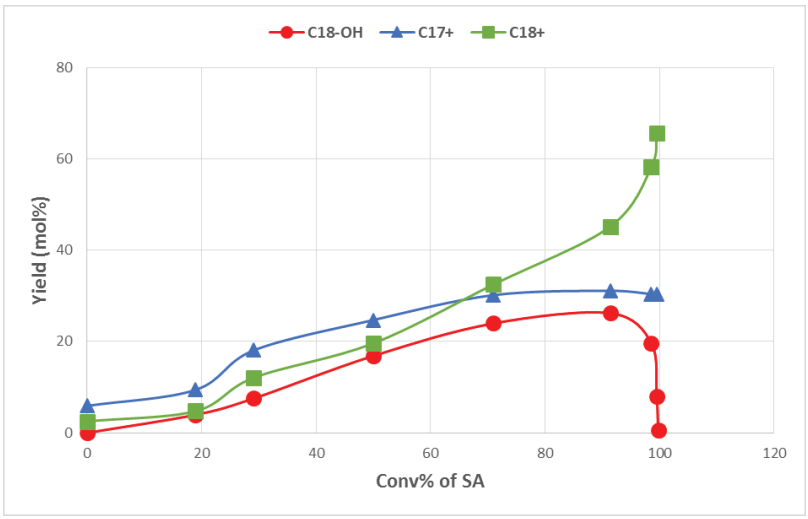

Fig 4.33 Baseline experiment- HDO of stearic acid (SA) at 300°C, hydrogen pressure 50 bar, catalyst mass 0.4 g, and stirring rate 1000 rpm. Symbols are experiments, curves indicate trends.

4.4.2 Kinetic modeling results

A kinetic model is developed to explain the reaction pathways for HDO of SA. The model was developed based on the results from experimental Section 4.2.1 above, and open literature [16, 20, 24, 40]. A simplified reaction scheme is proposed for HDO of SA for the kinetic model, see Scheme 4.1.

The five main reactions occurring on the NiMoS catalyst surface are –

Reaction 1: Conversion of SA to C18=O by reduction of carboxyl group;

Reaction 2: Decarboxylation of SA to C17+ hydrocarbon via removal of CO_2;

Reaction 3: Reduction of C18=O to C18-OH;

Reaction 4: Decarbonylation of C18=O to C17+; and

Reaction 5: Removal of water from C18-OH to yield C18+ hydrocarbons.

It should be noted that octadecanal, rather than the alcohol is considered as the main intermediate. It was observed in Section 4.2.1 that C18-OH is the intermediate when starting from C18=O feed and very little C18=O formed from C18-OH feed. Also, the saturation of double bonds in alkenes (both C17 and C18) have been lumped together since these hydrogenation reactions are quick and straight forward. Carbon oxides would be released from the decarbonation reaction. Additionally, side reactions like water gas shift (WGS) and methanation would contribute to the distribution of CO, CO_2 and CH_4 in the gas phase. WGS and methanation reactions were initially included in the kinetic model but the predictions from the model for the gas phase were found to be poor. This could be explained due to the fact that the solubility of CO_2 in liquid phase is much larger than other two gases as per the liquid-vapor equilibrium predicted by the EOS.

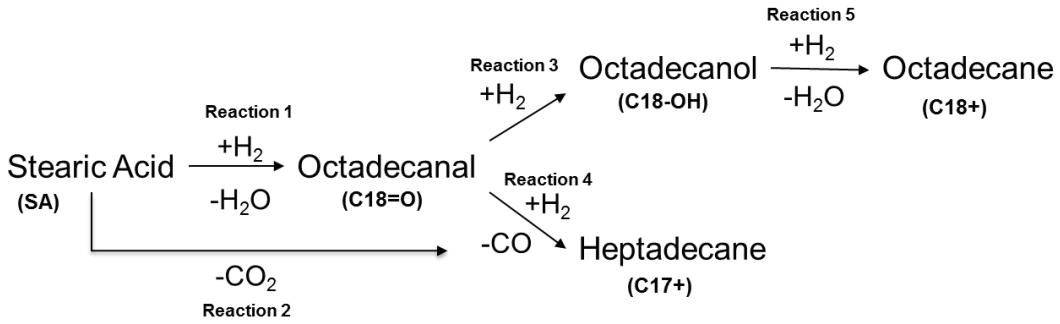

Scheme 4.1 Simplified reaction scheme for kinetic model.

4.4.2.a Kinetic rate expressions

Table 4.12, presents the Langmuir-Hinshelwood (LH) type rate expressions for the reactions mentioned in Scheme 1. The denominator of the rate expressions includes an inhibition term due to SA. This inhibition is in accordance with a few experimental studies in the literature which suggest that species containing a carboxylic group inhibit the HDO reactions [29, 40, 56]. This seems to be validated by our results as discussed in Section 4.4.2 above regarding Fig 4.33. In the given model it was assumed that there is only one site for all reactions to occur. Thus, the inhibition term for SA was included in all rate expressions. This inhibition term was found to be very important to allow the rate of reaction for C18-OH to increase as less SA remained in the reaction mixture and thus a better agreement between modeling and experimental results could be achieved. The SA inhibition term permitted the effective order of the reaction with respect to SA to be less than unity in Scheme 1 for reactions 1 and 2. This is also in agreement with the results presented in experimental Section 4.2.1 and as shown in Fig 4.33. Donnis et. al.[20] validated the

tautomerism step during HDO of similar molecules. This equilibrium term was included for the direct-HDO route in the rate expressions.

Table 4.12 Reaction scheme and rate expressions.

	Reaction	Rate expression
r1	$C_{18}H_{36}O_2 + H_2 \rightarrow C_{18}H_{36}O + H_2O$	$r_1 = \frac{k_1 C_{SA} C_{H2}}{(1 + K_{SA} C_{SA})}$
r2	Decarboxylation $C_{18}H_{36}O_2 \rightarrow C_{17}H_{36} + CO_2$	$r_2 = \frac{k_2 C_{SA}}{(1 + K_{SA} C_{SA})}$
r3	Direct-HDO $C_{18}H_{36}O + H_2 \rightarrow C_{18}H_{37}OH$	$r_3 = \frac{k_3 C_{C18=O} C_{H2}}{(1 + K_{SA} C_{SA})}\left(1 - \frac{a_{C18OH}}{a_{C18=O} a_{H2} K_{eq}}\right)$
r4	Decarbonylation $C_{18}H_{36}O \rightarrow C_{17}H_{36} + CO$	$r_4 = \frac{k_4 C_{C18=O}}{(1 + K_{SA} C_{SA})}$
r5	$C_{18}H_{37}OH + H_2 \rightarrow C_{18}H_{38} + H_2O$	$r_5 = \frac{k_5 C_{C18OH}}{(1 + K_{SA} C_{SA})}$

4.4.2.b Parameter estimations and simulation results

Table 4.13, presents the rate and adsorption equilibrium constants for the reactions and their respective activation energies. The reaction rate constants were calculated using all experiments at the baseline temperature of 300 °C, whereas activation energies were calculated based on the deviations at the higher and lower temperatures. The range of the confidence intervals (95%) depicts the accuracy of assessment. In Table 4.13, it could be seen that the confidence intervals are relatively high for rate constants of reaction 2 and 4 and the activation energy for reaction 4. This could be likely due to the fact that both these reactions led to the formation of products C17+ via decarboxylation and decarbonylation route, and thus their kinetic parameters are correlated. These two routes have been distinguished only at one temperature i.e. 275 °C based on the difference in selectivity from the experiments with SA and C18=O as feed. Similarly reactions 1 and 2 are related as both are involved in the conversion of SA. So again, correlation likely explains why the confidence interval for the activation energy of reaction 1 is high. A comparison of experimental and modeling results has been shown in Fig 4.34-4.37. The continuous lines correspond to the results from the simulations while symbols represent the experimental data. There is a good agreement between the modeling and experimental results in the given range of reaction conditions (temperature 275-325 °C, pressure 40-70 bar hydrogen, feed concentration 2-8 wt%) tested. For instance, the model predicted faster conversion of SA at higher temperature of 325 °C compared to 275 °C as shown in Fig 4.34. The increase in selectivity for C17+ products with increased temperature was also well-predicted by the model. In Fig 4.34a and 4.35, the experiments with varying pressure are depicted. It could be seen that there is a good agreement between the experiment and simulation results with respect to change in selectivity with increase in pressure. The model is able to predict that direct-HDO route is preferred at higher hydrogen pressure. This is in accordance with the reaction scheme where the direct-HDO reaction (reaction 3 in Table 4.12) is dependent on H_2 concentration, whereas the competing decarbonylation (reaction 4) and the decarboxylation (reaction 2) are independent of H_2 concentration. Also, the slower rate of conversion of SA with increasing initial feed concentration was consistent with the experimental data in Fig 4.34a and 4.36. The inhibition term included in the rate expressions for

SA mentioned in the above section facilitates this good agreement. The developed model also predicted the change in concentration profiles when octadecanol and octadecanal feed were employed (see Fig 4.37). The model closely predicts that direct-HDO is by far the most favored route when C18-OH is used. This is due to the fact that the C18-OH is an intermediate of only the direct-HDO pathway according to the model reaction scheme (Scheme 1). Similarly, the rapid conversion of C18=O was consistent with the experimental data in Fig 4.37a which is due to the high reactivity of aldehyde species.

Table 4.13 Kinetic parameter values and 95% confidence intervals.

Rate and adsorption equilibrium constants (units) at 300°C	Value ± Confidence interval	Activation energies (kJ mol^{-1})	Value ± Confidence interval
k_1 (m^6 mol^{-1} kg^{-1} s^{-1})	$5.52\pm1.16\times10^{-5}$	E_1	22.3±17.3
k_2 (m^3 kg^{-1} s^{-1})	$8.63\pm1.96\times10^{-3}$	E_2	119±30.2
k_3 (m^6 mol^{-1} kg^{-1} s^{-1})	$2.78\pm0.53\times10^{-3}$	E_3	159±31.8
k_4 (m^3 kg^{-1} s^{-1})	$4.72\pm2.26\times10^{-2}$	E_4	90.7±80.4
k_5 (m^3 kg^{-1} s^{-1})	$2.70\pm0.34\times10^{-2}$	E_5	117±20.8
K_{SA} (m^3 mol^{-1})	$5.14\pm1.34\times10^{-2}$		

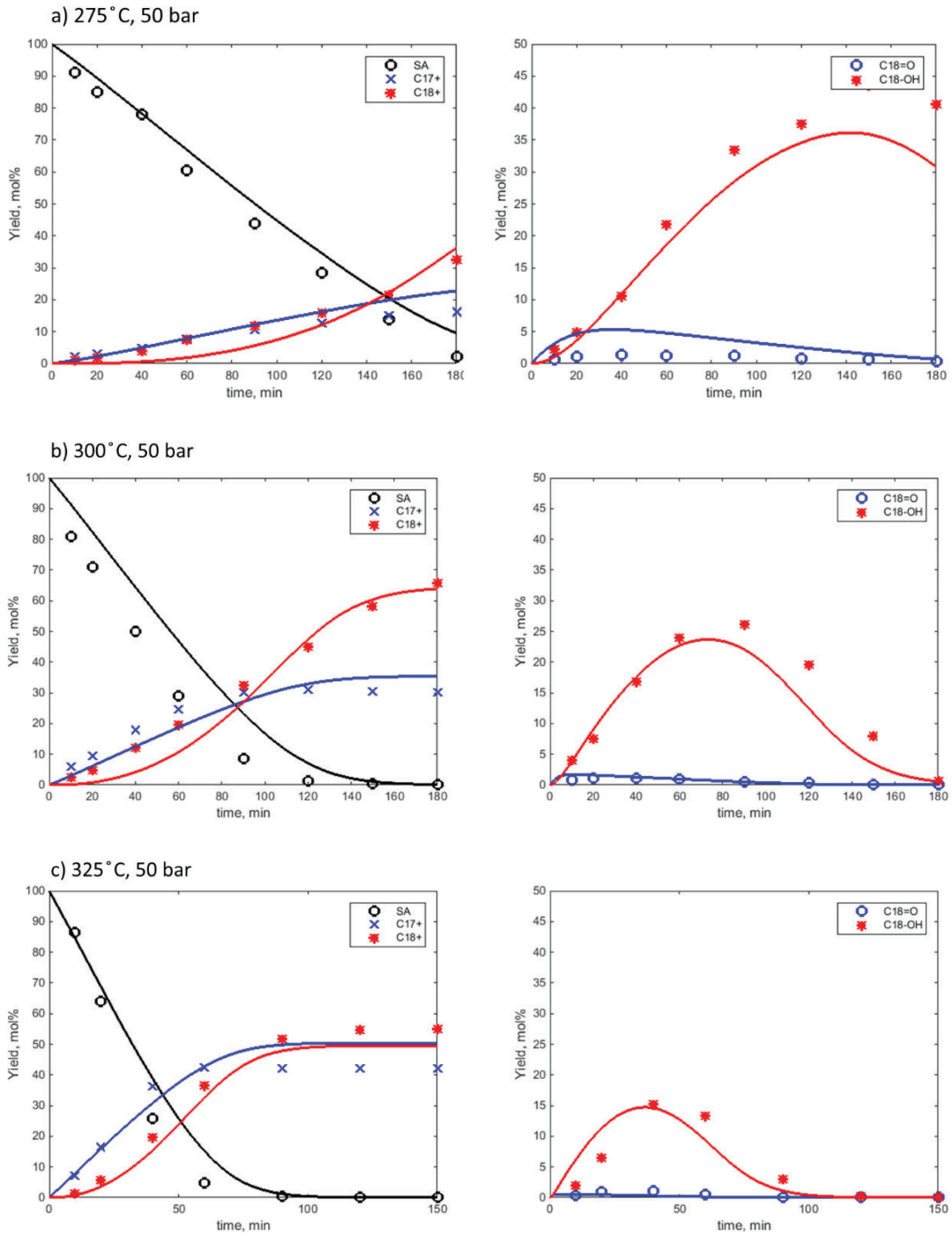

Fig 4.34 Comparison of experimental and modeled results for varying temperature: (a) 275 °C, (b) 300 °C, (c) 325 °C with hydrogen pressure 50 bar, feed 5 wt% SA, catalyst mass 0.4 g and stirring speed 1000 rpm. Symbols are experiments, curves are model predictions.

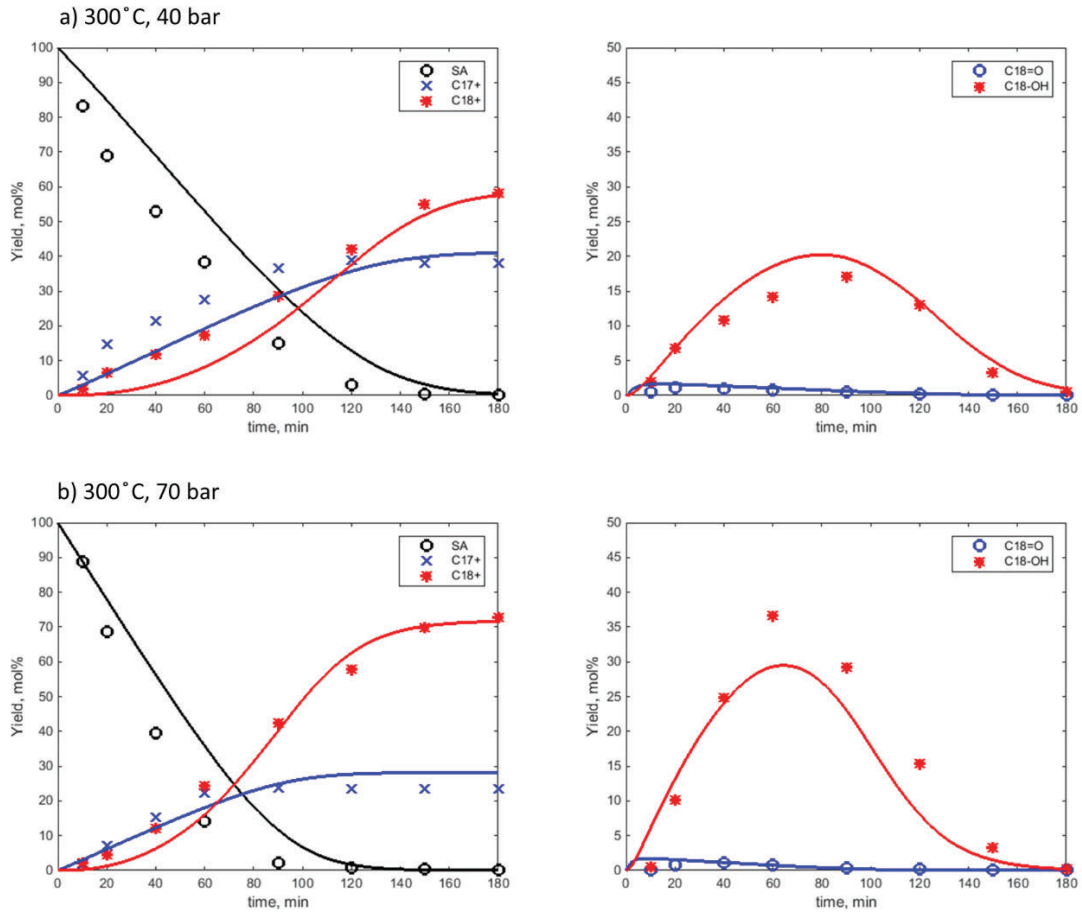

Fig 4.35 Comparison of experimental and modeled results for varying hydrogen pressure: (a) 40 bar, (b) 70 bar with temperature 300 °C, feed 5 wt% SA, catalyst mass 0.4 g and stirring speed 1000 rpm. Symbols are experiments, curves are model predictions.

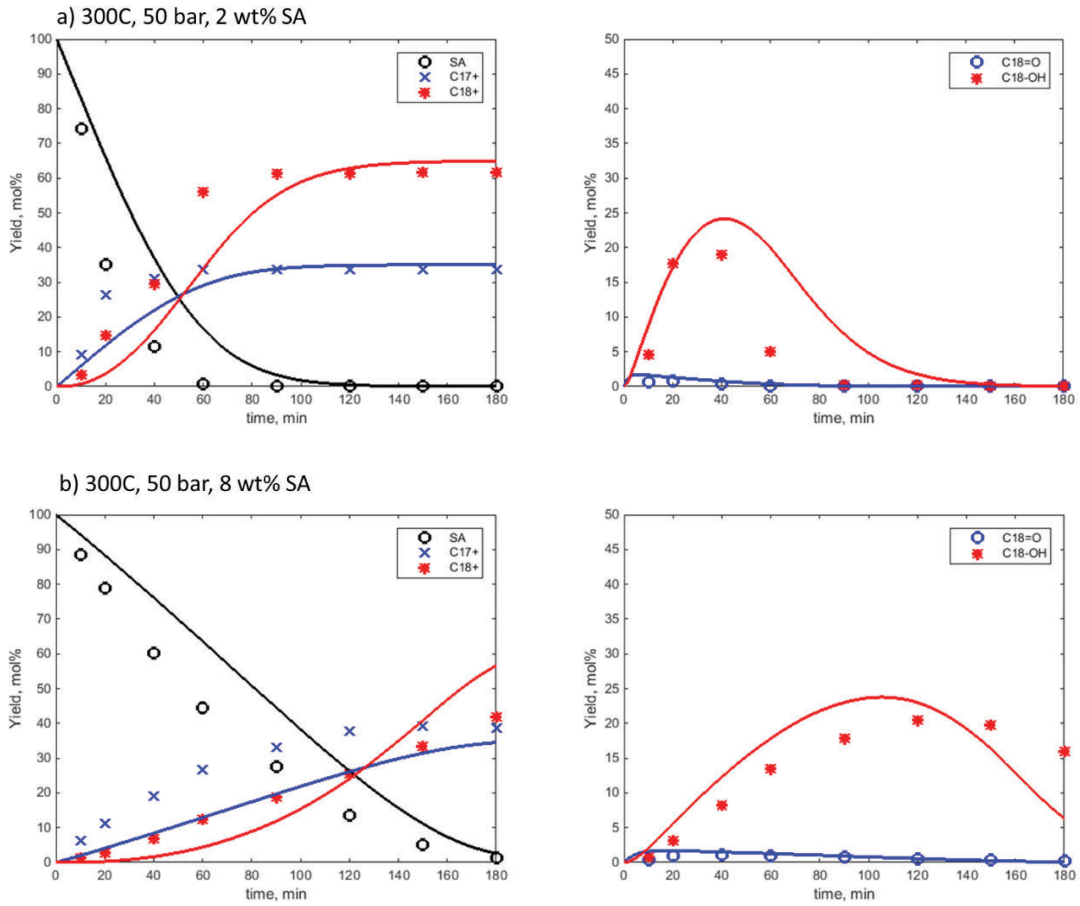

Fig 4.36 Comparison of experimental and modeled results for varying feed concentration: (a) 2 wt% SA, (b) 8 wt% SA with temperature 300 °C, hydrogen pressure 50 bar, catalyst mass 0.4 g and stirring speed 1000 rpm. Symbols are experiments, curves are model predictions.

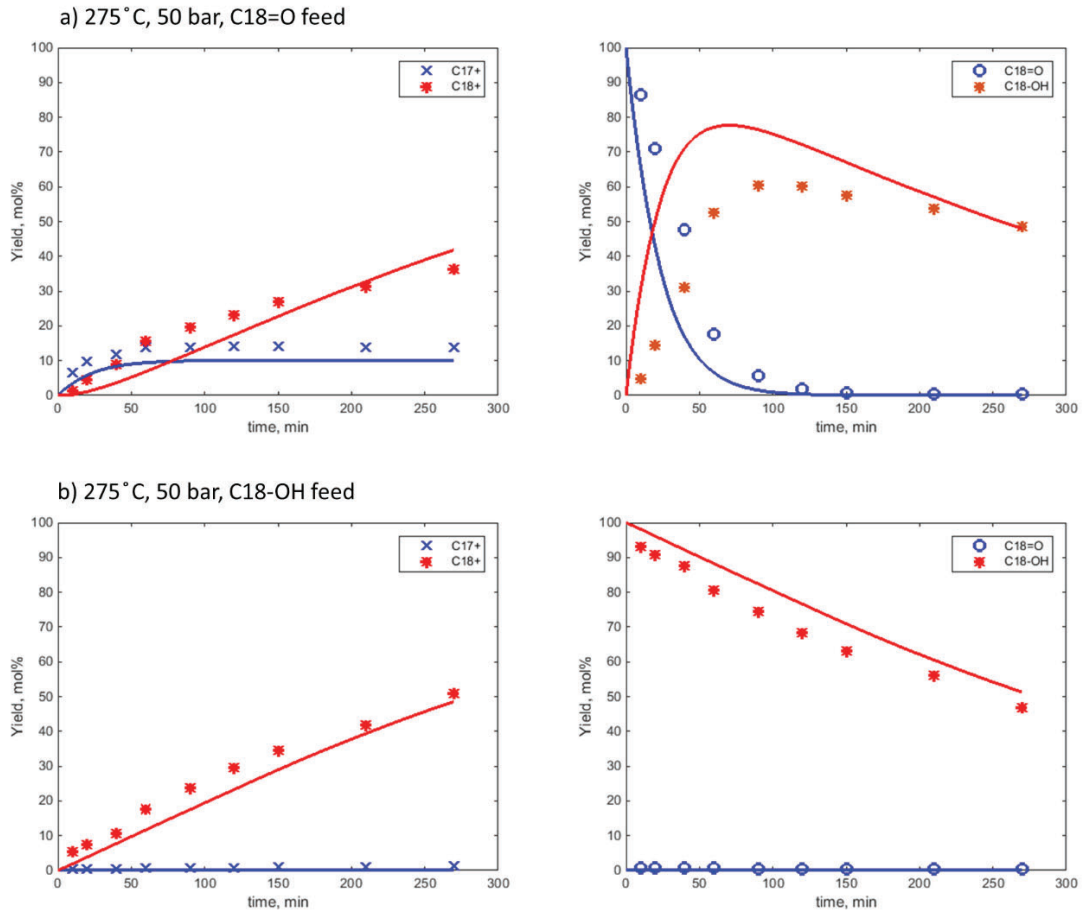

Fig 4.37 Comparison of experimental and modeled results for varying feed component: a) 5 wt% C18=O, b) 5 wt% C18-OH with temperature 275 °C, hydrogen pressure 50 bar, catalyst mass 0.04 g and stirring speed 1000 rpm. Symbols are experiments, curves are model predictions.

5 Conclusions and Outlook

5.1 Concluding Remarks

To combat the climate crisis a range of sustainable solutions must be developed and adapted. Advanced biofuels have the potential to bring down the GHG emissions from the transport sector substantially. Hydrodeoxygenation is at the core of the processes in refineries to produce biofuels which employ typical hydrotreating (TMS) catalysts. Renewable feedstocks like tall oil, algal oil, used cooking oil etc. contain different impurities like iron complexes (Fe), phospholipids (P) and alkali metals (Na, K etc.) which can accelerate the deactivation of the catalyst. Knowledge regarding catalyst deactivation and reaction kinetics was developed in this thesis through experiments and kinetic modeling.

This thesis includes studies on the deactivation of sulfided NiMo catalysts due to iron species (Paper I), catalyst deactivation due to phosphorus from phospholipids (Paper II), comparisons of the role of different key poisons identified from analysis of spent catalysts from a refinery (Paper III) and kinetic modeling of hydrodeoxygenation (HDO) of stearic acid (Paper IV).

The deactivation of molybdenum based catalysts (MoS_2 and NiMoS) supported on alumina was investigated over a range of concentrations of Fe during HDO of oleic acid. Renewable feeds are known to have higher total acid numbers (TAN) which could cause corrosion during storage and transportation in iron vessels to yield iron salts. Iron oleate complex was used as the poison and added together with the feed and solvent to the batch reactor. This Fe poison had a negative impact on the activity for both unpromoted and promoted catalysts. The conversion of oxygenates slowed down which would not be a desirable scenario in a refining process. Another interesting finding was the change in selectivities for these catalyst systems. C17 hydrocarbons were the major product when NiMoS was employed while for MoS_2, selectivity for C18 hydrocarbons was greater. But, in the presence of Fe poison, the selectivity for direct-HDO increased for NiMoS while with MoS_2 there was an increase in the selectivity for the decarbonation route. Spent catalysts were characterized to elucidate reasons behind the observed changes in activity and selectivity. BET results suggest a significant drop in the pore volume which explains the decrease in activity up to a certain extent. The carbon content in recovered catalysts independent of amount of iron added which suggest that iron didn't promote coking as such. A loss of active sulfide phase was also ruled out since the sulfur content of the spent catalyst did not indicate much loss of sulfur or relation to Fe addition. The results from temperature programmed reaction with hydrogen indicated a loss of labile sulfur instead. This was concluded by the ability to react with hydrogen

to produce H_2S for a baseline and a poisoned catalyst sample. TEM-EDX imaging resulted in information of relative distribution of Fe with respect to Ni and Mo. It was found that Fe preferentially deposits around Ni which illustrates the reduced activity and lower selectivity for the C17 products which otherwise is a preferred reaction route with the NiMoS system. On the other hand, for the MoS_2 catalyst, the Fe species would have caused poisoning of active sites and may have formed the less active FeMo phase which explains the drop in activity and switch in the selectivity from direct-HDO to decarbonation.

The catalyst deactivation of NiMo supported on alumina was studied during HDO of oleic acid due to phospholipid molecules. Bio/algal oils are known to contain phospholipids like phosphatidylcholine (PC), which was employed as a model compound to represent poison in this study. It was found that the hydrogenation and hydrogenolysis activity of the catalyst reduced due to the presence of PC. The decarbonation route was affected more than the direct-HDO route and the decrease in C17 selectivity was proportional to the amount of PC in the feed. The loss of sulfur as the cause of deactivation was ruled out as the sulfur amount was in a similar range in spent catalysts. A correlation between refractory coke (high C/H ratio) formation to the PC concentration was established based on the TPO of spent catalysts. Nitrogen physisorption of the spent catalyst suggested severe pore blockage even at the lower concentrations of PC in the feed. The distribution of phosphorus was found to be uniform over the alumina support based on the TEM-EDX results. It seems that the phosphorus on the support resulted in a reduced distribution of MoS_2 slabs and affected the Ni promotion. XPS results confirmed the phosphorus interacted with the support to form aluminum phosphate ($AlPO_4$), which blocks the active sites and pores, leading to the observed catalyst deactivation.

The effect of catalyst poisons present in bio-based feedstocks has been investigated on the hydrodeoxygenation activity of NiMo catalysts. A batch of $NiMo/Al_2O_3$ model catalyst was prepared by an impregnation method and placed in a refinery unit for biofuel (HVO) production for several months. The spent catalysts recovered from the refinery was analyzed via ICP, elemental analysis and SEM-EDX. These analyses suggested the key contaminants found on the catalyst were Fe, P and alkali metals in addition to coke. Also, these poisons were mostly deposited near the catalyst particle surface. Two treatment methods were explored to revive the catalyst activity – calcination and Soxhlet extraction. Calcination was found to be an effective method compared to Soxhlet extraction. Then, a set of lab scale experiments were performed to study the role of poisons (iron stearate (Fe), potassium nitrate (K) and phospholipid (P/Na)) during hydrodeoxygenation of stearic acid over NiMo catalysts. All three poisons caused a significant drop in catalytic activity with an increase in poison concentration. Fe had the largest impact at low concentrations. In the case of K, the catalyst deactivation was prominent at higher concentrations. BET analysis suggested that the surface area, pore volume and pore distribution was affected, where phospholipid caused the largest reduction. It was found that the poison elements were in the given oxidation states of P(+5), K(+1) and Fe(+3) from XPS analysis. SEM-EDX analysis provided insights into the elemental distribution of elements along the radial axis which indicated that Fe and P deposited near the surface while K penetrated deeper into the catalyst particles.

The reaction scheme for hydrodeoxygenation (HDO) of SA over a NiMo catalyst has been explored in detail by employing Stearic acid (SA), Octadecanal (C18=O) and Octadecanol (C18-OH) as feed components. It was proposed that the aldehyde is the common intermediate for both

decarbonation and direct-HDO routes, however alcohol was intermediate for only the direct HDO-route based on the experimental results. Several experiments were carried over a range of temperature (275-325 °C), pressure (40-70 bar hydrogen), feed concentration (2-8 wt%) and stirring rate (500-1000 rpm). On the basis of a simplified reaction scheme for HDO of SA, a kinetic model was developed. An inhibition term due to stearic acid was included in the kinetic rate expressions. The experimentally observed rates of conversions and variations in selectivity for varying temperatures, hydrogen pressure and feed concentrations were well reproduced by the kinetic model. The reaction scheme and contribution of the competing rates of decarboxylation and decarbonylation to produce C17 products were distinguished by experiments with feed of intermediate species (C18=O and C18-OH).

5.2 Outlook

The variation in renewable feedstocks is more than the fossil feedstocks in terms of oxygen (heteroatoms) content, types of molecules (functional groups) and contaminants. Also, catalyst deactivation is inevitable for most processes, however its rate at which it happens varies to a great extent. All these factors make it a complex subject to study. Based on our studies, the Fe, P and alkali metals are the most common impurities which were found on the spent catalysts. However, it would be worth investigating other contaminants present in renewable feedstocks. It was realized that phospholipids could be detrimental to the textural properties of the catalyst and phosphorus is one of the contaminants which is omnipresent in all feedstocks of bio-origin. Further work should be aimed to explore the effect of phospholipids on different aspects of catalyst deactivation to develop deeper knowledge on deactivation mechanisms. For example spectroscopic techniques like Raman or IR spectroscopy on adsorbed CO can highlight the nature of carbonaceous species or interaction of poison element with catalyst surface. We found how the iron affects the creation of sulfur vacancies by comparing fresh and spent catalysts via temperature-programmed reaction with hydrogen. Moreover, a detailed adsorption study using probe molecules like CO or NO, could be carried out to further understand how these poisons interact with the active metal phase or alumina to influence the catalytic activity and stability. It could lead to interesting insights regarding how poisons affect the quantity or type of active sites and how much fraction of actives sites were blocked on spent catalysts related to poison concentration. It was found that the amount of poison deposited on catalyst varied. Thus, it would be very interesting from an application point of view to develop specific guard beds for renewable feeds. The catalyst pore structure and size range would need to be tuned to maximize the trapping of impurities present in renewable oils. In our studies, a batch reactor set-up was employed with experiments with a duration of 4-6 h, so the concentration of poison added to the feed was relatively high to observe their impact in this limited period. It may provide further insights if we can evaluate catalysts for deactivation due to these contaminants in a continuous reactor system and with longer time-on-stream. More specifically one could with a continuous reactor examine the distribution of poisons axially long the length of the bed. This can also be useful since for a favorable guard bed material, poisons should be highly concentrated to a limited zone in the front of the bed.

6 References

[1] BP Energy Outlook 2019.
[2] S. Díaz, J. Settele, E. Brondízio, H. Ngo, M. Guèze, J. Agard, A. Arneth, P. Balvanera, K. Brauman, S. Butchart, Summary for policymakers of the global assessment report on biodiversity and ecosystem services of the Intergovernmental Science-Policy Platform on Biodiversity and Ecosystem Services, (2019).
[3] C. Le Quéré, R.M. Andrew, P. Friedlingstein, S. Sitch, J. Hauck, J. Pongratz, P.A. Pickers, J.I. Korsbakken, G.P. Peters, J.G. Canadell, Global carbon budget 2018, Earth System Science Data (Online), 10 (2018).
[4] D. Dunn, US Energy Information Administration Monthly Energy Review, August, 2016.
[5] U.S. Energy Information Administration (EIA) Monthly Energy Review (accessed July 2019).
[6] HYBRIT – Towards fossil-free steel http://www.hybritdevelopment.com/hybrit-toward-fossil-free-steel (accessed July 2019).
[7] Global Energy Perspective 2019 McKinsey.
[8] A.E. Outlook, With Projections to 2050 (US Energy Information Administration, 2017), 2017.
[9] International Energy Outlook 2017 (accessed July 2019).
[10] T.L. Marker, L.G. Felix, M.B. Linck, M.J. Roberts, Integrated hydropyrolysis and hydroconversion (IH2) for the direct production of gasoline and diesel fuels or blending components from biomass, part 1: Proof of principle testing, Environmental Progress & Sustainable Energy, 31 (2012) 191-199.
[11] R. Tiwari, B.S. Rana, R. Kumar, D. Verma, R. Kumar, R.K. Joshi, M.O. Garg, A.K. Sinha, Hydrotreating and hydrocracking catalysts for processing of waste soya-oil and refinery-oil mixtures, Catalysis Communications, 12 (2011) 559-562.
[12] H. Aatola, M. Larmi, T. Sarjovaara, S. Mikkonen, Hydrotreated Vegetable Oil (HVO) as a Renewable Diesel Fuel: Trade-off between NOx, Particulate Emission, and Fuel Consumption of a Heavy Duty Engine, SAE International Journal of Engines, 1 (2008) 1251-1262.
[13] S. Eijsbouts, L.C.A. van den Oetelaar, J.N. Louwen, R.R. van Puijenbroek, G.C. van Leerdam, Changes of MoS2 Morphology and the Degree of Co Segregation during the Sulfidation and Deactivation of Commercial Co−Mo/Al2O3 Hydroprocessing Catalysts, Industrial & Engineering Chemistry Research, 46 (2007) 3945-3954.
[14] S.L.a.A.R. B Flach, EU Biofuels Annual 2017.

[15] P. Arora, H. Ojagh, J. Woo, E. Lind Grennfelt, L. Olsson, D. Creaser, Investigating the effect of Fe as a poison for catalytic HDO over sulfided NiMo alumina catalysts, Applied Catalysis B: Environmental, 227 (2018) 240-251.
[16] E. Commision, The Commission calls for a climate neutral Europe by 2050 (accessed July 2019).
[17] M.o.t. Environment, Sweden positive on EU long-term climate strategy (accessed July 2019).
[18] The climate policy framework - Ministry of the Environment https://www.government.se/articles/2017/06/the-climate-policy-framework/ (accessed July 2019).
[19] P.J. Kooyman, J.A. Rob van Veen, The detrimental effect of exposure to air on supported MoS2, Catalysis Today, 130 (2008) 135-138.
[20] Territoriella utsläpp och upptag av växthusgaser - Swedish Environmental Protection Agency http://www.naturvardsverket.se/klimatutslapp?# (accessed July 2019).
[21] Energy in Sweden 2019, Energimyndigheten https://www.energimyndigheten.se/statistik/ (accessed July 2019).
[22] Energy for transport Eurostat https://ec.europa.eu/eurostat/web/products-eurostat-news/-/DDN-20190222-1 (accessed July 2019).
[23] P. Forzatti, L. Lietti, Catalyst deactivation, Catalysis Today, 52 (1999) 165-181.
[24] E. Furimsky, Catalytic hydrodeoxygenation, Applied Catalysis A: General, 199 (2000) 147-190.
[25] P.M. Mortensen, D. Gardini, C.D. Damsgaard, J.-D. Grunwaldt, P.A. Jensen, J.B. Wagner, A.D. Jensen, Deactivation of Ni-MoS2 by bio-oil impurities during hydrodeoxygenation of phenol and octanol, Applied Catalysis A: General, 523 (2016) 159-170.
[26] D. Kubička, J. Horáček, Deactivation of HDS catalysts in deoxygenation of vegetable oils, Applied Catalysis A: General, 394 (2011) 9-17.
[27] B. Donnis, R.G. Egeberg, P. Blom, K.G. Knudsen, Hydroprocessing of Bio-Oils and Oxygenates to Hydrocarbons. Understanding the Reaction Routes, Topics in Catalysis, 52 (2009) 229-240.
[28] S.-J. Lee, S. Go, G.-T. Jeong, S.-K. Kim, Oil production from five marine microalgae for the production of biodiesel, Biotechnology and Bioprocess Engineering, 16 (2011) 561-566.
[29] A. Kumar, S. Sharma, Potential non-edible oil resources as biodiesel feedstock: An Indian perspective, Renewable and Sustainable Energy Reviews, 15 (2011) 1791-1800.
[30] J.M. Anthonykutty, K.M. Van Geem, R. De Bruycker, J. Linnekoski, A. Laitinen, J. Räsänen, A. Harlin, J. Lehtonen, Value Added Hydrocarbons from Distilled Tall Oil via Hydrotreating over a Commercial NiMo Catalyst, Industrial & Engineering Chemistry Research, 52 (2013) 10114-10125.
[31] O.İ. Şenol, E.M. Ryymin, T.R. Viljava, A.O.I. Krause, Reactions of methyl heptanoate hydrodeoxygenation on sulphided catalysts, Journal of Molecular Catalysis A: Chemical, 268 (2007) 1-8.
[32] S. Brillouet, E. Baltag, S. Brunet, F. Richard, Deoxygenation of decanoic acid and its main intermediates over unpromoted and promoted sulfided catalysts, Applied Catalysis B: Environmental, 148–149 (2014) 201-211.
[33] P.M. Mortensen, J.D. Grunwaldt, P.A. Jensen, K.G. Knudsen, A.D. Jensen, A review of catalytic upgrading of bio-oil to engine fuels, Applied Catalysis A: General, 407 (2011) 1-19.

[34] C. Dupont, R. Lemeur, A. Daudin, P. Raybaud, Hydrodeoxygenation pathways catalyzed by MoS2 and NiMoS active phases: A DFT study, Journal of Catalysis, 279 (2011) 276-286.
[35] D.W.S. Wayne K. Craig, Production of hydrocarbons with a relatively high cetane rating, 1988.
[36] E. Laurent, B. Delmon, Study of the hydrodeoxygenation of carbonyl, car□ylic and guaiacyl groups over sulfided CoMo/γ-Al2O3 and NiMo/γ-Al2O3 catalysts: I. Catalytic reaction schemes, Applied Catalysis A: General, 109 (1994) 77-96.
[37] D. Kubička, L. Kaluža, Deoxygenation of vegetable oils over sulfided Ni, Mo and NiMo catalysts, Applied Catalysis A: General, 372 (2010) 199-208.
[38] H. Topsøe, B.S. Clausen, F.E. Massoth, Hydrotreating Catalysis, in: J.R. Anderson, M. Boudart (Eds.) Catalysis: Science and Technology, Springer Berlin Heidelberg, Berlin, Heidelberg, 1996, pp. 1-269.
[39] H. Zhang, H. Lin, Y. Zheng, The role of cobalt and nickel in deoxygenation of vegetable oils, Applied Catalysis B: Environmental, 160–161 (2014) 415-422.
[40] M. Snåre, I. Kubičková, P. Mäki-Arvela, K. Eränen, D.Y. Murzin, Heterogeneous Catalytic Deoxygenation of Stearic Acid for Production of Biodiesel, Industrial & Engineering Chemistry Research, 45 (2006) 5708-5715.
[41] B. Peng, Y. Yao, C. Zhao, J.A. Lercher, Towards Quantitative Conversion of Microalgae Oil to Diesel-Range Alkanes with Bifunctional Catalysts, Angewandte Chemie International Edition, 51 (2012) 2072-2075.
[42] K. Sun, A.R. Wilson, S.T. Thompson, H.H. Lamb, Catalytic Deoxygenation of Octanoic Acid over Supported Palladium: Effects of Particle Size and Alloying with Gold, ACS Catalysis, 5 (2015) 1939-1948.
[43] O.İ. Şenol, E.M. Ryymin, T.R. Viljava, A.O.I. Krause, Effect of hydrogen sulphide on the hydrodeoxygenation of aromatic and aliphatic oxygenates on sulphided catalysts, Journal of Molecular Catalysis A: Chemical, 277 (2007) 107-112.
[44] O.İ. Şenol, T.R. Viljava, A.O.I. Krause, Effect of sulphiding agents on the hydrodeoxygenation of aliphatic esters on sulphided catalysts, Applied Catalysis A: General, 326 (2007) 236-244.
[45] E.-M. Ryymin, M.L. Honkela, T.-R. Viljava, A.O.I. Krause, Insight to sulfur species in the hydrodeoxygenation of aliphatic esters over sulfided NiMo/γ-Al2O3 catalyst, Applied Catalysis A: General, 358 (2009) 42-48.
[46] E. Laurent, B. Delmon, Study of the hydrodeoxygenation of carbonyl, carboxylic and guaiacyl groups over sulfided CoMo/γ-Al2O3 and NiMo/γ-Al2O3 catalyst: II. Influence of water, ammonia and hydrogen sulfide, Applied Catalysis A: General, 109 (1994) 97-115.
[47] E. Laurent, B. Delmon, Study of the hydrodeoxygenation of carbonyl, car□ylic and guaiacyl groups over sulfided CoMo/γ-Al2O3 and NiMo/γ-Al2O3 catalyst: II. Influence of water, ammonia and hydrogen sulfide, Applied Catalysis A: General, 109 (1994) 97-115.
[48] D. Kubička, J. Horáček, Deactivation of HDS catalysts in deoxygenation of vegetable oils, Applied Catalysis A: General, 394 (2011) 9-17.
[49] A.E. Coumans, E.J.M. Hensen, A model compound (methyl oleate, oleic acid, triolein) study of triglycerides hydrodeoxygenation over alumina-supported NiMo sulfide, Applied Catalysis B: Environmental, 201 (2017) 290-301.
[50] I. Simakova, B. Rozmysłowicz, O. Simakova, P. Mäki-Arvela, A. Simakov, D.Y. Murzin, Catalytic Deoxygenation of C18 Fatty Acids Over Mesoporous Pd/C Catalyst for Synthesis of Biofuels, Topics in Catalysis, 54 (2011) 460-466.
[51] E.W. Ping, J. Pierson, R. Wallace, J.T. Miller, T.F. Fuller, C.W. Jones, On the nature of the deactivation of supported palladium nanoparticle catalysts in the decarboxylation of fatty acids, Applied Catalysis A: General, 396 (2011) 85-90.

[52] A.T. Madsen, B. Rozmysłowicz, I.L. Simakova, T. Kilpiö, A.-R. Leino, K. Kordás, K. Eränen, P. Mäki-Arvela, D.Y. Murzin, Step Changes and Deactivation Behavior in the Continuous Decarboxylation of Stearic Acid, Industrial & Engineering Chemistry Research, 50 (2011) 11049-11058.
[53] M. Abdus Salam, D. Creaser, P. Arora, S. Tamm, E. Lind Grennfelt, L. Olsson, Influence of Bio-Oil Phospholipid on the Hydrodeoxygenation Activity of NiMoS/Al2O3 Catalyst, 8 (2018) 418.
[54] O.İ. Şenol, T.R. Viljava, A.O.I. Krause, Hydrodeoxygenation of aliphatic esters on sulphided NiMo/γ-Al2O3 and CoMo/γ-Al2O3 catalyst: The effect of water, Catalysis Today, 106 (2005) 186-189.
[55] M. Toba, Y. Abe, H. Kuramochi, M. Osako, T. Mochizuki, Y. Yoshimura, Hydrodeoxygenation of waste vegetable oil over sulfide catalysts, Catalysis Today, 164 (2011) 533-537.
[56] V.N. Urade, L.N.C. Soundararajan, A.A. Del Paggio, S. Gopal, P. Arora, Improved biomass conversion process, US20190169508A1, 2019.
[57] T. Ouni, V. Sippola, P. Lindqvist, Renewable oil with low iron content and its use in hydrotreatment process, Google Patents, 2012.
[58] H. Ojagh, D. Creaser, S. Tamm, P. Arora, S. Nyström, E. Lind Grennfelt, L. Olsson, Effect of Dimethyl Disulfide on Activity of NiMo Based Catalysts Used in Hydrodeoxygenation of Oleic Acid, Industrial & Engineering Chemistry Research, 56 (2017) 5547-5557.
[59] C.J. Easton, L. Xia, M.J. Pitt, A. Ferrante, A. Poulos, D.A. Rathjen, Polyunsaturated Nitroalkanes and Nitro-Substituted Fatty Acids, Synthesis, 2001 (2001) 0451-0457.
[60] Y.-J. Lee, K.-W. Jun, J.-Y. Park, H.S. Potdar, R.C. Chikate, A simple chemical route for the synthesis of γ-Fe2O3 nano-particles dispersed in organic solvents via an iron–hydroxy oleate precursor, Journal of Industrial and Engineering Chemistry, 14 (2008) 38-44.
[61] Y. Shi, J. Chen, J. Chen, R.A. Macleod, M. Malac, Preparation and evaluation of hydrotreating catalysts based on activated carbon derived from oil sand petroleum coke, Applied Catalysis A: General, 441–442 (2012) 99-107.
[62] T. Holderbaum, J. Gmehling, PSRK: A Group Contribution Equation of State Based on UNIFAC, Fluid Phase Equilibria, 70 (1991) 251-265.
[63] E.-M. Turpeinen, E. Sapei, P. Uusi-Kyyny, K.I. Keskinen, O.A.I. Krause, Finding a suitable thermodynamic model and phase equilibria for hydrodeoxygenation reactions of methyl heptanoate, Fuel, 90 (2011) 3315-3322.
[64] S. Horstmann, A. Jabłoniec, J. Krafczyk, K. Fischer, J. Gmehling, PSRK group contribution equation of state: comprehensive revision and extension IV, including critical constants and α-function parameters for 1000 components, Fluid Phase Equilibria, 227 (2005) 157-164.
[65] J.M.P. B. E. Poling, J. P. O'Connell, Properties of Gases and Liquids, 2001 ed., McGraw-Hill2001.
[66] S. Changi, A.J. Matzger, P.E. Savage, Kinetics and pathways for an algal phospholipid (1, 2-dioleoyl-sn-glycero-3-phosphocholine) in high-temperature (175–350 C) water, Green Chemistry, 14 (2012) 2856-2867.
[67] A. De Koning, K. McMullan, Hydrolysis of phospholipids with hydrochloric acid, Biochimica et Biophysica Acta (BBA)-Lipids and Lipid Metabolism, 106 (1965) 519-526.
[68] R. Iwamoto, J. Grimblot, Influence of Phosphorus on the Properties of Alumina-Based Hydrotreating Catalysts, in: W.O. Haag, B.C. Gates, H. Knözinger (Eds.) Advances in Catalysis, Academic Press1999, pp. 417-503.

[69] G. Liu, A.W. Robertson, M.M.-J. Li, W.C.H. Kuo, M.T. Darby, M.H. Muhieddine, Y.-C. Lin, K. Suenaga, M. Stamatakis, J.H. Warner, S.C.E. Tsang, MoS2 monolayer catalyst doped with isolated Co atoms for the hydrodeoxygenation reaction, Nature Chemistry, 9 (2017) 810.
[70] F. Diez, B.C. Gates, J.T. Miller, D.J. Sajkowski, S.G. Kukes, Deactivation of a nickel-molybdenum/.gamma.-alumina catalyst: influence of coke on the hydroprocessing activity, Industrial & Engineering Chemistry Research, 29 (1990) 1999-2004.
[71] M. Marafi, A. Stanislaus, Effect of initial coking on hydrotreating catalyst functionalities and properties, Applied Catalysis A: General, 159 (1997) 259-267.
[72] A. York, T. Xiao, M. L. H. Green, J. Claridge, Methane Oxyforming for Synthesis Gas Production, 2007.
[73] E. Uitterhaegen, K.A. Sampaio, E.I.P. Delbeke, W. De Greyt, M. Cerny, P. Evon, O. Merah, T. Talou, C.V. Stevens, Characterization of French Coriander Oil as Source of Petroselinic Acid, Molecules, 21 (2016) 1202.
[74] P. Rayo, J. Ramírez, P. Torres-Mancera, G. Marroquín, S.K. Maity, J. Ancheyta, Hydrodesulfurization and hydrocracking of Maya crude with P-modified NiMo/Al2O3 catalysts, Fuel, 100 (2012) 34-42.
[75] P. Arora, E.L. Grennfelt, L. Olsson, D. Creaser, Kinetic study of hydrodeoxygenation of stearic acid as model compound for renewable oils, Chemical Engineering Journal, 364 (2019) 376-389.
[76] M. Peroni, I. Lee, X. Huang, E. Baráth, O.Y. Gutiérrez, J.A. Lercher, Deoxygenation of Palmitic Acid on Unsupported Transition-Metal Phosphides, ACS Catalysis, 7 (2017) 6331-6341.
[77] P. Grange, Catalytic Hydrodesulfurization, Catalysis Reviews, 21 (1980) 135-181.